A Radial Drift Chamber Combining Tracking and Transition Radiation Detection for Use in the H1 Experiment at HERA

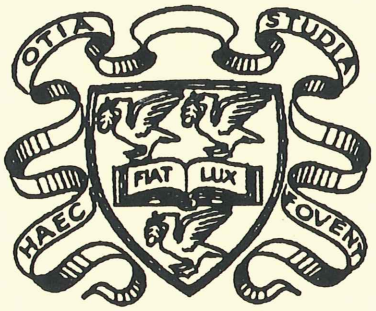

Thesis submitted in accordance with the requirements
of the University of Liverpool for the degree of
Doctor of Philosophy

by

Douglas Michael Gillespie

December 1992

Oliver Lodge Laboratory
University of Liverpool

A Radial Drift Chamber Combining Tracking and Transition Radiation Detection for Use in the H1 Experiment at HERA

Douglas Michael Gillespie

Liverpool, 1992

Abstract

The HERA accelerator, which was recently commissioned at the *Deutsches Elektronen Synchrotron* (DESY) in Hamburg, has been built to study interactions between quarks and leptons at a center of mass energy of up to 314 GeV.

Radial wire geometry drift chambers (RWDCs) have been installed in the forward track detector of the H1 experiment at HERA to simultaneously provide accurate track space points and to identify electrons by means of transition radiation.

This thesis describes the RWDCs and presents results of tests of a full sized RWDC in a high energy e/π beam at CERN. Both the spatial reconstruction accuracy and the e/π separation possible with the chambers have been investigated in a number of different gas mixtures. Results show that it is possible to achieve a drift coordinate error of less than 200 μm, averaged over the entire detector volume, and simultaneously discriminate between electrons and pions with less than 3 % pion contamination for 90 % electron efficiency at beam momenta of up to 50 GeV/c.

The radial coordinate, which is measured by charge division, is dominated by a large systematic error. The formation of pulses and the charge dividing mechanism have been studied using a Monte Carlo simulation of pulses in an equivalent electrical circuit for a RWDC anode. Results from the simulation show that the error results from changes in the shape of the pulses as they travel along the RWDC anodes and through connectors linking pairs of RWDC anodes at the center of the chamber.

Acknowledgements

Firstly I would like to thank my supervisor Erwin Gabathuler and, also, John Dainton for their valuable support during the course of my studies in Liverpool. I am also deeply indebted to all other members of the Liverpool H1 group, particularly those who helped during the setting up and running of the chamber in the CERN test beam. Without their enormous contribution this thesis would not have been possible. I must also thank my many colleagues from the universities of Lancaster and Manchester and from RWTH Aachen and the Rutherford Appleton Laboratory who helped during the test beam run.

Secondly I would like to thank the Science and Engineering research Council for financial support during the three years of my research and DESY and CERN for the use of facilities during the very enjoyable periods I spent at both those institutions. I am also grateful to the DELPHI group at CERN for forcing me to start work on September 1, 1992. Otherwise I may still have been writing this thesis on September 1, 1993 !

I would also like to thank my family and friends for their moral support and for taking me climbing when I should have been working. Thanks also to Sarah for proof reading this thesis in a brave attempt to correct the English.

Finally I would like to thank (and apologize to) Liz for still being my friend even when I talk about wire chambers for an entire weekend.

The Authors Contribution

I joined the Liverpool H1 group in March 1989. At that time, the full sized prototype had just been completed, and production of the three chambers for the H1 FTD was under way. The spring and summer of that year were spent setting up cosmic ray tests of the prototype and helping with the building and testing of the production chambers. During these tests, I noticed the large systematic shift in the charge division coordinate and started work on the simulation of drift chamber pulses presented in chapter 5.

A large amount of time between December 1989 and the summer of 1990 was spent installing and testing the production chambers into the FTD at RAL. In the summer of 1990, I followed the FTD to DESY and was responsible for testing the RWDCs prior to the installation of the FTD into the H1 experiment. I also played a major role in organizing the repair of one of the chambers.

In the spring of 1991, it became clear that H1 was not going to start taking data until 1992. It was therefore decided that I should take a RWDC to CERN to carry out tests using an e/π beam from the SPS during the summer of that year. I organized all aspects of setting up and running the test beam. Data were taken from within 30 minutes of the SPS starting up until we had to hand over the beam to people from the Zeus experiment 10 days later.

In August 1991, I returned to Liverpool, analyzed data from the CERN tests and finished work on the pulse simulation. H1 software already available at the time included the drift time, charge integration and track segment finding algorithms and the test pulse calibration routines. I used the CERN data to measure the systematic and random errors in the chamber, and to develop the other calibration and correction techniques described in chapters 3 and 4, and to look at the e/π separation in the chambers using transition radiation.

This thesis is dedicated to my parents who have contributed the following to high energy physics research:

"*We live in three dimensions – space, time, and doubt. Of the three, doubt is the most certain.*"

"*When are we going to get cheap electricity ?* "

Contents

List of Figures

List of Tables

Chapter 1

HERA and the H1 Detector

1.1 Introduction and Motivations for HERA

The HERA accelerator, which was recently commissioned at the *Deutsches Elektronen Synchrotron* (DESY) in Hamburg, has been built to study interactions between quarks and leptons at a center of mass energy of up to 314 GeV.

In recent years the Standard Model has successfully described, to a high degree of accuracy, interactions between particles at increasingly high energies. It describes all of the known particles and makes predictions for others such as the top quark and the Higgs boson (table 1.1). In fact the eventual discovery of the top quark is essential if the Standard Model is correct. The major drawback of the Standard Model is its inability to predict values for the large number of free parameters in the model which include the masses of the fundamental particles, the coupling constants and the mixing angles of the three forces which it describes. The Standard Model also fails to answer a number of important questions, including;

- Why are there only three generations of leptons and quarks ?
- Are leptons and quarks point-like or do they have substructure ?
- Why do quarks carry *exactly* $-\frac{1}{3}$ and $+\frac{2}{3}$ of the electron charge ?
- What is the origin of the masses of the fundamental particles ?

Particles			Charges
FERMIONS (SPIN $\frac{1}{2}$)	LEPTONS	ν_e $e^{\pm}$	0 1
		ν_μ $\mu^{\pm}$	0 1
		ν_τ $\tau^{\pm}$	0 1
	QUARKS	d u	$-\frac{1}{3}$ $+\frac{2}{3}$
		s c	$-\frac{1}{3}$ $+\frac{2}{3}$
		b t †	$-\frac{1}{3}$ $+\frac{2}{3}$
BOSONS	VECTOR BOSONS (SPIN 1)	γ	0
		$W^{\pm}$ Z^0	± 1 0
		8 gluons	0
	SCALAR BOSONS (SPIN 0)	Higgs †	0

Table 1.1: Today's 'Fundamental' Particles.

The center of mass energy of HERA interactions is similar to that of the LEP e^+e^- collider at CERN. LEP interactions are annihilation processes which therefore analyze the vacuum and the virtual particles it contains. HERA interactions are scattering processes which analyze the contents of the target and the projectile. The seemingly point-like nature of leptons makes them an ideal probe to study proton structure. Unlike proton-proton or proton-antiproton collisions where the fraction of the energy transfer is generally only a small fraction of the total center of mass energy, in electron-proton collisions the energy transfer is generally large. As a consequence of Heisenberg's uncertainty principle, high momentum transfers probe small distances. At a center of mass energy of 314 GeV, HERA interactions probe matter with a spatial resolution of $\sim 10^{-16}$ cm.

By colliding leptons and quarks, HERA will also produce large numbers of heavy

† The top quark and Higgs boson have yet to be observed experimentally.

quarks and will provide a unique opportunity to investigate new exotic phenomena involving both the lepton and quark sectors of the Standard Model. The principal areas of study undertaken by the collaborations of the H1 and Zeus experiments can be summarized as follows:

- To measure the proton structure functions.
- To search for new particles.
- To look for evidence of lepton and quark sub-structure.

It is also hoped that the experiments will be able to answer some of the outstanding questions arising from the Standard Model which were outlined above.

Details of some of the interactions expected at HERA are given in section 1.2. The rest of this thesis is then concerned solely with the detection apparatus which has been built to study such interactions. Section 1.4 gives an overview of the complete H1 detector. Chapter 2 describes a set of three drift chambers with novel radial wire geometry which are installed in the Forward Track Detector (FTD) of the H1 experiment. The chambers provide accurate track coordinates and use Transition Radiation (TR) to provide enhanced electron identification in the forward proton direction. Chapter 3 describes how one of the chambers was tested in a high energy electron/pion beam at CERN in the summer of 1991. The space point precision of the chambers is evaluated in chapter 4. In order to understand the origins of the systematic and random space point errors, chapter 5 describes a simple model of pulse formation on the anodes of a drift chamber and compares the results of that model with those from the analysis of test beam data. Finally, chapter 6 shows how transition radiation is detected in the chambers and measures the electron-pion separation as a function of particle momentum.

1.2 Electron-Quark Interactions at HERA

No attempt is made here to describe all of possible interactions which could take place at HERA. A selection of interactions is described which I hope will give the reader a

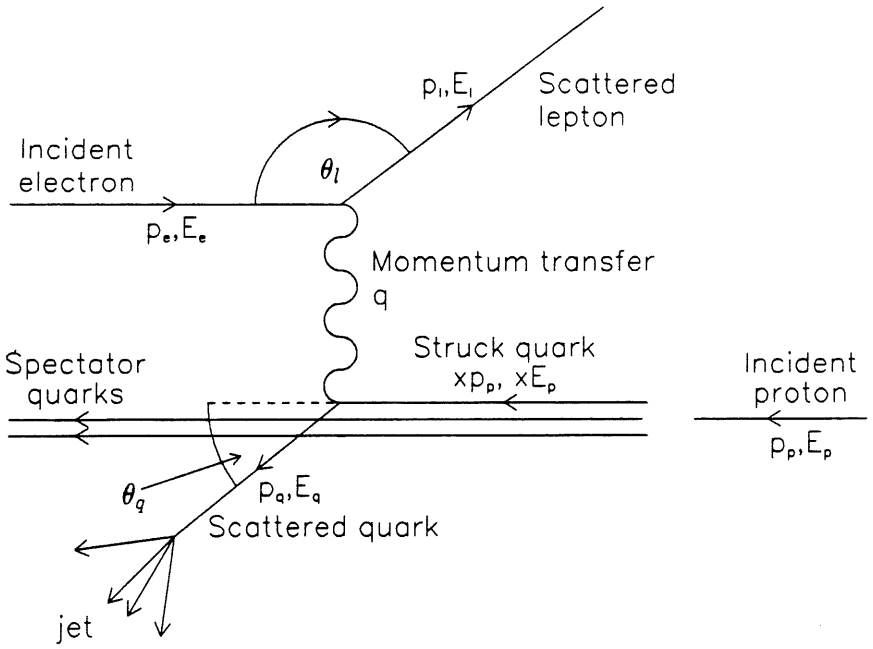

Figure 1.1: Schematic diagram of a typical HERA interaction.

feel for the type of physics undertaken at HERA and, more importantly, a feel for what the events will look like in the detector. A complete description of HERA physics is given in the proceedings of the HERA workshops [1, 2]

1.2.1 The Kinematics of HERA Interactions

Before proceeding with the interactions themselves it is necessary to take a look at the general topology and kinematics of HERA interactions.

The energies of the electron and proton at HERA are sufficiently large for their rest masses to be ignored, so the square of the maximum possible 4-momentum transfer is given by

$$s = (p_e + p_p)^2 = 4E_eE_p \tag{1.1}$$

where p_e, p_p, E_e and E_p are the momentum and energy of the incident electron and proton respectively. The maximum center of mass energy of HERA interactions is $\sqrt{s} = 314$ GeV.

At high enough momentum transfer, the incident lepton scatters off a single quark

(or gluon) in the incident proton (figure 1.1). The lepton and struck quark emerge at angles θ_l and θ_q to the forward proton direction respectively. Due to the confinement of quarks, the struck quark 'fragments' into a jet of more stable particles. Depending on the type of interaction, the incident electron can re-emerge as an electron or as an electron neutrino ν_e. The 'spectator' quarks (i.e. those which were not struck) in the remnants of the proton also form hadronic jets but generally have a low transverse momentum and therefore remain in the beam pipe and do not play a role in HERA physics.

If q is the 4-momentum transferred between the lepton and the quark, it is conventional to work with the variable Q^2 which is defined by

$$Q^2 \equiv -q^2 = -(p_e - p_l)^2 \simeq 4E_e E_l \cos^2\left(\frac{\theta_l}{2}\right) \tag{1.2}$$

where E_e and E_l are the energy of the incident and scattered lepton respectively (and the particles rest masses have again been ignored in the approximation). The Bjorken x defines the fraction of the proton momentum carried by the struck quark [1]:

$$x \equiv \frac{Q^2}{2p_p q} \simeq \frac{E_e E_l \cos^2\left(\frac{\theta_l}{2}\right)}{E_p\left(E_e - E_l \sin^2\left(\frac{\theta_l}{2}\right)\right)} \tag{1.3}$$

Another useful variable is the Bjorken y:

$$y \equiv \frac{p_p.q}{p_p.p_e} = \frac{2p_p.q}{s} \simeq \frac{E_e - E_l \sin^2\left(\frac{\theta_l}{2}\right)}{E_e} \tag{1.4}$$

In equations 1.2 and 1.3, both Q^2 and x have been calculated without any reference to the scattering angle or energy of the struck quark. If the lepton emerges from the interaction as a neutrino, it will be impossible to measure either its energy or scattering angle. It will then be necessary to measure the scattering angle θ_q and the energy E_q of the particles in the jet in order to obtain the 4-momentum of the scattered quark. In fact Q^2 and x can be calculated if a measurement is made of any two out of the four quantities E_l, θ_l, E_q or θ_q.

Figure 1.2 shows the scattering angles and energies of the lepton and struck quark in the (x, Q^2) plane. To demonstrate the increase in the kinematic range possible with HERA, the kinematic limit of the European Muon Collaboration (EMC) experiment at CERN is also shown [3].

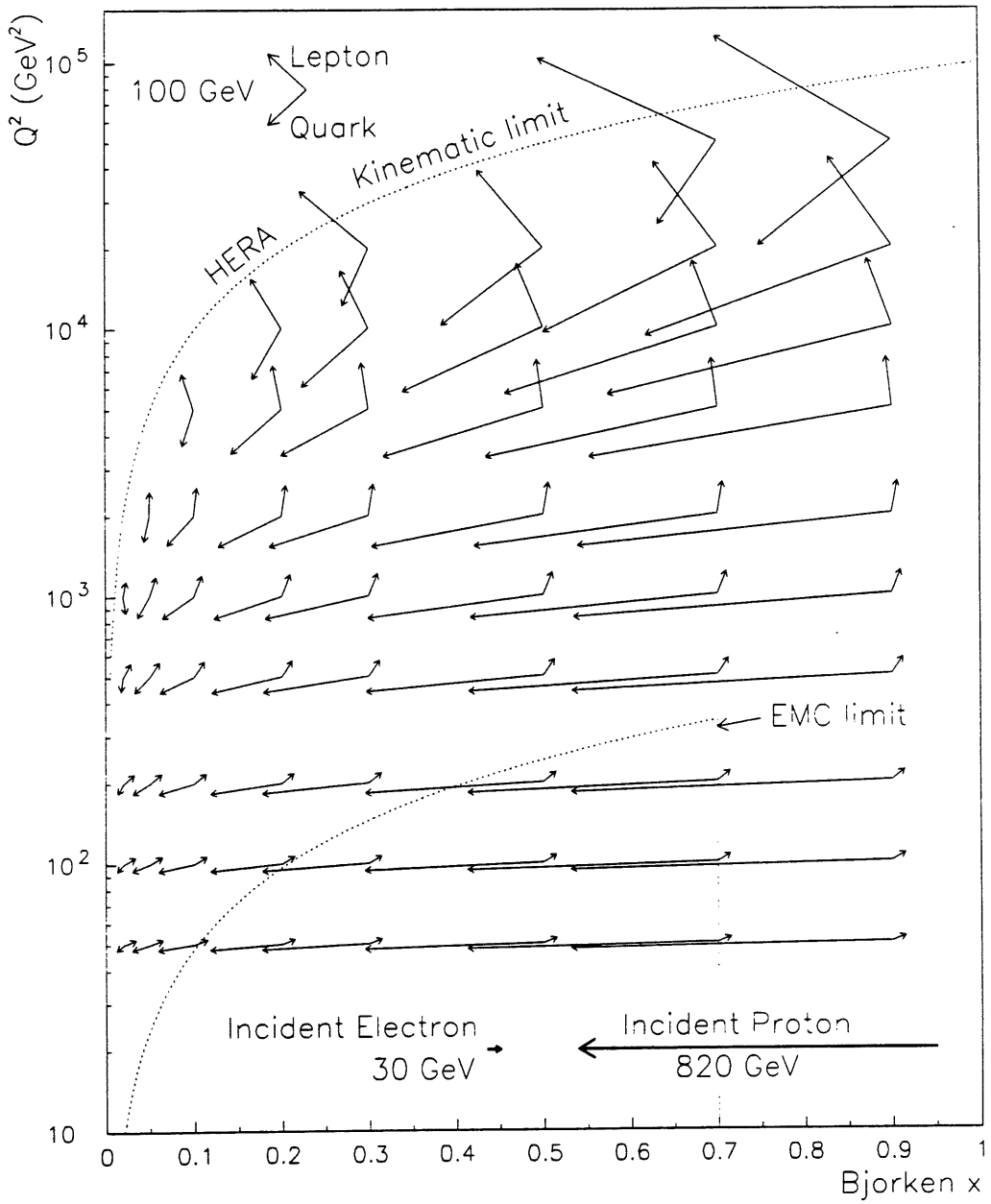

Figure 1.2: Scattering angle and energy of the lepton and struck quark for HERA interactions in the (x, Q^2) plane. The length of the arrows denotes the energy of the particles.

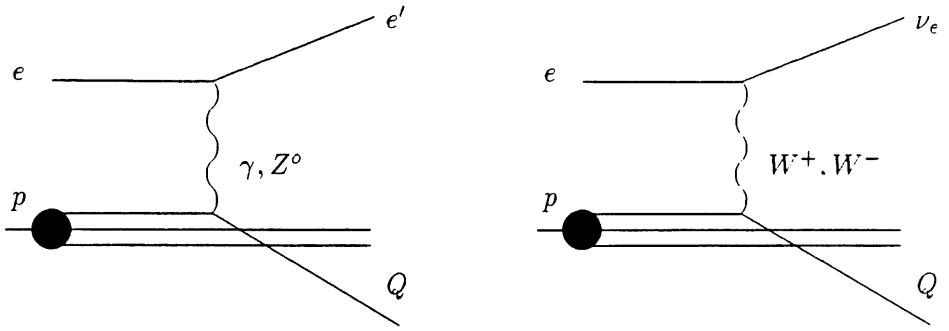

Figure 1.3: Leading order Feynman diagrams for neutral and charged current interactions.

1.2.2 Deep Inelastic Scattering

In Deep Inelastic Scattering (DIS) events, the incident electron penetrates deeply into the incident proton and scatters off one of its constituent quarks or gluons. It is often convenient to think of DIS between electrons and protons as elastic scattering between electrons and quarks or gluons. DIS interactions divide into two categories:

1. Neutral current (NC), where scattering is via either γ or Z^0 exchange resulting in the ejection of the struck quark and the re-emergence of an electron.

2. Charged current (CC), involving the exchange of a $W^{\pm}$. Again the struck quark is ejected from the proton, but the incident electron now emerges as an electron neutrino ν_e.

Leading order diagrams for NC and CC events are shown in figure 1.3.

The leading order cross section for NC scattering is

$$\frac{d^2\sigma_{NC}}{dxdQ^2} = \frac{4\pi\alpha^2}{xQ^4}\left\{y^2 xF_1\left(x,Q^2\right) + (1-y)F_2\left(x,Q^2\right) + \left(y - \frac{y^2}{2}\right)xF_3\left(x,Q^2\right)\right\} \quad (1.5)$$

where F_1, F_2 and F_3 are the quark structure functions and $\alpha = \frac{1}{137}$ is the fine structure constant.

The leading order cross section for CC scattering is

$$\frac{d^2\sigma_{CC}}{dxdQ^2} = \frac{G_F^2 M_W^4}{\pi x\left(M_W^2 + Q^2\right)^2}\left\{\begin{array}{c} y^2 xF_1\left(x,Q^2\right) + (1-y)\,F_2\left(x,Q^2\right) \\ + \left(y - \frac{y^2}{2}\right)F_3\left(x,Q^2\right) \end{array}\right\} \quad (1.6)$$

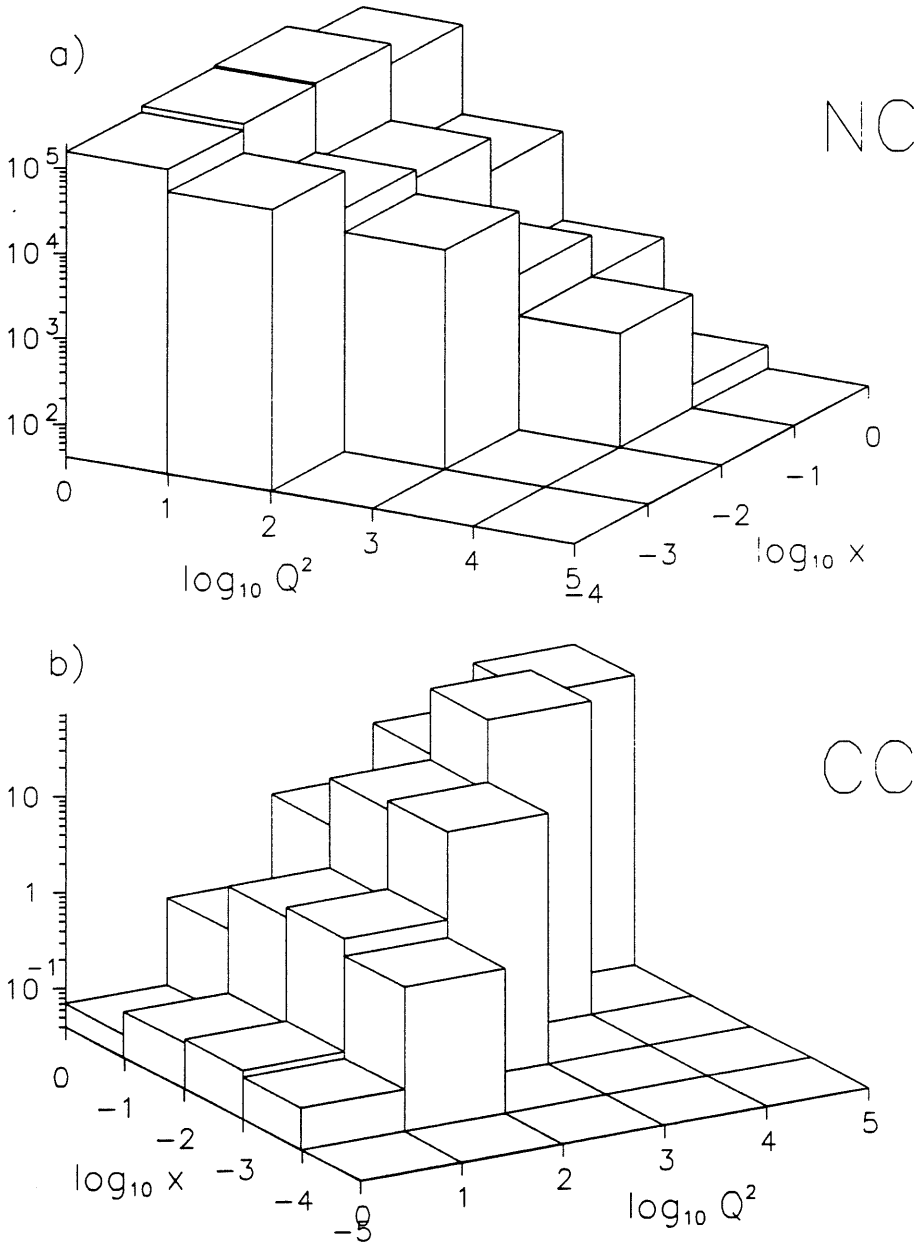

Figure 1.4: Number of a) neutral current and b) charged current interactions for 1 pb^{-1} of luminosity as a function of x and Q^2. (Note the very different vertical scales).

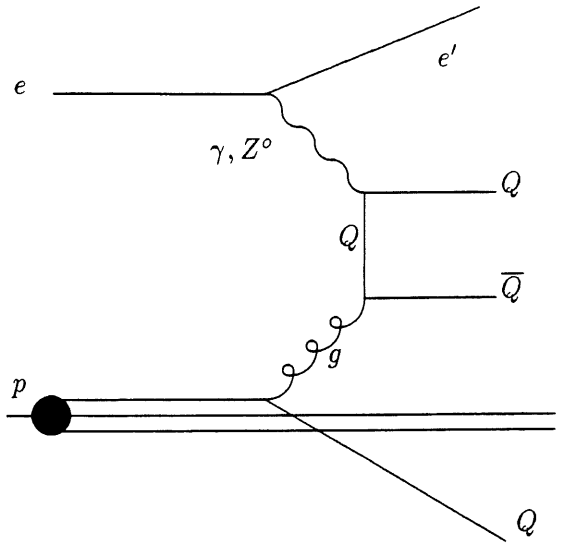

Figure 1.5: Heavy flavor production by boson-gluon fusion.

where G_F is the Fermi coupling constant and M_W the W boson mass. Equation 1.6 only applies to left handed electrons (or right handed positrons) since the resultant electron neutrino ν_e can only be left handed (or anti electron neutrino $\overline{\nu}_e$ right handed).

Figure 1.4 shows the number of neutral and charged current events for 1 pb^{-1} of luminosity at HERA. The rate of charged current events is low since they may only occur via the exchange of massive W bosons and therefore tend not to occur for momentum transfers much below the mass scale of the W boson (80.6 GeV). The structure functions used for the calculation of rates in figure 1.4 come from muon and neutrino scattering in fixed target experiments [4].

1.2.3 Heavy Flavor Production

Collisions between electrons and quarks at HERA energies should produce large numbers of heavy flavor quarks, namely charm (c), strange (s) and bottom (b), through the process of boson-gluon fusion.

The proton contains three valence quarks, two u and one d. The valence quarks constitute approximately 37 % of the proton mass, 47 % of the mass is from gluons and the remainder may be attributed to what are known as sea quarks. Sea quarks can be of any flavor, their contribution to the proton structure function being principally at low x. It is therefore possible that heavy quarks can be ejected from the proton

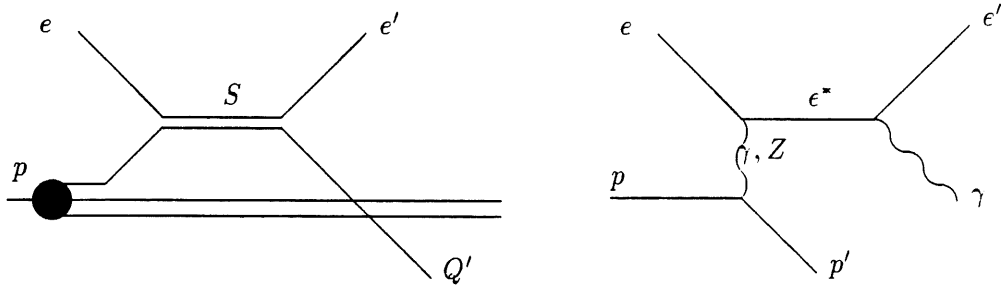

Figure 1.6: Leptoquark and excited electron production at HERA.

by the DIS interactions described above. Since there is little evidence for intrinsic c and b quarks in the proton, however, heavy quarks are more likely to be produced at HERA by boson-gluon fusion as shown in figure 1.5. As well as direct studies of the heavy quarks and their decays, heavy flavor production by this mechanism will allow measurement of the gluon structure of the proton.

1.2.4 Exotic Physics at HERA

The combination of lepton and proton beams makes HERA an excellent facility for the study of exotic behavior by both leptons and quarks. Furthermore it may allow glimpses into an underlying substructure common to both quarks and leptons. Such a substructure is most likely to manifest itself in the form of a bound state between a lepton and a quark or a gluon – a leptoquark or leptogluon. Such events (if they occur within the HERA kinematic limits) should appear as clean resonances above the neutral and charged current backgrounds [1].

Another possibility is the production of electron excited states. The scattered parton p' in elastic e* production would remain in the beam pipe, leaving a clear signal in the detector consisting of nothing but a scattered electron e^- and a photon γ (figure 1.6).

Project	Lab	Particles	Energies (GeV)		E_{COM}	YEAR
S$p\bar{p}$S	CERN	$p\bar{p}$	315	315	630	1981
Tevatron	FNAL	$p\bar{p}$	1000	1000	2000	1987
LEP I	CERN	$e\bar{e}$	60	60	120	1989
HERA	DESY	ep	30	820	314	1992
LEP II	CERN	$e\bar{e}$	90	90	180	1995
IHEP/UNK	Serpukov	pp	3000	3000	6000	?
LHC	CERN	pp	8000	8000	16000	?
SSC	USA	pp	20000	20000	40000	?

Table 1.2: Comparison between HERA and other accelerators from around the world.

1.3 The HERA Accelerator

It can be seen from table 1.2 [5] that HERA is unique in that it collides beams containing two particles of different mass as opposed to colliding particles with their corresponding antiparticles or particles of the same kind as in the case of previous experiments. Whereas in previous collider experiments it has generally been possible to have a single beam pipe containing bunches of particles circulating in opposite directions[†], the different beam momenta at HERA necessitate two separate acceleration and storage systems whose beams are only brought together at the interaction regions.

Electrons are injected into HERA from PETRA at an energy of 14 GeV. Protons are injected from PETRA at 40 GeV after first being accelerated to 7.5 GeV in the new synchrotron, DESY-III. Because of the high momentum of the HERA proton beam, a vertical magnetic field of 4.7 T is required to contain it in the ring. The large currents required to achieve such a high field necessitates that the proton ring is fully equipped with helium cooled superconducting dipole magnets. Due to its much lower energy, the electron beam is held in place by conventional 'warm' magnets. However, due to the high energy losses from electron beams due to synchrotron radiation, the

[†] Except in the case of the ISR at CERN

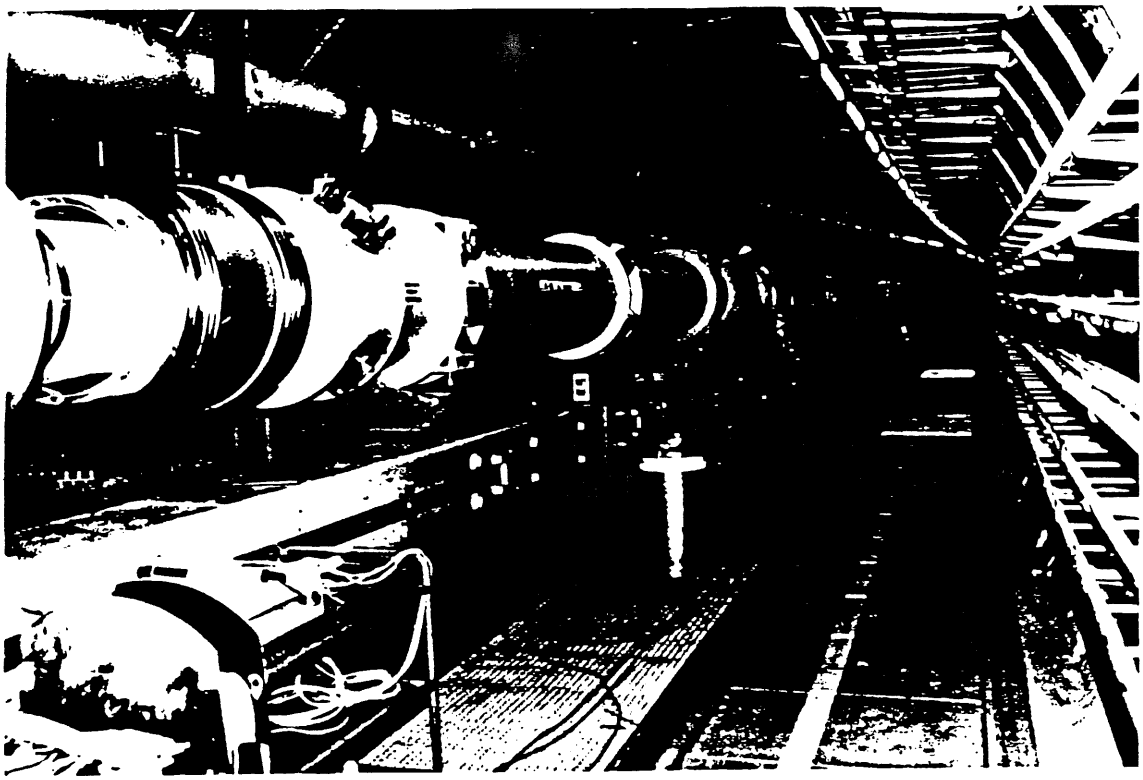

Figure 1.7: Photograph of the proton (top) and electron (bottom) storage rings in the HERA tunnel.

electron storage ring requires superconducting radio frequency (rf) cavities to achieve the maximum design energy of over 30 GeV. Conventional copper cavities are used to accelerate protons. Beam energies reach equilibrium when the loss in energy to synchrotron radiation matches the energy being put back into the beam from the rf system.

For most of the length of the HERA tunnel the two storage rings sit one above the other (figure 1.7). Close to the interaction regions it is necessary to bend the electron beam through a relatively tight curve for head-on collisions with the proton beam. This sudden bending of the electron beam is the cause of a large flux of synchrotron radiation close to the experiments, leading to potentially large backgrounds. In order to achieve the required luminosity of 16×10^{30} cm^{-2}s^{-1}, bunches of electrons and protons will cross the interaction regions of the experiments every 96 ns. This has lead to the development of very sophisticated multi-level triggers and data pipe-lining systems for

the experiments in order to unambiguously select genuine physics events from particular bunch crossings.

1.4 The H1 Detector

To fully exploit the physics potential of HERA outlined above, the detector must satisfy the following general requirements [6].

- Electrons play a key role in HERA physics which demands that the detection apparatus achieves the best possible electron momentum resolution and identification.
- It must have a high degree of hermeticity in order to investigate phenomena involving neutrinos and other non-interacting secondary particles.
- It must permit excellent energy flow measurements for the inclusive measurement of neutral current and charged current based on good energy resolution, fine granularity and absolute energy calibration, both for the electromagnetic and hadron calorimeters.
- Muon identification and energy measurement must be good for new physics searches, for phenomena involving heavy flavors and to preserve hermeticity when high energy muons are present.

Furthermore, due to the unique event topologies of HERA interactions, a detector is required which is asymmetrical in design, with enhanced tracking, calorimetry, muon identification and electron identification in the forward proton direction. A cut-away view of the H1 detector is shown in figure 1.8. Working outwards from the interaction region, the main features of the detector are:

1. Central and forward charged track detectors (see section 1.4.1).
2. Liquid argon calorimeter in the barrel and forward regions covering angles to the forward proton direction of $20° < \theta < 152°$. It has an electromagnetic section with lead absorber plates (20 to 30 radiation lengths) and a hadronic

Experiment H1

Vertical cut along the beam/
Längsschnitt in Strahlrichtung

Overall size: 12 x 10 x 15m
Abmessungen: 12 x 10 x 15m
Total weight: 2800 tons
Gesamtgewicht: 2800 Tonnen

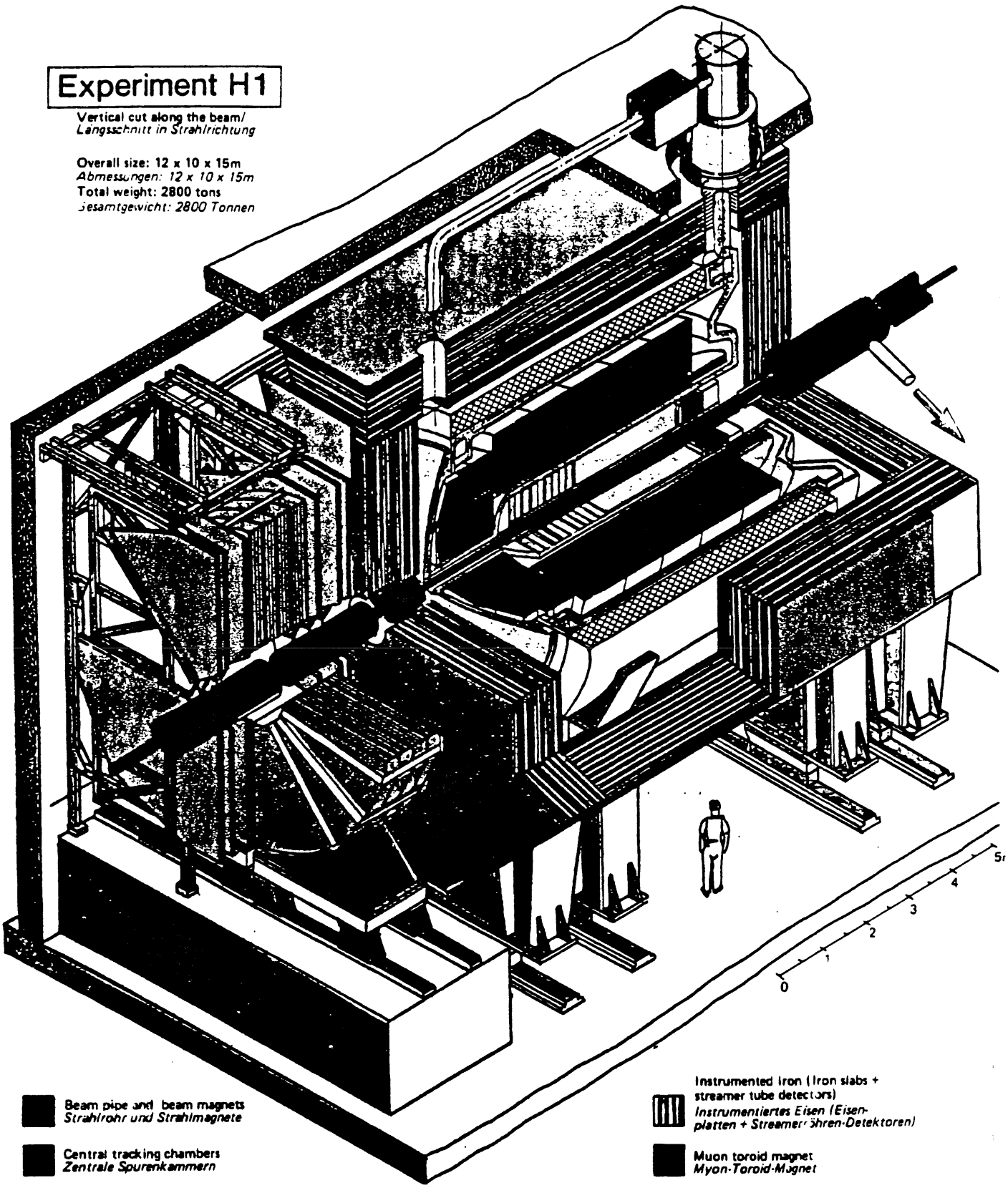

Beam pipe and beam magnets
Strahlrohr und Strahlmagnete

Central tracking chambers
Zentrale Spurenkammern

Forward tracking chambers and transition radiators
Vorwärtsspurenkammern und Übergangsstrahlungsmodul

Electromagnetic Calorimeter (lead)
Elektromagnetisches Kalorimeter (Blei)

Hadronic Calorimeter (stainless steel)
Hadronisches Kalorimeter (Edelstahl)

Liquid Argon
Flüssiges Argon

Superconducting coil (1.2 Tesla)
Supraleitende Spule (1,2 Tesla)

Compensating magnet
Kompensationsmagnet

Helium cryogenics
Helium Kälteanlage

Muon chambers
Myon-Kammern

Instrumented Iron (Iron slabs + streamer tube detectors)
Instrumentiertes Eisen (Eisenplatten + Streamerröhren-Detektoren)

Muon toroid magnet
Myon-Toroid-Magnet

Warm electromagnetic calorimeter
Warmes elektromagnetisches Kalorimeter

Plug calorimeter (Cu,Si)
Vorwärts-Kalorimeter

Concrete shielding
Betonabschirmung

Liquid Argon cryostat
Flüssig Argon Kryostat

Figure 1.8: (previous page) Cut-away view of the H1 detector.

section with stainless steel absorber (3.5 to 7 interaction lengths). The energy resolutions for electrons and pions are 12 $\%/\sqrt{E}$ and 50 $\%/\sqrt{E}$ respectively. Installing both sections of the calorimeter in the same cryostat improves the energy flow measurements and reduces the amount of material in front of the hadronic section.

3. The liquid argon calorimeter is complemented in the backward direction by a lead scintillator sandwich (22 radiation lengths) which measures electromagnetic energy at angles between 152° and 176°. The energy resolution of this calorimeter is 10 $\%/\sqrt{E}$.

4. The superconducting coil is situated outside the liquid argon calorimeters to provide maximum uniformity of the 1.2 T magnetic field used for particle momentum measurement in the charged track detectors.

5. The instrumented iron acts as a flux return yoke, and contains streamer tubes for muon identification and to act as a tail catcher for the hadron calorimeter.

6. In the forward direction a toroid magnet and further sets of muon chambers provide extra muon identification and momentum measurement.

7. A plug calorimeter mounted in the instrumented iron in the forward direction closes the detector down to an angle of 0.7°. This consists of layers of silicon sandwiched between copper plates to meet the strict space limitations in this region.

8. In the backward direction, a super conducting compensation magnet ensures zero integrated magnetic field over the complete detector.

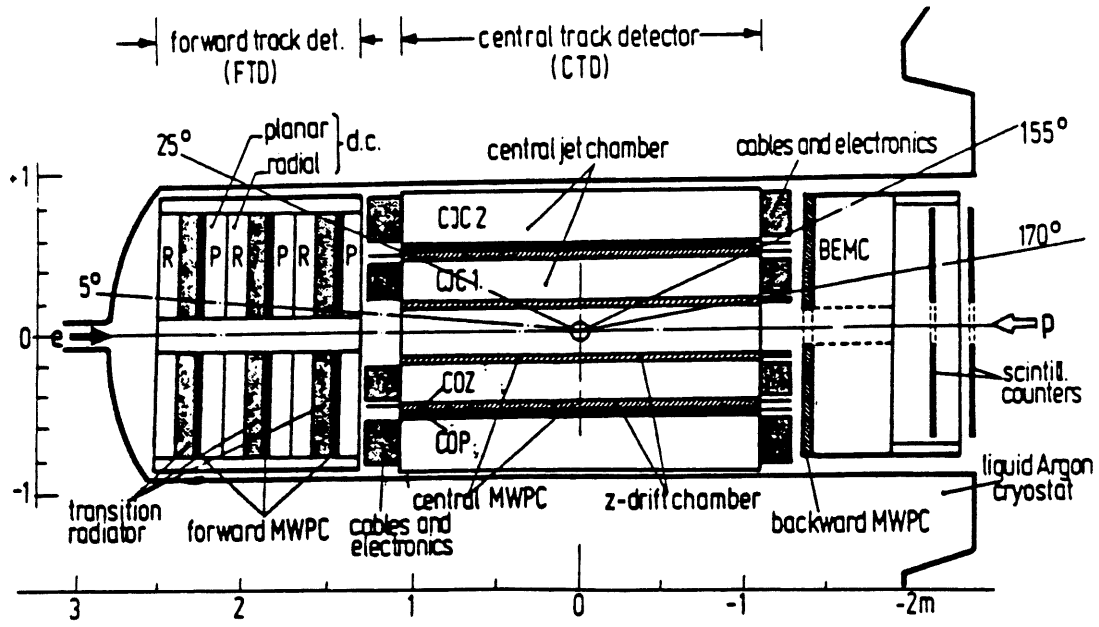

Figure 1.9: The tracking detectors of the H1 experiment.

1.4.1 Charged track detectors

The layout of the H1 tracking detectors is shown in figure 1.9. The tracking detectors divide into two main regions. The central track detector (CTD) which is symmetric about the interaction region has an angular acceptance of between 15° and 170°. The forward track detector (FTD) covers angles between 7° and 25° to the beam pipe. In the backward region a Multiwire Proportional Chamber (MWPC) consisting of four wire planes covers angles between 155° and 175°.

A particle passing through the CTD traverses first a MWPC (known as CIP – for Central Inner Proportional chamber) and the first of two drift chambers which have the direction of electron drift parallel to the z-axis and therefore provide an accurate z measurement (CIZ). Particles then traverse the first of two large jet chambers (CJC1) which has wires strung parallel to the z-axis and has its drift cells tilted at $\sim 30°$ to the radial direction. The jet chambers measure the ϕ coordinate of charged tracks to a precision of 200 μm, providing a transverse momentum[‡] resolution of $\Delta p/p^2 = 0.01/\text{GeV}$.

[‡] The transverse momentum is defined as the component of momentum perpendicular to the beam pipe.

The particles then cross a second z-chamber (COZ), a second MWPC (COP) and the second jet chamber (CJC2). Charge division is used in the z chambers to measure ϕ and in the jet chambers to measure z. The importance of the interplay between the z-chambers and the jet chambers is discussed in section 5.7.

In a similar way, the FTD contains layers of multiwire and drift chambers. The FTD is described in detail in section 2.1.

1.4.2 Lepton Identification in the H1 detector

It is clear from section 1.2 that lepton identification must play a central role in understanding HERA physics. In neutral current events the kinematics of the event may be reconstructed purely from the energy and scattering angle of the electron. Charged leptons also provide a useful signature for processes such as boson-gluon fusion and lepto-quark or lepto-gluon production.

1.4.2.1 Muon Identification

Muons may be identified by their penetration of the liquid argon calorimeter (5 to 8 absorption lengths) [6] and the instrumented iron (4.5 to 9 absorption lengths). In the barrel region muons are tracked by 8 layers of streamer tubes in the instrumented iron and by a further 3 layers of drift chambers which clad the outside of the iron (figure 1.8). In the forward region, muons are tracked at angles of between 3° and 17° by a further 6 double layers of drift chambers, three each side of a warm toroid magnet which provides an integrated magnetic field of ~ 2 Tm achieving a momentum resolution of $\frac{\Delta p}{p} \approx 30$ %.

1.4.2.2 Electron Identification

Electron identification in H1 is based on the transverse and longitudinal shower shape in the liquid argon calorimeter, and on a comparison of track momentum with the calorimetric energy and of the shower position with the impact point of the track, giving a π/e rejection of $\leq 10^{-3}$ [6]. Calorimetric electron identification is degraded in the vicinity of cracks and by up to a factor of 10 if the electron is in the vicinity of a

jet. Calorimetric measurements are complemented with pulse integral measurements (dE/dx) in the CTD and a combination of dE/dx and transition radiation detection in the FTD (chapter 6). Although the intrinsic e/π separation using these latter methods is poor compared to the liquid argon, they do have the advantage of being able to unambiguously associate the particle type with a particular track even in the dense multi-track environment at HERA.

1.5 Conclusions

The large center of mass energies of HERA interactions provides a unique probe to study the proton structure on a much smaller distance scale than previously possible. It also provides a unique opportunity for looking at exotic phenomena involving both quarks and leptons. The H1 detector is well matched to both the known and the speculative physics of HERA and will be a powerful tool for exploring new phenomena if its components can be operated to their specified precision.

Chapter 2

The Forward Track Detector and Radial Wire Drift Chambers

2.1 The Forward Track Detector (FTD)

The importance of the Forward Track Detector (FTD) can be easily seen in figure 1.2 on page 6. Over most of the HERA kinematic range, the struck quark is emitted at an angle of less than 25° to the forward proton direction and will therefore pass through the FTD.

The design objectives of the FTD are:

- Momentum resolution for charged tracks $\Delta p/p^2 \leq 0.3$ %.
- Enhanced electron identification by means of a combination of Transition Radiation (TR) detection and track ionization (dE/dx) measurement in the FTD drift chambers.
- Multi-track angular resolution of < 1 mrad.
- Efficient pattern recognition and visual recognition of tracks from raw digitizations to facilitate on-line examination of data.
- Provision of a fast (< 96 ns) signal for triggering and timing purposes.

The FTD consists of three supermodules (figure 1.9), each containing a planar wire drift chamber (PWDC), a MWPC, transition radiator and a Radial Wire Drift Chamber (RWDC). Interleaving planar and radial wire drift chambers in this way provides the optimum lever arm for accurate momentum measurement. The PWDC is situated at the front of each supermodule since its homogeneous spatial precision in x and y is most suitable for linking to tracks in the central track detector. For practical reasons the MWPCs are mounted directly behind the PWDCs since they use the same gas mixture. There is also some advantage to be gained by having the MWPCs as far forward as possible since this maximizes the geometrical trigger efficiency of the FTD. By default therefore, the transition radiator and RWDC are at the back of each supermodule.

Each PWDC contains 3 planes, each of 4 wires in z, rotated at 60° to each other in azimuth – so called x, u and v. They provide constant track segment precision in x, u and v throughout the FTD angular coverage. Linking PWDC and RWDC track segments not only provides the required momentum resolution but is also essential for precise calibration of the RWDC charge division coordinate r (see section 4.4).

After each PWDC, particles cross two MWDC planes, a coincidence of which provides a fast (< 96 ns) signal for bunch crossing timing and triggering purposes and reduces background due to the high levels of synchrotron radiation from the HERA accelerator.

After each MWPC and directly preceding each RWDC, particles pass through a transition radiator consisting of 400 polypropylene foils. Each RWDC provides up to 12 accurate track space points from ionization drift timing and charge division. e/π discrimination is achieved in the dense multi-track environment of the FTD by pulse integral analysis of dE/dx and TR ionization energy deposition. The second and third RWDCs are rotated by 3.75° and 2.5° ($\frac{1}{2}$ and $\frac{1}{3}$ of a wedge) relative to the first. This improves the two track resolution of the FTD since a track which is lost behind another track in one RWDC will appear before it in the next.

Precision support of FTD components is provided by an aluminium tank which also acts to contain the 3 different gas envelopes per FTD supermodule ($Ar:C_3H_8$ for the PWDC and MWPC, $He:C_2H_6$ for the transition radiator, and $Ar:C_2H_6$ or $Xe:He:C_2H_6$

for the RWDC). Although the ideal gas for the transition radiators would be pure He, it is necessary to use a mixture containing 30 % C_2H_6 to ensure high voltage stability of the RWDC front field forming strips which lie inside the transition radiator gas volume.

2.2 Radial Wire Drift Chambers

The wires in a RWDC are strung radially from a central hub (r = 15 cm) to the outer radius of the tracking volume (r = 76 cm). Each RWDC is segmented into 48 wedge shaped drift cells in ϕ, each containing 12 resistive anode wires 1 cm apart in z (figure 2.1). Drift cells are separated by cathode planes with voltage graded copper strips to maintain a constant drift field perpendicular to and on each side of each wire plane. Left-right track segment ambiguities are resolved by an alternate ± 287 μm stagger of the anodes out of the wire plane.

Drift timing, even in the presence of substantial ionization drift Lorentz angle ($\sim 30°$ for Xe:He:C_2H_6 gas mixtures and $\sim 45°$ for Ar:C_2H_6 50:50) always measures track sagitta and therefore provides an accurate transverse momentum measurement. Charge division of the signal on a pair of anode wires which are coupled at the inner radius and read out at the outer radius measures r. Coupling wedges at the hub in this way avoids reading out both ends of each individual anode wire which would lead to excessive amounts of material close to the beam pipe and also double the number of RWDC read out channels. Each hit on each anode wire provides space point coordinates in $(r\phi, r)$. In the uniform magnetic field along the beam axis (z), ϕ is proportional to z so this arrangement is optimal for fast track recognition. Another advantage of the radial geometry is that space in the FTD is filled efficiently, the cell size being smaller close to the beam pipe where there is a higher track density.

2.2.1 RWDC Design and Construction

Each RWDC is constructed inside a 'saucepan-like' shell which makes up the back and sides of the chamber and acts as a support for other RWDC components (figures 2.1 and 2.2). It is constructed from Kevlar skinned Nomex honeycomb [7]. The structure has a very low mass and is also rigid and stable enough to support the combined tension

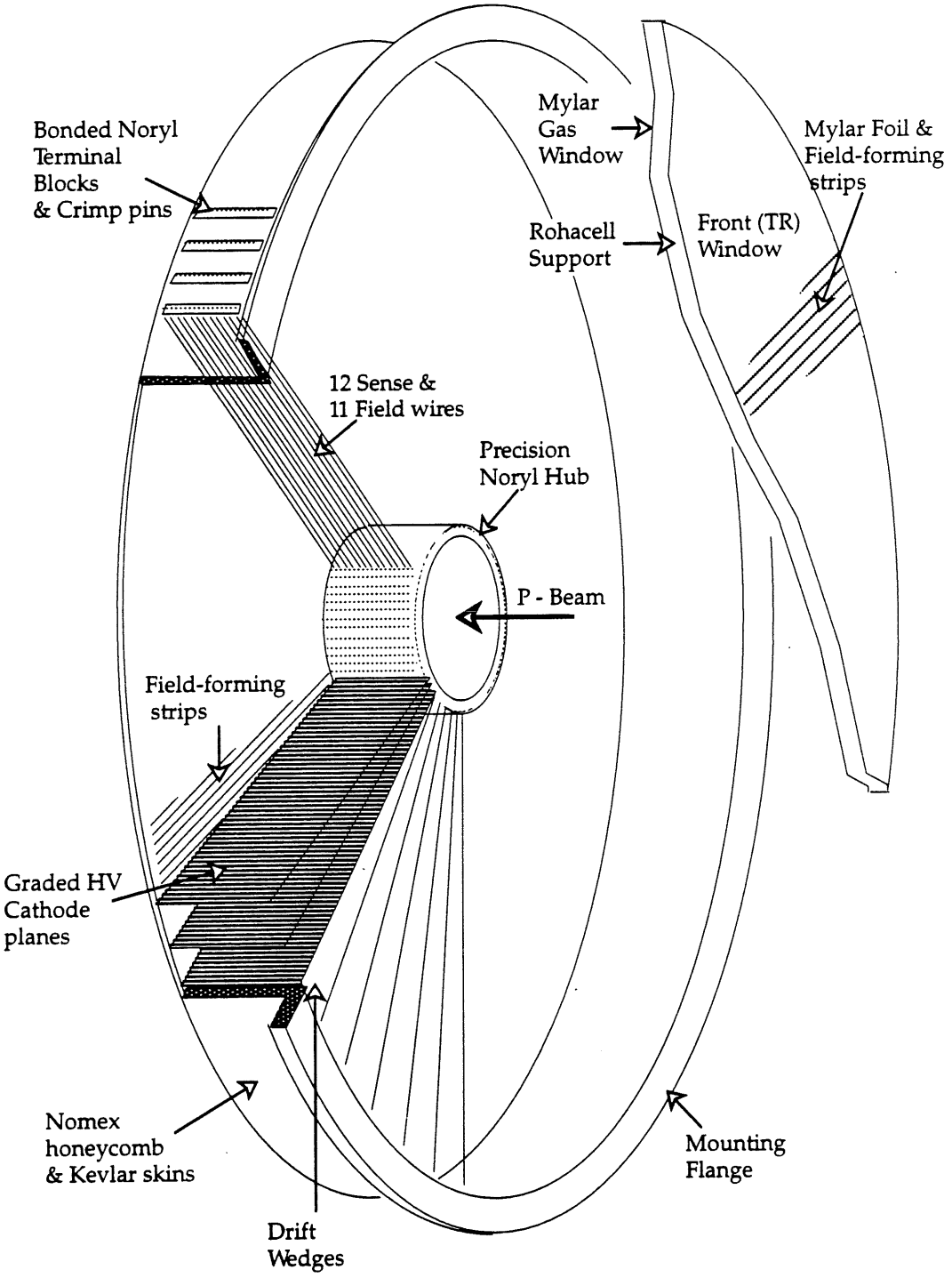

Figure 2.1: Schematic exploded view of a RWDC showing the main structural features.

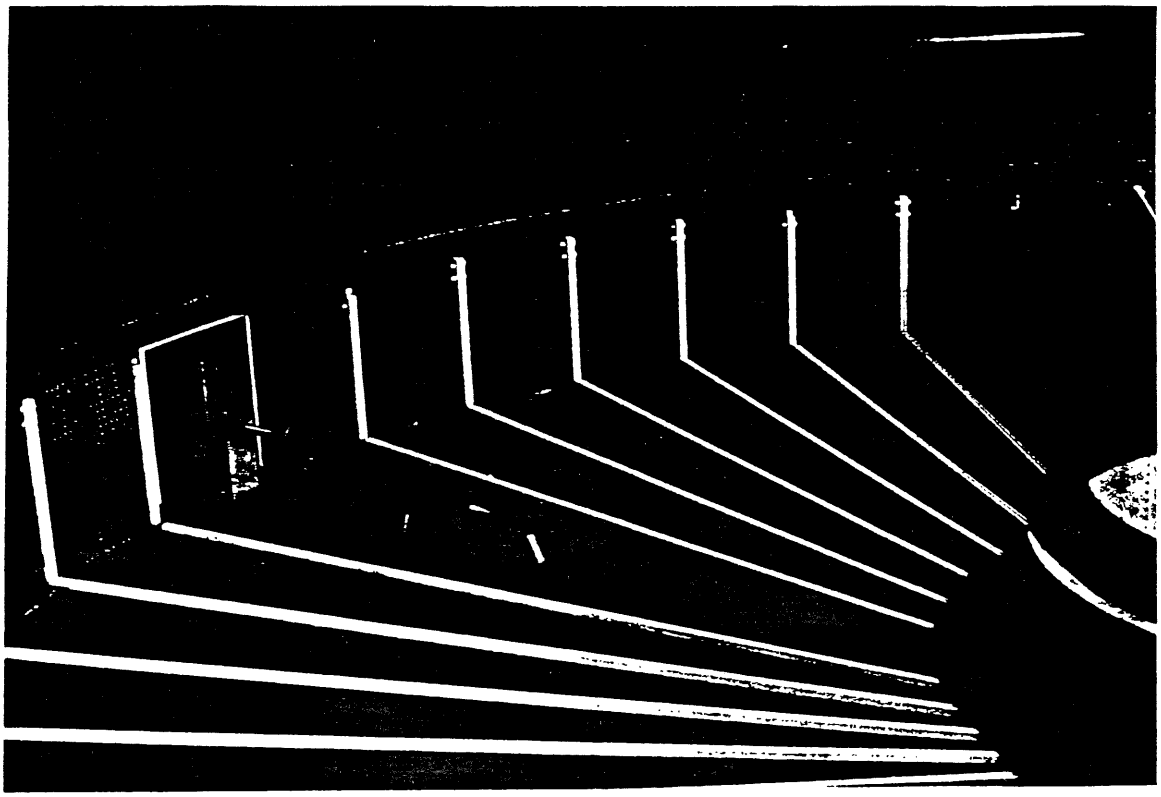

Figure 2.2: The back field formers being bonded to the composite shell. Clearly visible are the Noryl guides for the cathodes and the Noryl hub at the center of the chamber.

of the 1104 wires in each chamber. The rim of the shell attaches the RWDC to the tank and also contains dowel holes for alignment. A further advantage of this construction material is that it contains no silicon. Silicon residues building up on anode wires in a drift chamber can lead to premature ageing of the wires and a reduction in gain [8].

A Noryl [9] hub and templates support the wires at the center and outer radius of the chamber. Noryl may be machined and bonded to a much greater accuracy than the large composite shell. Extensive surveys have shown that the final positions of the wire support crimps are accurate to within 38 μm of their nominal positions [10].

After mounting the hub and the templates, Noryl support guides for the cathode planes are bonded onto the inside of the shell at the back and outer radius of the chamber. Slots exist in the hub to support the cathodes at the inner radius. To facilitate access to the chamber during wiring, the actual insertion of the cathodes is left until later.

The back field formers, which complete the drift cage at the back and outer radius of the drift cells (section 2.2.3) are next bonded onto the inside of the shell, between the cathode support rails (figure 2.2). They are made from 0.3 mm epoxy impregnated paper [11] with 2 mm wide copper strips, running parallel to the wires, spaced 3 mm apart.

Once the back field formers and cathode support rails have been bonded into position the chamber is ready for wiring. This is relatively straightforward given the open nature of the design, all wires being freely accessible even when they are all strung. The anode wires are 50 μm diameter Stablohm [12] (80 % nickel, 19 % chromium and 1 % aluminium) which, as its name suggests, has a constant resistivity over a wide temperature range. Between the 12 anode wires are 11 grounded field wires made from 125 μm diameter copper. Wires are strung starting from the back of the chamber with the chamber mounted on a vertical support. They are strung horizontally and tensioned by running them over pulleys and attaching known weights (170 g for anode wires and 280 g for field wires). Opposite wedges are wired simultaneously and the wiring of subsequent pairs of wedges is staggered to avoid uneven build up of stress in the partly wired chamber. Each chamber was wired in approximately 15 working days. The tension of each wire was tested using a resonance technique [13] and any wires not within an acceptable tension range were replaced. Also measured was the precise resistance of each wire which was then recorded in the charge division calibration data base. The tension measurement of each wire was repeated on all chambers after a period of some weeks as a check of stability.

Once wiring was complete, the cathode planes were slid into position and epoxyed in place. The cathode planes control gas flow in the chambers. Gas flows into each chamber through two holes in the shell at the top and out into the tank volume through two holes at the bottom. The top and bottom cathodes separate the chamber into two halves. All other cathodes have a small hole, the position of which alternates between opposite ends of successive cathodes to ensure that flow is along the full length of all wedges. The final gas seal is provided by the tank and the front window, though care was taken to seal the shell to the greatest extent possible to regulate the flow.

The front windows, which close the gas volume and support the front edge of the cathode planes and the front field forming strips, were then attached. Since the RWDCs are to be used to detect transition radiation the RWDC front windows have to satisfy the following conditions.

- They must be gas tight.
- They must be transparent to X-rays.
- Since the probability of a TR photon depositing its energy decreases exponentially with z, they must ensure total ionization collection close to the front of the chamber.

The gas seal is provided by 50 μm Mylar tensioned by bonding it to an inner Noryl ring and an outer ring of resin impregnated wood [11]. Noryl supports for the cathodes are bonded to the inner surface of the Mylar. To minimize X-ray absorption, the front field forming strips are made from 12 μm aluminium, bonded to 25 μm polyester film [14]. As for the back field formers, the strips are 2 mm wide with 3 mm spacing. The field formers are mounted on Rohacell supports which sets them back 5 mm from the Mylar gas window. This gives the necessary uniformity of ionization collection on the front wire as discussed in section 2.2.3.

2.2.2 RWDC Electrostatics

The basic principles of operation of the RWDCs are like those of any drift chamber with only a few small complications due to their unusual shape. It is therefore instructive to look first at a simple drift chamber where the cathodes are mounted parallel to the planes of wires.

The basic principle of operation of any drift chamber can be summarized as follows:

1. A charged track passing through the chamber interacts with the gas in the chamber leaving a number of electron/ion pairs in its path. 100 or so ion pairs are produced per cm for a typical chamber gas.

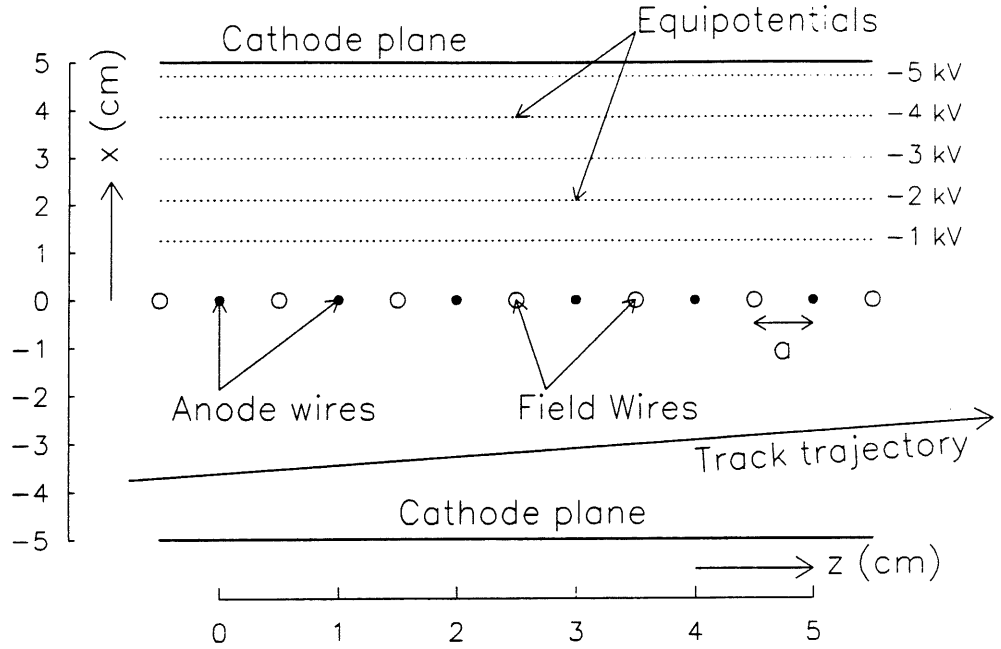

Figure 2.3: A simple drift cell showing equipotentials in the region of linear drift.

2. This small number of ions then drifts towards a plane of anode wires in a uniform electric field at a constant *drift velocity*. It is the measurement of this *drift time* which provides the main spatial information from the chamber.

3. The number of primary ions produced is too small to be easily detected. Therefore, chambers are designed so that there is a region of high electric field close to the anode wires (figure 2.4). On entering this region, more electron/ions pairs are produced by avalanche multiplication (typically a factor of between 10^4 and 10^5) thereby producing a signal large enough to detect electronically.

4. Additional information can be provided if resistive anode wire is used. The charge deposited on the wire will divide between the two ends of the wire in inverse proportion to the impedance to ground at each end. A comparison of the charge collected at each end of the wire will thus give the coordinate of each space point along the length of the wire.

An arrangement capable of meeting the above requirements is shown in figure 2.3. The electric potential inside a such a chamber is given by [15]

$$V(x,z) = V_0 - \frac{1}{2}\left[r_s E_s U(x,z) + r_g E_g U(x, z-a)\right] \tag{2.1}$$

where

$$U(x,z) = \log\left\{4\left[\sinh^2\left(\frac{\pi x}{2a}\right) + \sin^2\left(\frac{\pi z}{2a}\right)\right]\right\} \quad . \tag{2.2}$$

E_s, r_s and E_g, r_g are the surface fields and radii of the anode and field wires respectively. a is the distance between the anode and field wires, x is the distance from the anode wire plane (the drift distance), and z is the distance across the anode wire plane as shown in figure 2.3. If the field wires are grounded (i.e. $V(0, a-r_g) = 0$) then V_0 is given by

$$V_0 \simeq E_s r_s \log_e 2 - E_g r_g \log_e\left(\frac{a}{\pi r_g}\right) \tag{2.3}$$

The voltage on the anodes is then

$$V_s = E_s r_s \log\left(\frac{2a}{\pi r_s}\right) - E_g r_g \log\left(\frac{2a}{\pi r_g}\right) \tag{2.4}$$

and the field at the surface of the field wires is

$$E_g = -E_s\frac{r_s}{r_g} + E_D\frac{2a}{\pi r_g} \tag{2.5}$$

where E_D is the drift field. The cathode voltage is

$$V_{cc} = V_0 - X_{cc}E_D \tag{2.6}$$

where X_{cc} is the distance between the wires and the cathodes.

These equations apply to an infinite array of wires in z. In practice the chamber volume must be closed at each end with field forming strips to maintain the field on the end wires. Field formers are discussed in section 2.2.3

The two most important parameters of drift chamber operation are the drift field and the field at the surface of the anode, controlling the drift velocity and the gas gain respectively. From the equations above, it can be seen that once the geometry of the chamber has been fixed, selecting values for E_s and E_D sets E_g and the relative potentials on the cathodes, field wires and anodes. The potential in the radial chamber for nominal fields E_s = 170 kV/cm and E_D = 1.2 kV/cm are shown in figures 2.4 and 2.5. It can be seen that the arrangement shown in figure 2.3 gives rise to a constant

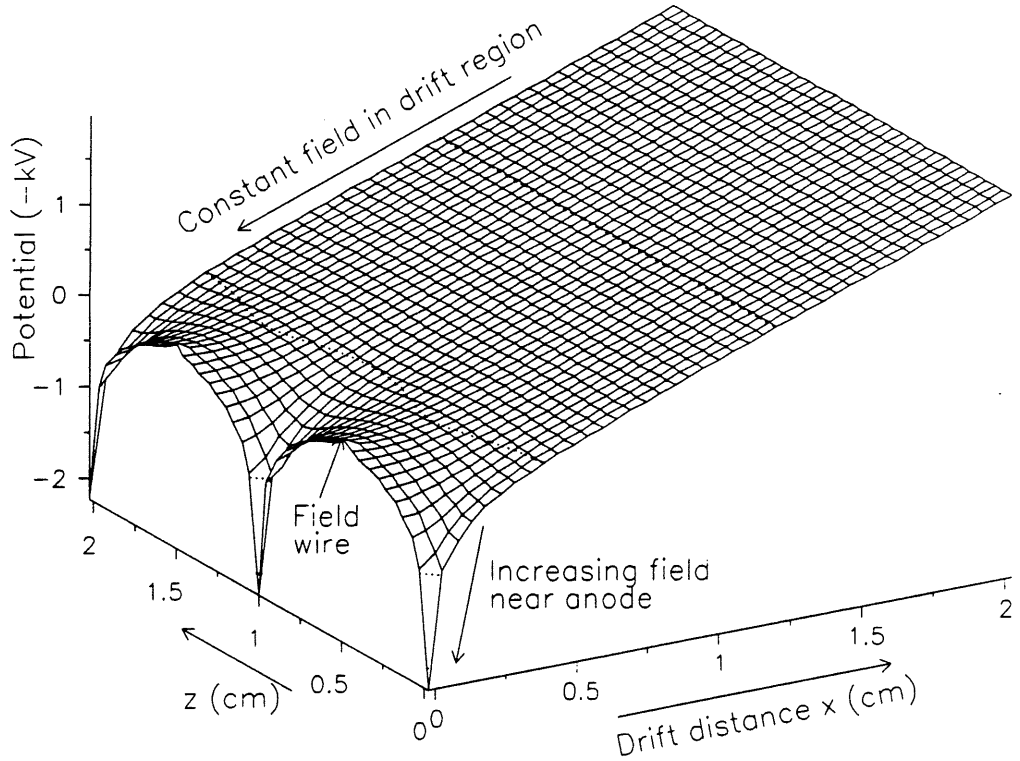

Figure 2.4: Electric potential in a drift chamber cell.

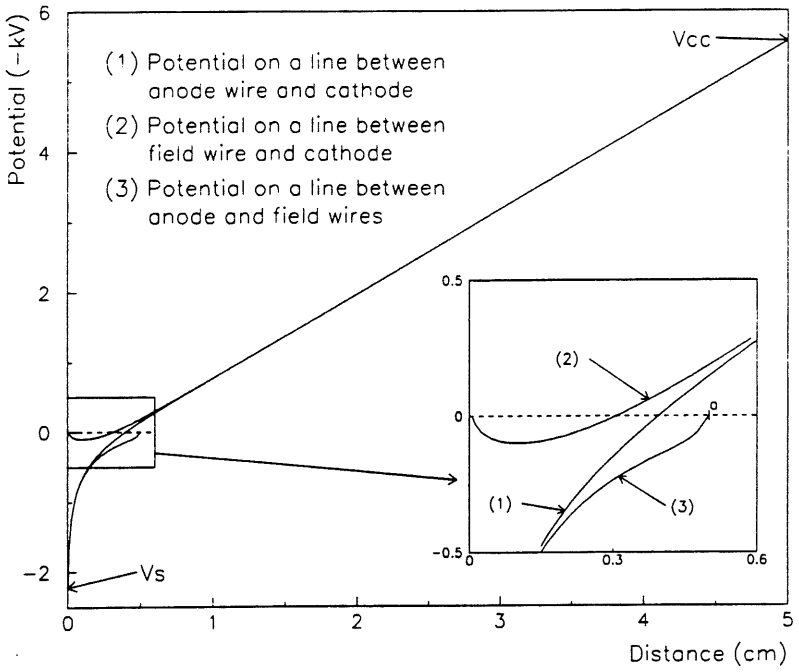

Figure 2.5: Details of the electric potential in a drift chamber cell. Three lines are drawn showing the potential on a line between an anode wire and a cathode plane, between a field wire and a cathode plane, and between an anode wire and a field wire.

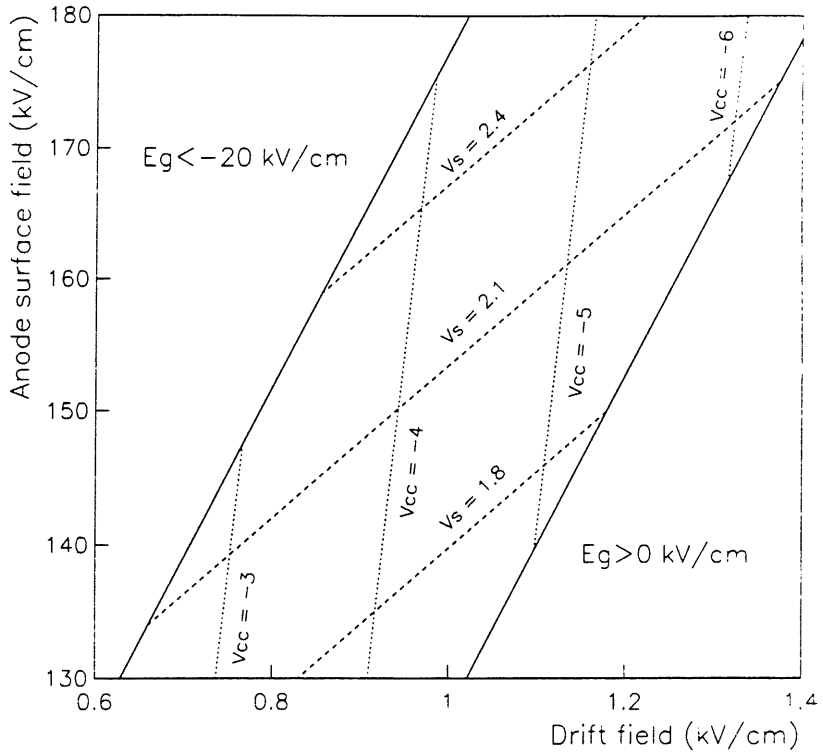

Figure 2.6: RWDC operating conditions. V_s and V_{cc} are the anode and cathode potentials given in kV.

field at distances > 0.6 cm from the wire plane for all values of z. Close to the anodes, the field increases rapidly and becomes radially symmetric at the anodes surface.

In order to satisfy the condition of total ionization collection it is important that there be a negative field at the surface of the field wires (E_g) to prevent electrons from collecting there instead of on the anodes. In fact, a slightly negative field is desirable to focus the electrons towards the anodes. If, however, the field becomes too negative there is the possibility of field emission from the surface of the wires. Operation is therefore limited to a corridor in the E_s/E_D plane defined by -20 kV/cm$< E_g < 0$ as shown in figure 2.6. Also shown in figure 2.6 are lines of constant anode voltage V_s and the cathode potential V_{cc} for a wire plane – cathode spacing of 5 cm.

2.2.3 The Radial Wedge in Practice

The radial wedges differ from that in figure 2.3 in two ways. The first is the obvious taper of the wedges. This has very little effect on the overall electrostatics since the

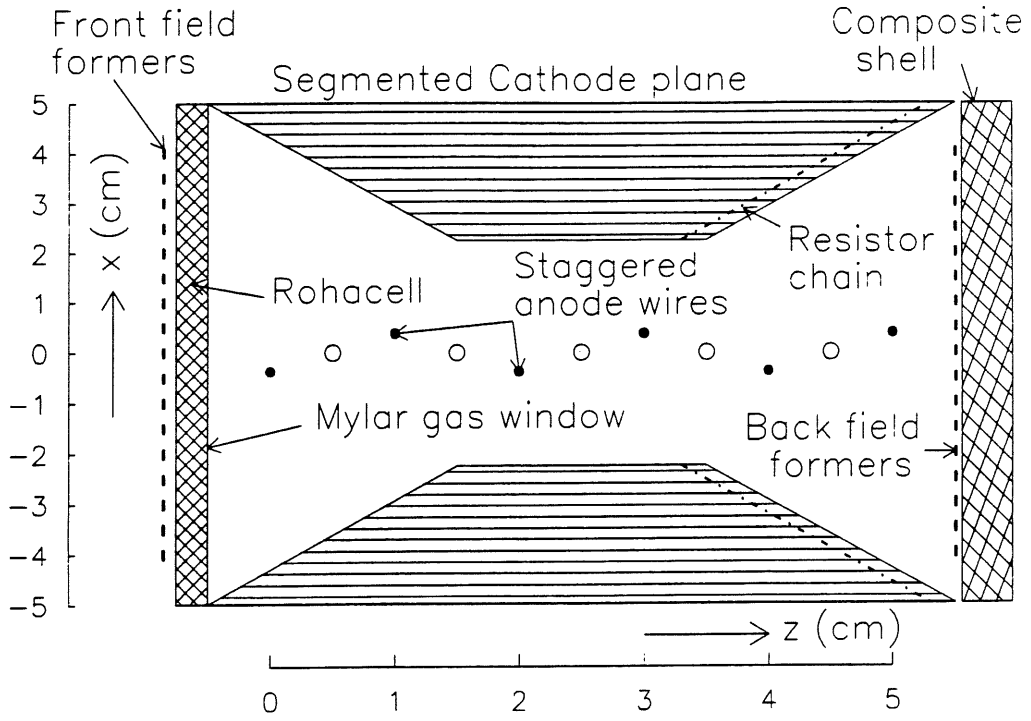

Figure 2.7: Schematic view looking down a RWDC wedge towards the beam pipe.

cathode potential is graded along its length in such a way that equation 2.6 is still satisfied at all radii. The cathodes in the RWDC wedges are divided into 86 strips in r, each 6 mm wide with 1 mm separation. They are connected by a chain of 85 x 10 MΩ resistors connected to a different high voltage supply at each end to provide the linear change in potential necessary for a constant drift field. The second departure is that the anode wires are alternately staggered about the central position by $\pm 287\,\mu$m. This enables pattern recognition software to recognize rapidly which side of the wire plane the track is on during track reconstruction. A schematic view down a radial wedge (only showing 6 of the 12 anode wires) is shown in figure 2.7

The conventional place to put field forming strips is inside the gas volume on the walls of the chamber. A consequence of this is that the charge on the strips attracts electrons which are drifting close to the chamber boundaries which then collect on the strips, never reaching the anode wire. Since charged particles deposit ionization along the whole of their track length this can be easily compensated by a slight increase in the depth of the end drift cells. Ionization deposited close to the boundaries is lost but is compensated for by the extra depth. This has been implemented at the back of the

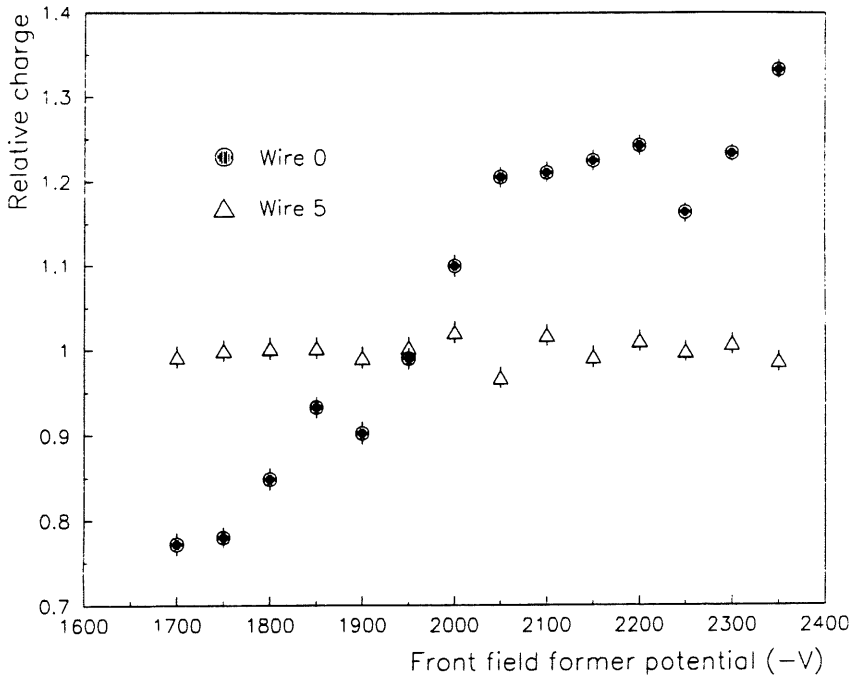

Figure 2.8: The variation of gas gain on the front wire of a RWDC with the voltage on the central front field forming strips in Ar:C_2H_6 50:50 gas mixture.

RWDCs where the distance from the back anode wire to the field formers is 8 mm (as opposed to the 5 mm spacing between adjacent anode and field wires). The potential on the central strip of the back field formers may be set independently to allow fine adjustment of the field in this region.

Transition radiation X-rays entering the chamber do not leave tracks, but deposit all of their energy at one point in the chamber. Since the most probable place for this to happen is near the front of the chamber, the arrangement outlined above would not be suitable for efficient TR detection, so that described in section 2.2.1 was adopted. The Mylar gas window is positioned 5 mm upstream of the first anode wire to conserve the periodicity of the cells. Setting the field forming strips back a further 5 mm ensures that the region in which the field is distorted lies safely outside the gas volume. As a further refinement, the potential on the central three strips may be set independently to make fine adjustments to the field in this all important region. Figure 2.8 shows how the relative mean charge deposited on wire 1 and wire 5 of a RWDC wedge in Ar:C_2H_6 50:50 gas mixture varies with the voltage applied to the central strips of the front field formers. The data were taken using a 50 GeV electron beam with no transition radiator

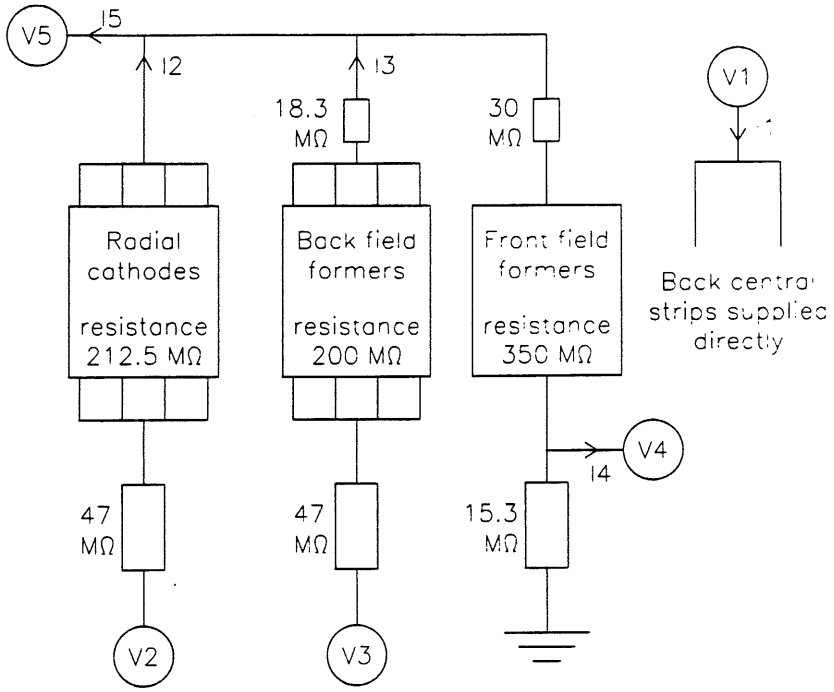

Figure 2.9: The high voltage supply to a pair of RWDC wedges. The five voltages V1 to V5 are defined in the text.

in front of the chamber.

Each radial wedge requires 6 different HV supplies. The supply points are:

V0 Anode wires.

V1 The central strip of the back field formers.

V2 The end of the cathodes closest to the hub.

V3 The inner back field former strips (i.e. the ones on either side of the central strip).

V4 The inner 3 front field former strips (which are connected together).

V5 The outer end of the cathodes.

The outer strips of the back and front field formers are connected to the same supply as the outer ends of the cathodes via resistors selected to drop the voltage on the strips slightly since the outer most strips do not lie at the same drift distance as the end of the graded cathodes. The drift cages of adjacent wedges are powered in pairs.

This is a compromise between being able to switch off individual wedges in the event of problems and introducing too much material into the detector in the form of extra HV cables. Connections between adjacent wedges and the above-mentioned resistors are made on small printed circuit boards or 'spider cards' glued onto the outside of the composite shell. Four cathode and four back field former resistor chains (two cells $\times$ two sides to each cell) are therefore connected in parallel for each wedge pair with resulting resistances of 212.5 MΩ and 200 MΩ respectively (figure 2.9). The front field formers are constructed in units which cover two wedges and contain a single resistor chain to provide the necessary potential gradients over both of them.

2.3 RWDC Infrastructure

2.3.1 High Voltage Supply

Due to the coupling of pairs of RWDC wedges at the hub, it is only necessary to power directly the anodes in half the wedges. Two HV supplies per chamber are each fanned-out 12 ways in a crate which also monitors the current [16]. A third (and space for a fourth should the need arise) supply and current monitor/fan-out is also available for each chamber to be used in the event of problems in a particular wedge.

The arrangement of the HV supply to a pair of wedges is shown in figure 2.9. Even with the wedges powered in pairs, the three radial chambers still require a total of 360 HV supplies for all of the drift cages. To reduce the number of HV supplies to one crate per chamber, each HV supply is fanned-out 8 ways for the front and back field formers, the back central field former strip, and the inner ends of the cathodes and 4 ways in the case of the outer ends of the cathodes since the HV supplies can not provide sufficient current to simultaneously supply the cathodes of 8 wedge pairs. The final drift cage requirements per chamber are therefore 6 supplies to the outer end of the cathodes and 3 to each of the other points. In order not to lose flexibility if any wedge pairs have to be turned off, enough spare HV supplies are available for each chamber such that a few 'funny' wedges on each chamber may still be powered separately (or left disconnected. or grounded) if required.

The high voltage supply [17] contains modules which can supply either positive *or* negative voltages. There is a limitation that positive supplies can only source current and negative supplies can only sink current. The end of the cathodes closest to the hub must be at a negative potential and at the same time act as a current source driving towards the more negative potential at the outer ends of the cathodes. To overcome this problem a 47 MΩ 'tail resistor' is connected between the inner end of the cathode and a positive supply. The resulting voltage drop across the cathode permits the positive supply to source current and still produces a negative potential at the end of the actual cathode. A similar arrangement is used for the back field formers. For the front field formers, a 15.3 MΩ resistor to ground sources current into negative supplies at both ends of the resistor chain. Tail resistors are all contained in the fan-out crate mounted close to the HV supplies. Since the values of the tail resistors effects the voltage applied to the ends of the cathodes, for uniformity of operation, resistors were carefully selected to be of the same value in each fan-out unit.

The HV requirements of each complete RWDC are summarized in table 2.1. If only a single front field former is connected, less current flows down the field formers. Since the potential across, and hence the current in the 15.3 MΩ resistor, is constant, considerably more current flows into the supply if only one wedge is connected.

High voltage feedthroughs in the gas tank form the connection between the spider cards and the external cables. Each feedthrough contains two specially designed connectors each of which connects all 5 drift cage HV supplies for a wedge pair. Twelve such feedthrough blocks are therefore required per chamber.

To avoid earth loops, which are a common source of electrical noise, the HV supplies to all FTD components are isolated from ground. This has been achieved by physically insulating all HV supply units and fan-out crates from the equipment racks and isolating the mains supply with a transformer. Care was taken during the installation of the trackers that the FTD did not make contact with either the cryostat walls or the CTD. Communications cables between the HV supply and the H1 control room contain opto-isolators. The only earth connection on the FTD is then via the signal cables between the preamplifiers and the FADC crates. The FTD tank is a common ground for all

Supply point	Number of supplies required	fan-out	Voltage (V)	Current per wedge pair (μA)	Current per supply (μA)
V1	3	x8	+500	0	0
V2	3	x8	+291	22	176
V3	3	x8	+963	24	192
V4	3	x8	-2000	122	59
V5	6	x4	-5413	55	220
Anodes	2	x12	+2228	0	0

Table 2.1: HV supply requirements of a RWDC for nominal operating conditions (E_S = 170 kV/cm and E_D =1.2 kV/cm). The supply points V1-V5 are defined on page 32.

FTD components.

2.3.2 Gas System

The gas system [18] for the RWDCs performs the following tasks:

- It controls accurately and safely the pressure difference across the fragile RWDC front window.
- It has the facility to prepare and analyze the gas mixtures required by the RWDCs
- It removes impurities from the gas.

Gas is circulated in a closed system which recycles the gas, purifying it by means of deoxo purifiers and a molecular sieve. The entire system is computer controlled and regulates the pressure across the RWDC front window to $\pm 50 \mu$bar. The gas is analyzed using an infra-red meter to measure the C_2H_6 concentration and a gas chromatograph to measure impurities. When helium gas is used its concentration may be monitored by measuring the partial pressure between 2 manometers at different heights.

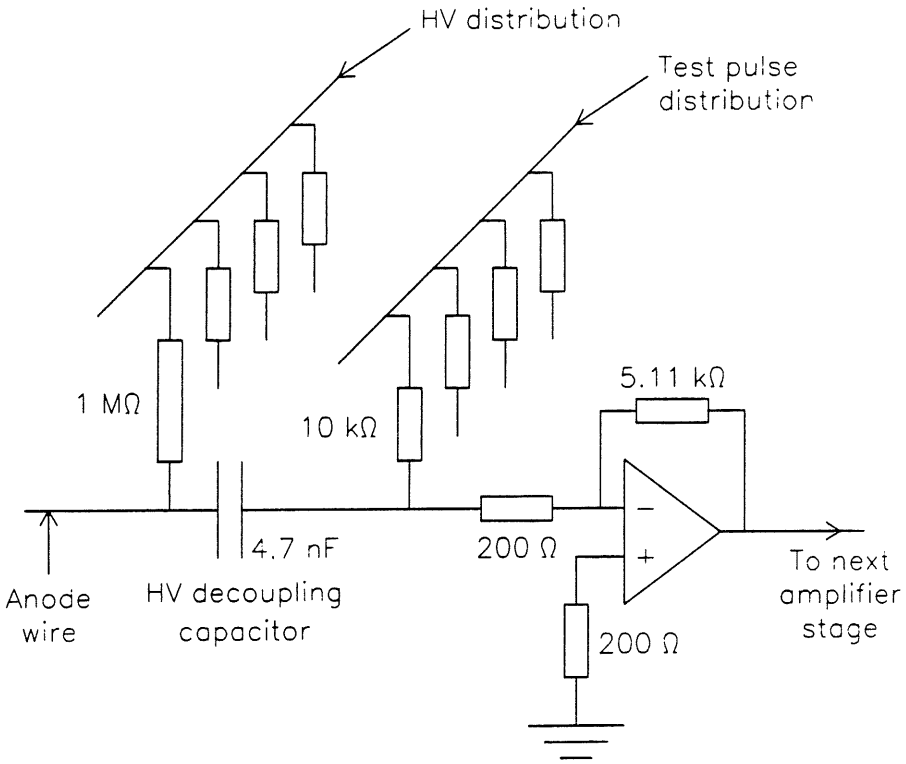

Figure 2.10: The main features of the preamplifier input circuit.

2.3.3 Preamplifiers

Preamplifiers [19] are mounted on the outside of the FTD tank as close as possible to the ends of the wires. The preamplifier cards also distribute HV to the anodes and contain the HV decoupling capacitors. The main features of the preamplifier input are shown in figure 2.10. The input impedance of this type of circuit is simply that of the 200 Ω input resistor. The preamplifier output is differential (i.e. two output signals one of which is inverted) which is a common technique used to make the signals less susceptible to pick up in the 40 m long cables from the experiment to the FADC crates. The two signals are subtracted from one another at the input to the FADCs resulting in the signals adding and any common noise cancelling out.

Each preamplifier card contains 8 identical channels, the properties of which are summarized in table 2.2. Since $1\frac{1}{2}$ cards are required for the 12 wires in each RWDC wedge, high voltage distribution is grouped into 2 sets of 4 channels on each card. These are then linked into groups of 12 channels with short lengths of HV cable after mounting on the tank. Test pulse inputs are provided to allow calibration of the

Gain	105 mV/μA
Power consumption	175 mW/channel
Rise time	10 ns (10 %/90 %)
Noise	15 mV_{p-p}
Input Impedance	200 Ω
Cross Talk	<0.5 %
Non-linearity	<0.5 %
Test pulse sensitivity	0.03 V/V
Repetition rate	1200 kHz

Table 2.2: Preamplifier specifications.

individual channel gains and cable delays both inside the tank and in the signal cables to the FADCs. Two test pulse inputs are provided, one for odd numbered channels and one for even.

The preamplifiers connect the FTD earth from the FADC crates by means of the output signal cables to the tank. Due to the large amount of power dissipated by the high gain preamplifiers used (a total of $\sim$ 500 W for all RWDC and PWDC channels) the preamplifier mountings are attached directly to water cooling pipes on the tank.

2.3.4 Read-out and Data Acquisition System

All H1 drift chambers are read-out using 104 MHz, 8 bit, non-linear FADCs [20]. The non-linearity increases the size of small signals entering the FADCs relative to larger ones as shown in figure 2.11.a. Digitizing a signal introduces an RMS noise equivalent to $\frac{1}{\sqrt{12}}$ times the digitization step size[†]. The non-linearity reduces the step size at small signal levels and increases it for large ones. The signal to noise ratio is thereby improved for small signals at the expense of larger ones (figure 2.11.b).

Each FADC chip writes into a region of memory 256 time bins deep. They operate

[†] The error on each digitization is evenly spread between $\pm\frac{1}{2}$ of the digitization step size (i.e. a 'top hat' function). The rms variation of such a distribution is $\frac{1}{\sqrt{12}}$.

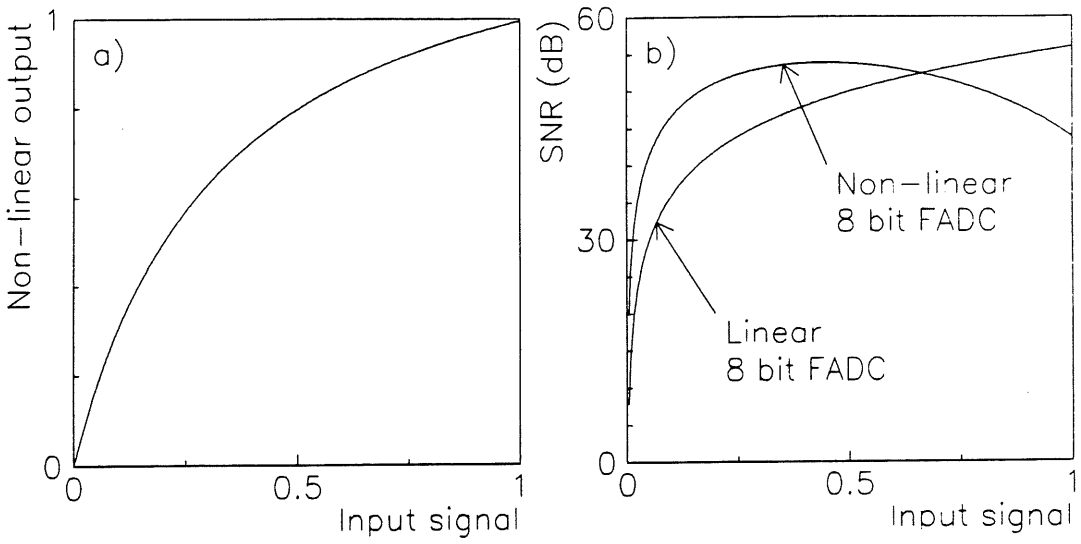

Figure 2.11: FADC non-linear response, a) The non-linear response function, b) Signal to noise ratio (SNR) for 8 bit linear and non-linear FADCs.

in 'common stop' mode. That is, they run continually, re-writing over the same memory until a STOP signal is received from the H1 trigger. The advantage of 'common stop' over the 'common start' mode of operation is that the trigger signal may arrive at the crate up to 2.5 μs later than the earliest part of the pulse from the chamber thus allowing time for the first level trigger logic to operate. Once a 'STOP' signal has been received, no further data can be taken until the contents of the memory have been transferred. Each crate is therefore equipped with a dedicated hardware processor (the scanner) [21] which takes digitizations from FADC memory and scans them for pulses which rise above some predetermined threshold for 2 or more consecutive time bins.. Only these regions of data plus a number of digitizations before the start of each pulse for baseline determination are passed to the next stage of the Data Acquisistion System (DAQ). The effect of this initial stage of data reduction is to clear the memory and restart the FADCs in approximately 0.8 ms.

The backplanes of the FADC crates are VME based, making them readily compatible with the rest of the DAQ and with other systems (such as the Apple Macintosh used during cosmic ray and test beam studies). Each crate contains 16 cards each of which has 16 FADCs. Each RWDC therefore requires $2\frac{1}{4}$ crates. For simplicity and flexibility of operation three crates are used for each chamber, the empty slots being

evenly distributed between them. The standard length of a word in the H1 DAQ is 32 bits. To avoid redundancy in data transfer and storage, four 8 bit quarter-words containing the data from from both ends of two wires are included in a single 32 bit word which is then separated during later analysis. The FADC system also sends test pulses and provides power to the preamplifiers along the same cables as those used for the signals.

Data from the FADCs are transferred to the front end processor (FEP) where the pulses are analyzed to determine drift times and pulse integrals. The raw digitizations may then be discarded resulting in a further 75 % reduction in the volume of the data before it is transferred to permanent storage via the DESY central computer. Currently four separate processors analyse the pulses. In the future it may be necessary to have one processor per FADC crate to further speed up this analysis when HERA reaches its full design luminosity.

2.4 Testing, Installation and Commissioning of the RWDCs

Extensive tests were carried out of the mechanical and electrical properties of the RWDCs at all stages of construction and installation in order to achieve the required stability of performance in H1.

2.4.1 Liverpool: 1989 - 1990

The three RWDCs were constructed in Liverpool before being installed into the FTD tank at the Rutherford Appleton Laboratory (RAL). Tests of the mechanical stability have already been described in section 2.2.1. Since the FTD tank forms the gas envelope for the RWDCs and contains all the high voltage feedthroughs to the chambers, a complete test of all RWDC wedges was not possible. Instead, a simple test stand was constructed which enabled connection and read out of only four RWDC wedges at any one time. The wedges were read out using a 6 bit non-linear FADC system [22] and some 2000 cosmic ray tracks were recorded in Ar:C_2H_6 50:50 gas mixture. Analysis of

these tracks showed that the chambers were performing to specification, with a drift coordinate precision better than 200 μm.

Due to the large volume of the RWDCs compared to the available gas flow rate, it would take several days to remove all the Ar:C_2H_6 from the chambers, re-connect to a new set of wedges, replace the chamber gas and collect data. It was therefore not possible to test all wedges in chamber gas. To ensure high voltage stability, all wedges were tested in air at voltages 60 % higher than the nominal Ar:C_2H_6 50:50 operating conditions require.

2.4.2 RAL: December 1989 - July 1990

Once testing of each chamber was completed in Liverpool, it was transported to RAL and installed into the FTD tank. Before installation, to check that no damage had occurred during transport, the resistances of the anodes were re-measured as a check both of continuity and of the stability of the wire support crimps, and the chambers were again subjected to the same high voltage tests in air. Before installation the precise relative positions of all the wires in each chamber were measured using the facilities of the RAL survey group to an accuracy of ± 5 μm, confirming that construction in Liverpool had been performed to the accuracy of $\sim 40\,\mu$m. Survey data have been used to produce precise calibration tables for track reconstruction.

The greatest difficulty during installation into the tank was the gas seal between the wooden bezel of the RWDC front window and the FTD tank. It was found that gas was leaking between the laminations of the wooden bezel so Mylar was epoxyed over it to improve the seal on each chamber. The ideal gas for TR detection contains 30 % Xenon so leaks across the window would not only introduce gas into the RWDC from the radiator volume, but would be expensive as well. The seal was tested by flushing the radiator gas volume with He gas with the RWDCs themselves still full of air. Measuring the oxygen content in the He output flow gave an indication of the leak rate across the window. The advantage of this method was that while the leak test was under way, work could proceed with connecting the crimp pins holding the RWDC wires and the cables for the drift cage to the high voltage feedthroughs mounted on the

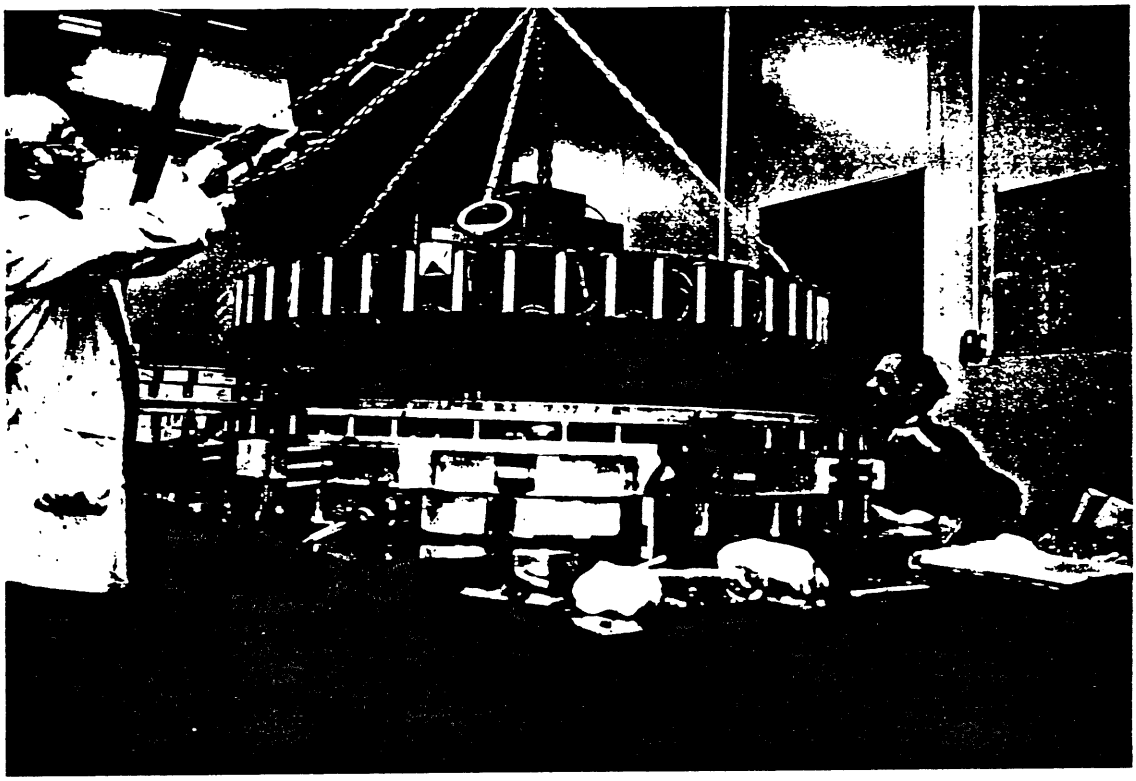

Figure 2.12: Assembly of a FTD supermodule at RAL. The supermodule is face down, i.e. the PWDC is closest to the table, and a leak test of the PWDC/MWPC gas volume is taking place. Signal and HV feedthroughs for the MWPC are protected by polystyrene blocks. The transition radiator is just visible at the top of the tank above the channel which contains water cooling pipes. A RWDC is being lowered into position. Clearly visible on the outer surface of the RWDC are the Noryl blocks which support the wire crimps and the (pale green) HV distribution boards. It is also possible to make out the wooden bezel and light reflecting from the RWDC front field formers.

tank.

In the final assembly, all three super modules are connected with a 100 μm Mylar separator between successive units. Dummy end caps were available for testing at RAL so that testing work could proceed on the first module while the second and third were still under construction.

Due to delays in the arrival of the complete high voltage system, it was still not possible to power all wedges on a supermodule simultaneously at RAL, though the number of wedges powered at any one time was increased from 4 to 12. This was not

as much of a problem as in Liverpool since connections only had to be re-made on the outside of the tank, which required no interruption to the gas flow and could be done in minutes rather than days. The best indicator of the high voltage stability of a RWDC is the current drawn by the anodes. The current monitoring system gave the current in each wedge pair to ± 5 nA. It was found that, although initially low, after some hours the current would sometimes start to increase from $\sim 10 - 20$ nA to $\sim 1\ \mu$A, at which point the HV supply would trip off automatically. This happened on most wedges and was thought to be due to the high potential gradient across RWDC cathodes when one wedge is powered and the adjacent one not. Small amounts of ionization produced at the corners of the cathodes could drift towards the anodes where the effects of gas gain would produce substantial currents. This phenomena was not observed in Liverpool because firstly, the accurate current monitor was not available and secondly, the oxygen concentration during tests in Liverpool was $\sim$0.3 % (as opposed to 0.02 % at RAL). Oxygen absorbs drifting electrons and would therefore have hidden this effect.

Cosmic ray data were taken at RAL on a part of a completed supermodule using the final H1 FADC system complete with scanner. Analysis of the tracks confirmed that the RWDCs were still working to specification and enabled work to start on linking RWDC and PWDC track segments in the FTD reconstruction software.

2.4.3 DESY Surface Tests: August-December 1990

The completed FTD was shipped to DESY in August 1990. On arrival the FTD was re-tested on the DESY main site and attached to the CTD and the cables put on before being transported to the H1 pit. Measurement of the resistances through the chamber anode wires confirmed that no damage had occurred during transport. The arrival of the first installment of the completed high voltage system also allowed testing of a complete supermodule for the first time. As had been hoped, the high currents observed at RAL did not reappear, confirming that they were due to the effect of not powering all of the RWDC wedges and should not therefore cause problems in the full operation of the chambers. The first problem to occur at this stage was electrical breakdown of some of the high voltage capacitors which isolate the anodes from the preamplifier

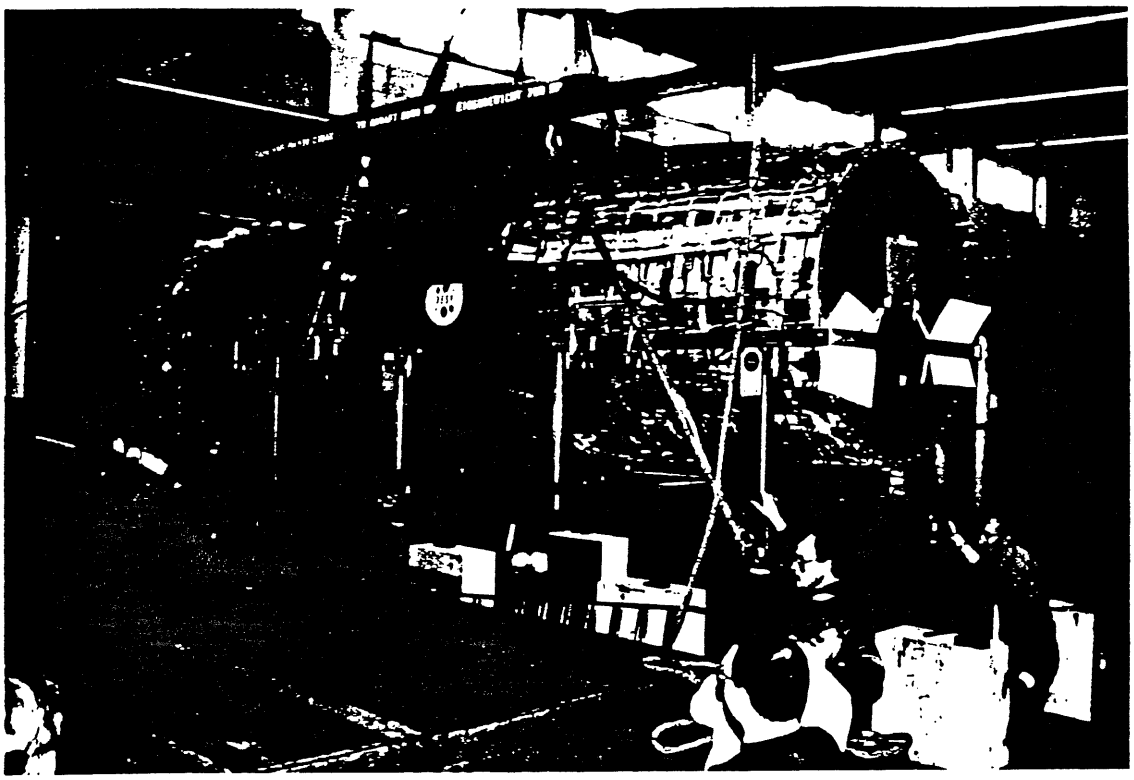

Figure 2.13: The complete tracking detector during transport to the H1 pit. The FTD is to the right of the picture. In the middle is the CTD (marked with the 'DESY' sticker). Cables from the FTD run over the CTD and were held during transport on a special support which can be seen to the left of the picture.

inputs. Faulty preamplifiers were replaced and there have been no failures since, so it seems that the problems were due to a few individual capacitors being faulty rather than to any degradation with time.

During this period, it was found that there was a break in the resistance chain of one of the cathode planes and that the anodes in another of the wedges persisted in drawing high currents. Since both of these faults were in the same supermodule it was considered worthwhile to make the repair before proceeding with the final installation. The break in the resistor chain turned out to be a bad solder joint at the point where the high voltage supply is attached to the outer end of cathode. The break-down in the other wedge was attributed to a length of anode wire which had become coiled up in the composite shell at the point where the anode wires pass through the shell to

the templates. The very end of the coil was sparking onto the nearby field forming strips. Although the repairs themselves were trivial and took only a matter of hours, taking apart the tank, re-assembling it and re-testing the complete FTD took a total of 4 weeks.

Once all repairs and tests were complete the FTD was attached to the front end of the CTD. FTD cables were attached and laid over the top of the CTD and onto a support structure which held them during transport to the H1 pit. Connections between the preamplifiers and the chamber and the preamplifiers and the readout signal cables were checked by using test pulse inputs to the preamplifiers. Pulsing the amplifier at one end of the wire would produce a signal at both ends, the ratio of the size of the pulses being the same as for a real signal undergoing charge division at this point in the chamber. This test therefore also confirmed the continuity of the anode wire connections through the chamber.

2.4.4 Installation into the H1 Experiment: Spring 1991

The completed charge track detector was transported to the North Hall at DESY on January 28, 1991. Before the final installation into the H1 cryostat, test pulses were once again used to confirm the continuity of connections to the chamber.

The cables were then attached to the Cable Distribution Area (CDA) where further cables (already in place) connected to the HV supplies and FADCs in the rucksacks on the side of the detector. Again, test pulses confirmed the continuity of the connections and a number of connections at the CDA were repaired. Once the gas content of the chambers stabilized, high voltage testing started. As for the signal cables there were a number of errors at the CDA panel which had to be repaired. It was quickly established that the second and third supermodules could hold volts over an indefinite period. However, one of the wedges on the middle supermodule, although initially stable, developed a problem with one of the cathode high voltage supplies and tended to trip out after a period of up to 24 hours. It is not known whether this is due to a genuine problem in the chamber or a fault in the external cabling in the inaccessible region between the CDA and the FTD. This wedge has now been connected to a

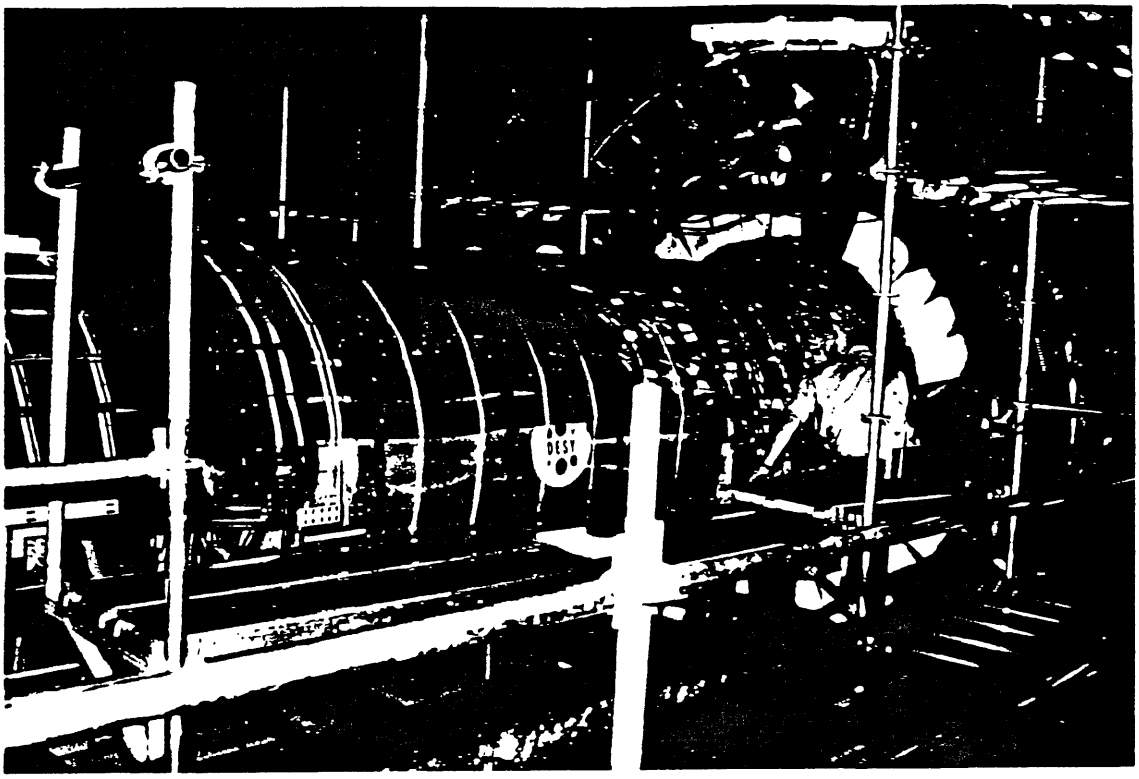

Figure 2.14: The complete tracking detector waiting installation into the H1 experiment which is to the right of the picture. Once the tracker had been pushed in on rails on the inside of the cryostat, the cables were removed from the support frame and attached to the cables which can be seen on the experiment.

separate supply and is currently operated at 80 % full volts.

Over the summer of 1991 H1 took cosmic ray data both with and without the 1.2 Tesla magnetic field. The flux of cosmic rays passing through the FTD at angles close enough to the horizontal to be useful is small, but enough were collected to again confirm that the RWDCs meet specification and, furthermore, that they can do so along with the added complications of a magnetic field.

On December 4, 1991, one of the wedges in the middle super module was found to be breaking down even at very low voltages on the anodes. The resistance to ground from the high voltage supply is entirely consistent with a short circuit between an anode and an adjacent field wire. Furthermore, test pulses have shown that there is no longer continuity along one of the wires in that wedge. This can only indicate that one of

the anode wires has broken and that the broken ends are now in contact with the field wires.

The current status is therefore that all wedges in the second and third supermodules are operating normally. In the middle supermodule, two wedge pairs have problems. One associated with a cathode; the other appears to be a broken anode wire. These two wedges are in separate regions of the chamber and the problems are not thought to be in any way connected.

Chapter 3

RWDC Test Beam Studies: Set-up and Analysis

3.1 Introduction

The performance of a complete RWDC has been studied using the fixed target (X5) e^- and π^- beam from the Super Proton Synchrotron (SPS) at CERN. The principal differences between this study and earlier tests of prototype radial wedges [10, 23] were that it was the first test of a full sized H1 chamber. It was the also the first test of a RWDC with both pions and electrons, previous tests having taken place at DESY where only electron beams are available.

A total of two million triggers were taken during a 14 day period. A summary of the chamber operating conditions and gas mixtures used is shown in figure 3.1. In each gas mixture, data were taken using both electrons and pions at momenta between 5 and 50 GeV/c. The data taken during the tests enabled a thorough investigation of all aspects of space point determination in RWDCs as well as a measurement of the e/π discrimination in the chambers.

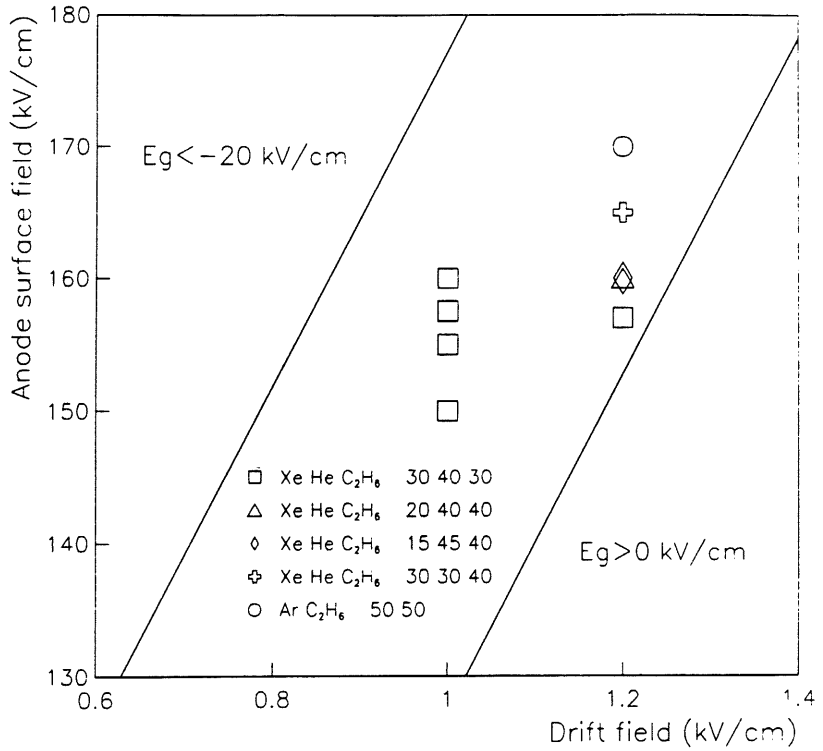

Figure 3.1: Operating conditions and gas mixtures used during tests at CERN.

3.2 The CERN X5 Beam

The X5 beam is a tertiary beam derived from the CERN SPS. The SPS provides a 2.56 s long burst of particles to fixed target experiments every 14.3 seconds, the time between spills being used to accelerate the next burst of protons and to accelerate electrons and positrons for injection into the Large Electron Positron collider (LEP).

In the production of the X5 beam, 450 GeV/c protons extracted from the SPS are directed onto the T1 primary target. Typical intensities at this point are 3×10^{12} protons per burst. Two secondary beams are derived from T1, one of which is split into 3 beams, each containing $\sim 10^7$, 120 GeV, negative particles (mainly pions and electrons). This secondary beam is directed onto either a copper or a lead target depending on what type of tertiary beam is required. A lead target produces a pure electron beam, pions are obtained from a 40 cm long copper target. Below energies of $\sim$ 50 GeV the pion beam is no longer pure. Lead absorbers may be used to absorb hadrons in the beam at intermediate energies of 20 to 50 GeV, at lower energies Cherenkov counters must be used in the experiment trigger to select a specific particle type (section 6.3.1). Two

counters containing He and N_2 gas were available, their different densities being suitable at different energies. The purity of the pion beam and the efficiency of the Cherenkov counters is discussed in section 6.3.1.

The beam momentum is determined by the current in two dipole bending magnets placed downstream of the second target. Any particles with momenta too far above or below the nominal value will be steered into collimators which define the momentum spread. The range of momenta available from the X5 beam is 5–100 GeV/c. Typically, with the collimator jaws set 5 mm apart, the spread in momentum $\Delta p/p$ is approximately 1 % [24]. The beam spot is approximately 1 cm in diameter.

3.3 Test Set-Up

The RWDC was mounted in a gas tank with sufficient instrumentation for 4 pairs of wedges to be read out. The gas tank was mounted on a traversing support (figure 3.2) which could be moved perpendicular to the beam axis and rotated about a vertical axis to allow illumination of different regions of the chamber. Data were read out using final H1 FADCs connected directly to a Mac II enabling a maximum trigger rate of up to 300 events from each spill from the SPS. Scintillators in front of and behind the RWDC provided a trigger and event drift time origin. The position of the beam was monitored using a beam position wire chamber mounted close to the end of the beam pipe (section 3.3.2.1). A photograph and a schematic layout of the RWDC in the CERN beam line are shown in figures 3.2 and 3.3.

With a beam spot $\sim$ 1 cm in diameter, it was not necessary to provide enough transition radiator to completely cover the front of the RWDC. A small piece of radiator was mounted against the front of the chamber when required during the tests. Polypropylene foils of exactly the same dimensions as the H1 FTD radiator were available as well as the polypropylene fibre radiator used in earlier prototype tests [25]. In H1 the radiator is flushed with a mixture of He and C_2H_6. During the tests, gas containment was not available for the radiator which was therefore in air (just as for previous prototype tests). The effect of this would be a slightly lower yield of TR photons and thus a higher pion contamination.

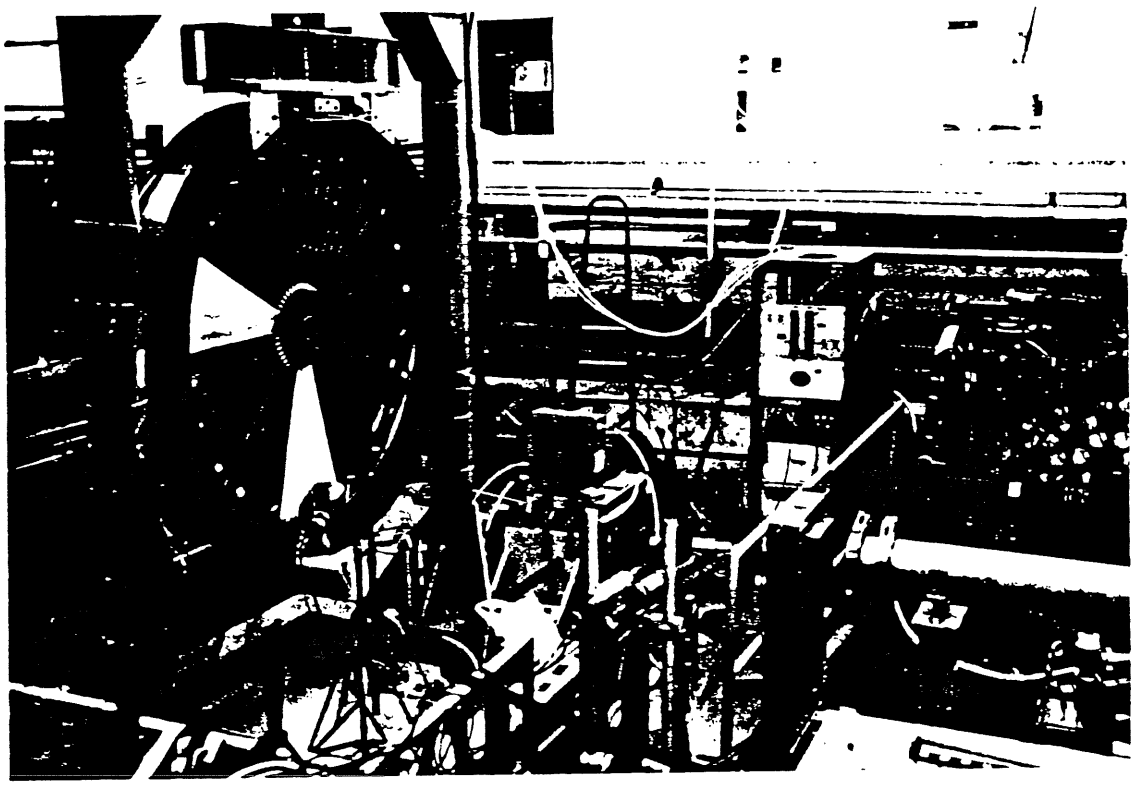

Figure 3.2: Photograph of the CERN test beam area.

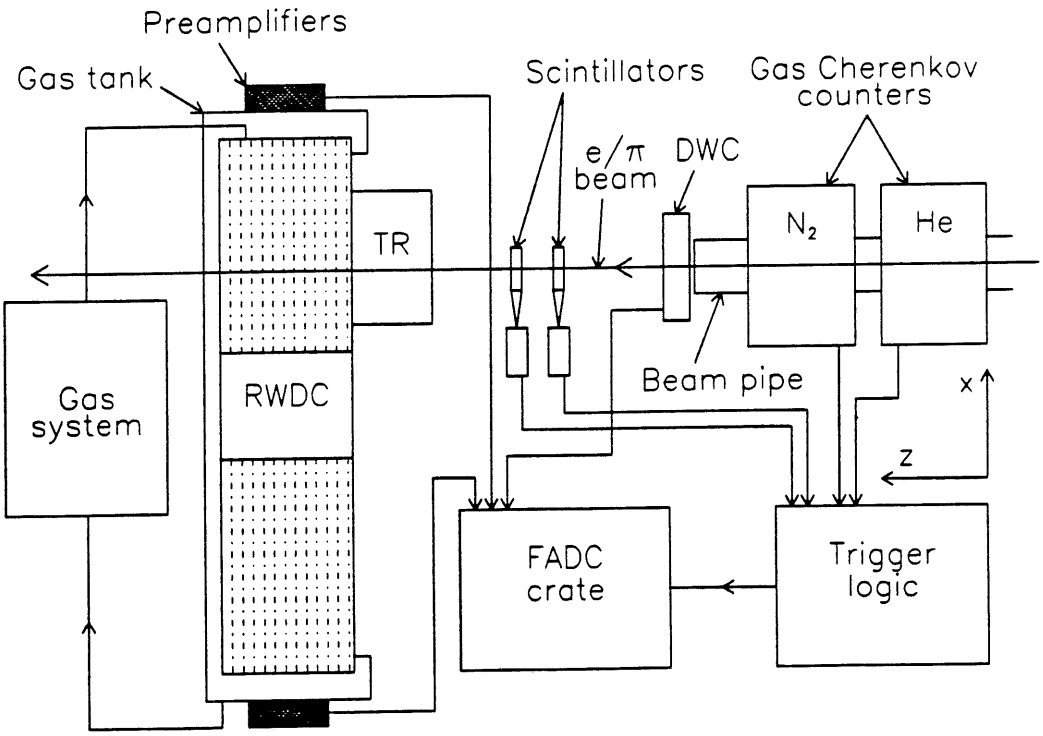

Figure 3.3: Schematic layout of the CERN test beam area.

High voltage supply was identical to the final H1 set up with the cathode planes adjacent to the read-out wedges powered to half the nominal operating potential to avoid the problems of high voltage stability discussed in section 2.4.2. A fully automatic system capable of performing all of the functions outlined in section 2.3.2 was used in a closed loop mode to supply gas to the chambers. Test pulse data were also taken at CERN to allow the same calibration of the chambers as at H1 (see section 3.5).

No magnetic field was available for these calibration tests. In a magnetic field, electrons no longer drift parallel to the electric field but at an angle (the so called 'Lorentz angle') varying between $\sim 30°$ and $\sim 45°$ in Xenon and Argon based gas mixtures respectively.

3.3.1 Trigger and Drift Time Origin

The trigger performed two tasks during the tests. The first was to initiate readout as a particle passed through the chamber. The second was to provide a reference time for drift time measurements in the chamber.

The basic trigger consisted of either 3 or 4 scintillators, two of which were positioned close to the beam pipe, one was behind the RWDC and, when TR was being used a fourth was mounted close to the transition radiator to ensure that particles could not cause a trigger without first traversing the radiator foils. (When the radiator was not in place and scans were being made across the chamber this scintillator was removed to allow free movement of the support). Accurate timing was achieved by delaying the arrival of the discriminated signal from the smallest scintillator so that it was the last to arrive at the trigger input which formed an AND of all scintillator signals. The accuracy of the drift time origin was then limited only by the timing jitter on that scintillator which would tend to be less than on larger ones where there is an indeterminate propagation time of the light across the scintillating material.

The H1 FADCs are designed to work synchronized to the HERA clock. A result of not having this clock available is a random delay of up to 96 ns (1 HERA bunch crossing) from the true time of the trigger signal arriving at the FADC crate to the time at which the FADCs actually stop. To avoid this potentially large timing error

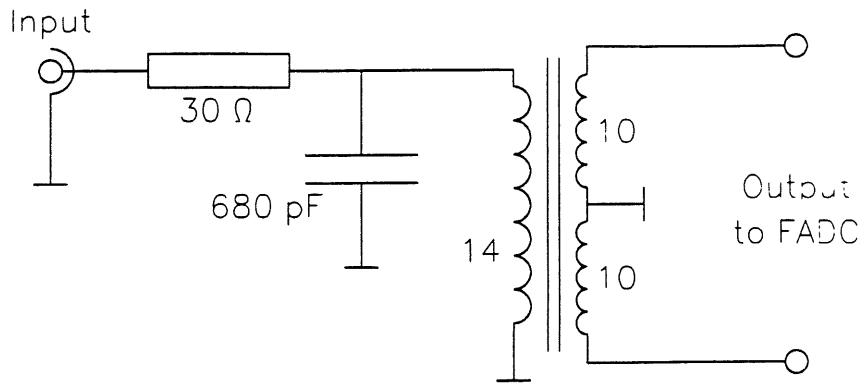

Figure 3.4: RC Filter circuit used with the DWC and trigger timing pulses.

the final trigger signal was read out using spare FADCs and used as a time reference during track reconstruction.

Since the same timing algorithms were used for the trigger signals as for genuine RWDC pulses, it was necessary to slow down the leading edge of the trigger pulses before they entered the FADCs using the simple RC filter shown in figure 3.4 [26]. This circuit has a rise time of $\simeq$ 27 ns resulting in the pulse leading edge being spread over 2 or 3 FADC bins, which is similar to that of a real RWDC pulse and ideal for accurate timing. The secondary coil, which is grounded at the center, causes a single input pulse to produce two output pulses of opposite sign to mimic the differential preamplifier output (section 2.3.3). 8 such circuits were implemented on a small circuit board which plugged directly into the back of the FADC crate.

Signals from two points in the trigger were input to two different FADC channels. Taking the average time improved the accuracy of the final drift time origin measurement by a factor $1/\sqrt{2}$. The spread in differences between the times of the two signals (figure 3.5) is equal to $\sqrt{2}$ times the error on each signal. The gaussian width of the time difference is 0.03 FADC bins (0.29 ns) indicating that the error on the final drift time origin measurement is $\pm$0.14 ns.

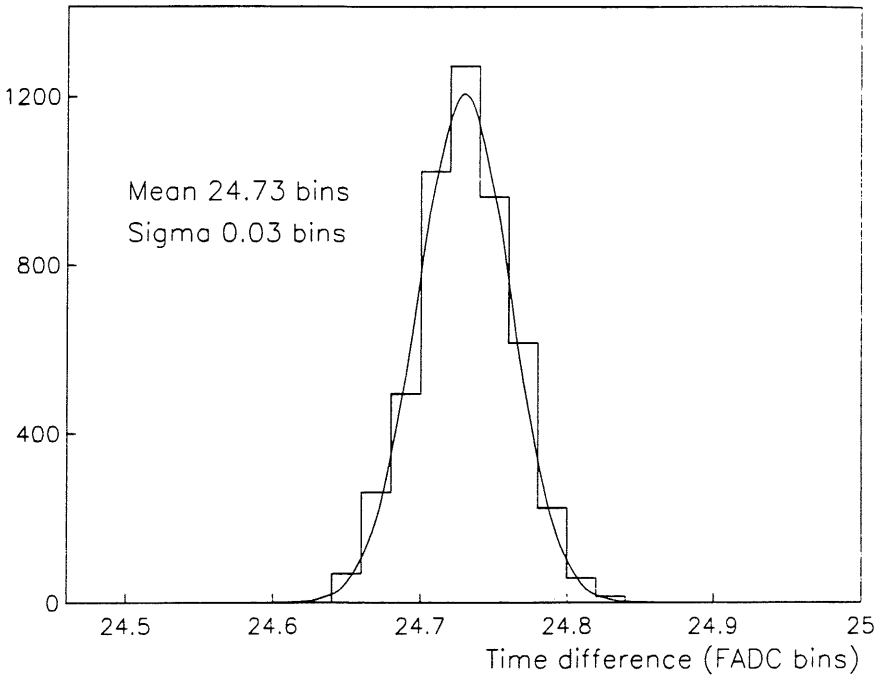

Figure 3.5: Time difference between trigger signals. (1 FADC time bin = 9.6 ns.)

3.3.2 Beam Position Measurement

3.3.2.1 The Delay Wire Chamber

The position of each particle in the beam was determined using the Delay Wire Chamber (DWC) mounted close to the end of the beam pipe. The DWC provides independent X, Y coordinates to a precision of 200 μm. A complete description is given in [27]. For each coordinate a plane of anode wires mounted perpendicular to the beam direction and sandwiched between two planes of cathode wires functions as for a normal MWPC. Charged particles passing through the chamber produce electron/ion pairs and the electrons drift towards the anodes. Close to the anode surface avalanche processes multiply the number of electrons and hence the signal on the anodes. Since the cathode wires are strung perpendicular to the anodes, the mirror current produced on the cathodes is spread over several wires. This would not be the case if the cathode wires were strung parallel to the anode wires. Of the 55 cathode wires on each side of the anodes, the central 51 are connected to a tapped delay line, the signals from both sides being used to increase the size of the signal. The measured time difference between the arrival of the signals at the opposite ends of the delay line is directly proportional to the posi-

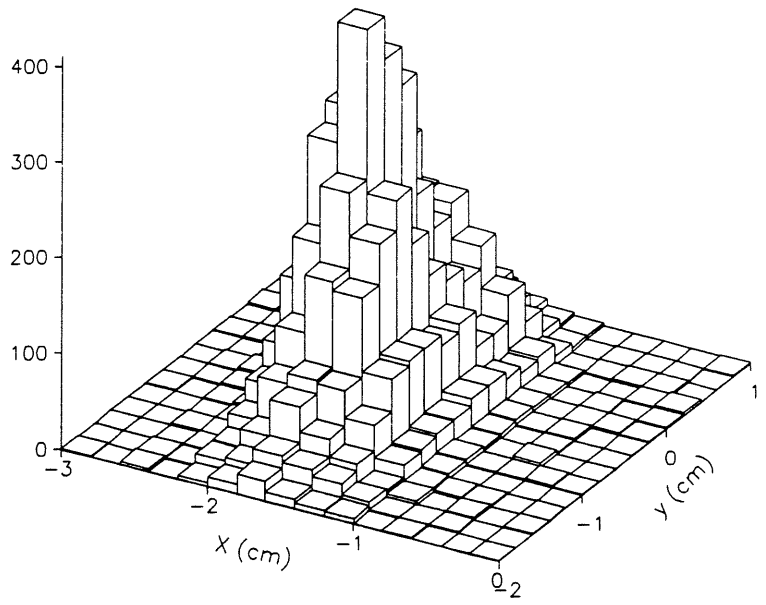

Figure 3.6: Typical beam coordinate distribution from the DWC.

tion of the incident particle. The spreading of the signal over several of the cathode wires results in the DWC accuracy being an order of magnitude smaller than the 2 mm cathode wire spacing.

Each coordinate from the DWC should normally be determined by measuring a single time difference with a Time to Digital Converter (TDC). TDCs were not available during the tests so an alternative approach was made using spare FADCs to measure the time differences between the ends of the delay lines. Since the discriminators at the outputs of the DWC preamplifiers were designed to be used with a TDC the pulses from the DWC were only a few ns wide – far too narrow to be read out by a FADC sampling only every 9.6 ns. The raw DWC signals were not available, so the discriminated signals were passed through a second set of discriminators [28] which were adjusted to give a 100 ns duration output pulse before being input to the FADCs via the same filter circuits as those used for the trigger timing signals (figure 3.4). Enough hardware was available for each signal to be read out using two separate FADCs, the signals being connected from the discriminator outputs to the filter card by a 10 ns and a 6 ns cable to give the same improvement and check on the timing accuracy as for the drift time origin determination.

The beam coordinates measured in the DWC for a typical run are shown in figure 3.6.

3.3.2.2 Traversing Support

The traversing support could be operated remotely from outside the beam area. It was fully interlocked to avoid the possibility of damage to the chamber or surrounding apparatus. Care was also taken to ensure that gas pipes and cables to or from the chamber could not get damaged during movement. The position of the support was measured using an optical readout system which was accurate to $\pm 10 \mu$m [29]. However, due to mechanical instabilities in the support structure and backlash, the position of the chamber was subject to an error of up to 200 μm.

3.3.2.3 Beam Dispersion Effects

The dispersion of the SPS beam is approximately 1 mrad [24]. With the DWC mounted 2.3 m upstream of the RWDC, the beam position at the RWDC would only have been accurate to ± 2.3 mm. A second DWC which would have enabled determination of the precise direction vector of each particle was not available. The beam dispersion was studied by comparing coordinates measured in the DWC with those reconstructed in the RWDC using *a priori* knowledge of the RWDC drift velocity. Making a correction for beam dispersion in this way affected the measured drift velocity (section 3.6) by $\sim$0.5 %. This in turn affects the measured dispersion by $\sim$0.5 % which was not large enough to then have an effect on the measured drift velocity when the drift velocity measurement was repeated.

Figure 3.7.a shows the beam dispersion which is given by

$$\text{Dispersion} = \frac{D_{\text{cham}} - D_{\text{beam}}}{D_{DWC}} \tag{3.1}$$

where D_{cham} and D_{beam} are the drift distance in the RWDC and the expected drift distance measured by the DWC. D_{DWC} is the distance between the RWDC and the DWC. In figure 3.7.b the mean values of the beam dispersion in figure 3.7.a have been plotted at different beam positions in the DWC showing a clear correlation between dispersion

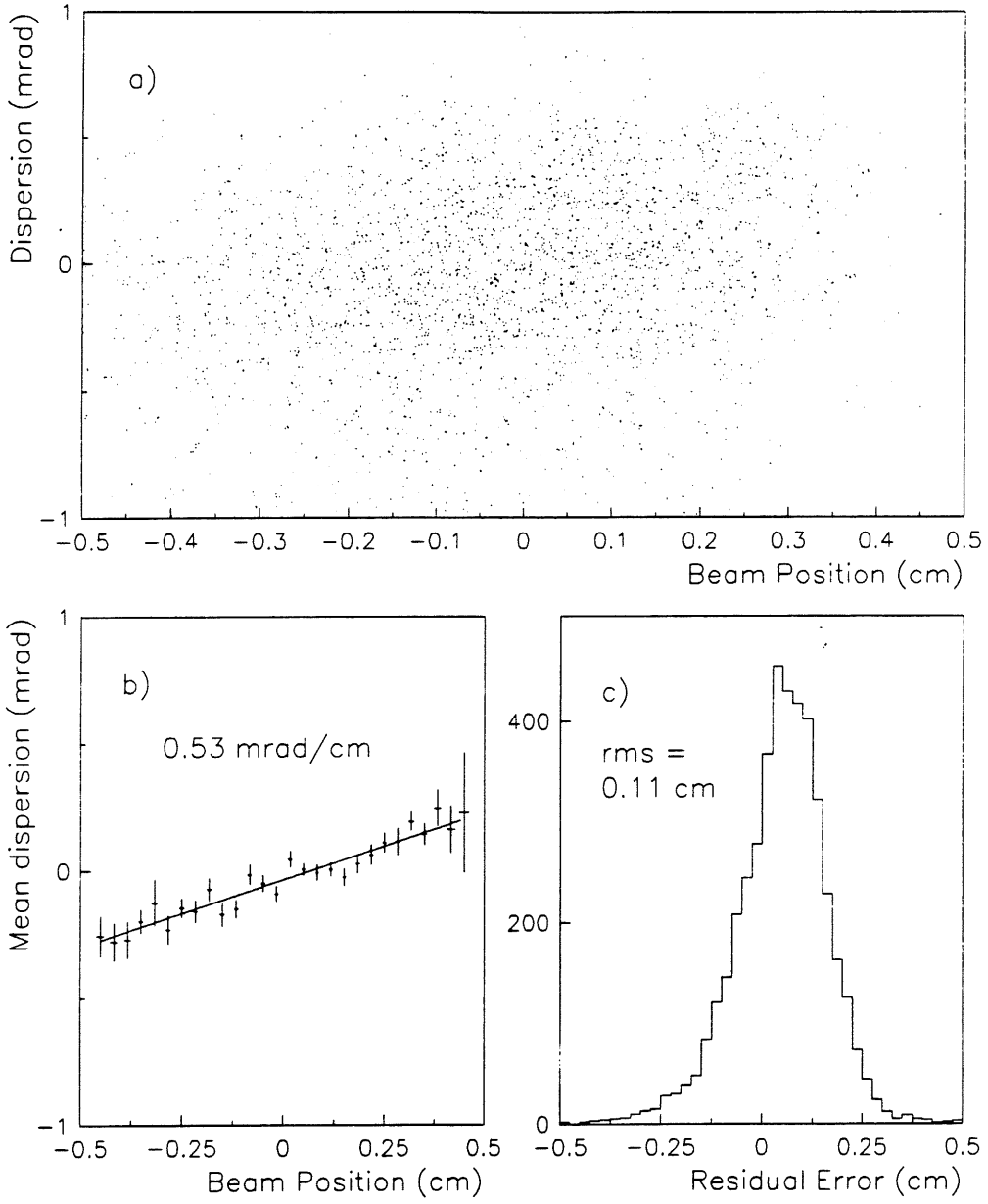

Figure 3.7: Beam dispersion: a) Scatter plot of measured dispersion against DWC coordinate, b) Mean dispersion plotted against DWC coordinate, c) Residual difference between predicted and measured beam coordinates when dispersion has been taken into account.

and the beam position at the DWC of 0.53 mrad/cm. This measured variation with beam position may be taken into account when projecting tracks from the DWC into the RWDC. When dispersion has been taken into account in this way a comparison between the predicted and the measured drift coordinates (figure 3.7.c) shows that the predicted beam position is accurate to ± 0.11 cm.

3.3.2.4 Absolute Beam Coordinate Determination

No attempt was made during the tests to make precise measurements of the absolute positions of the traversing support and the DWC. The relative positions were measured to within ± 0.5 cm with a meter rule and the precise relative positions calculated by comparing the mean difference between the predicted and measured beam coordinates during data analysis. To do this only the drift distance was used since it is two orders of magnitude more accurate than the charge division coordinate. Data in wedges with wires strung vertical and wedges with wires strung in a horizontal plane were used to obtain precise X and Y positions for the test beam components.

Combining the coordinates of the traversing support and the coordinates reconstructed from the DWC gave the position of *individual* particles passing through the chamber to a much greater accuracy than if the beam position had been defined by scintillators alone: namely 1×2 cm, which was the area of the smallest scintillator used in the trigger.

3.4 Drift Timing and Pulse Integration

The first step in the analysis of data from the RWDC was the determination of drift times and pulse integrals. In H1 this is done on-line which gives a 75 % reduction in the amount of data which has to be written to disk. For the tests, all of the raw data were written to disk and the analysis done off-line, thus enabling further developments of this vital step in the analysis.

The determination of drift times follows the "First Electron Method" developed from the analysis of data from early prototypes [25]. The principal refinement (also used in H1) is that the drift times are calculated separately from the signals at each end

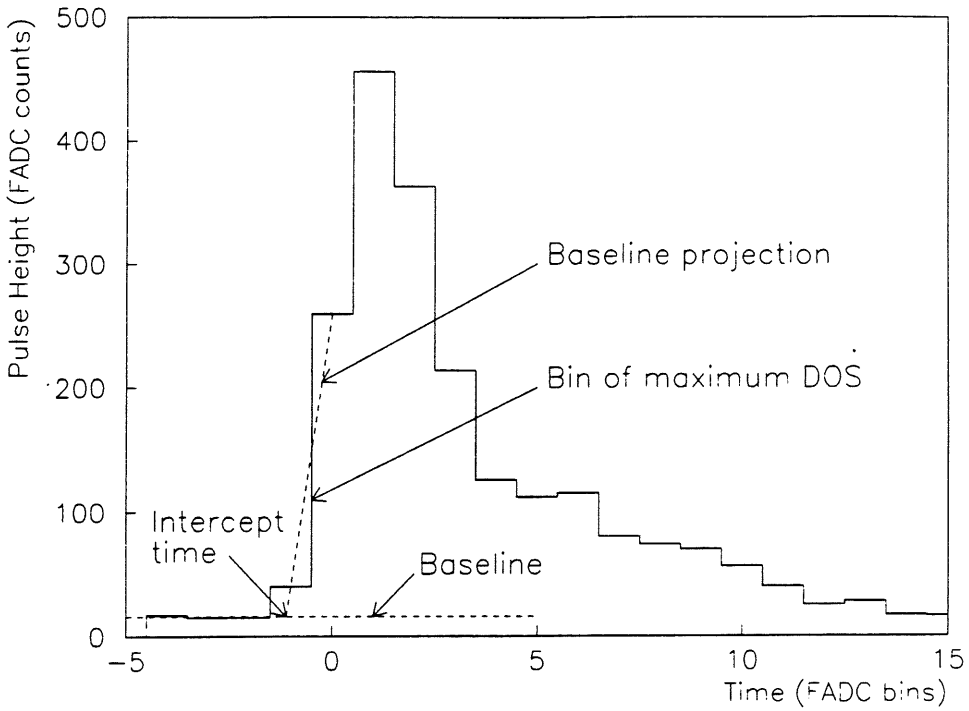

Figure 3.8: A typical RWDC pulse showing a construction of the "First Electron" timing method.

of the wire and a weighted average using the pulse integrals of the two times is taken. This is important since cables from the FTD were cut for mechanical convenience and are not necessarily the same length from the two ends of each wire. It also permits a correction to the final drift time to allow for the propagation delays inside the chamber based on the radial coordinate of each hit. A typical pulse from one end of a wire with a construction of the timing method is shown in figure 3.8. Figure 3.9 shows the charge integration interval. Drift time and charge integral determination is done in the following stages.

1. Raw data is relinearized using a lookup table which is the inverse of the non-linear FADC response described in section 2.3.4.

2. The sum of the relinearized data from the two ends of the wire is scanned for pulses using the product of the pulse height and the difference of samples – the Weighted Difference Of Samples (WDOS).

3. The baseline for each end is determined by taking the average of the bin contents

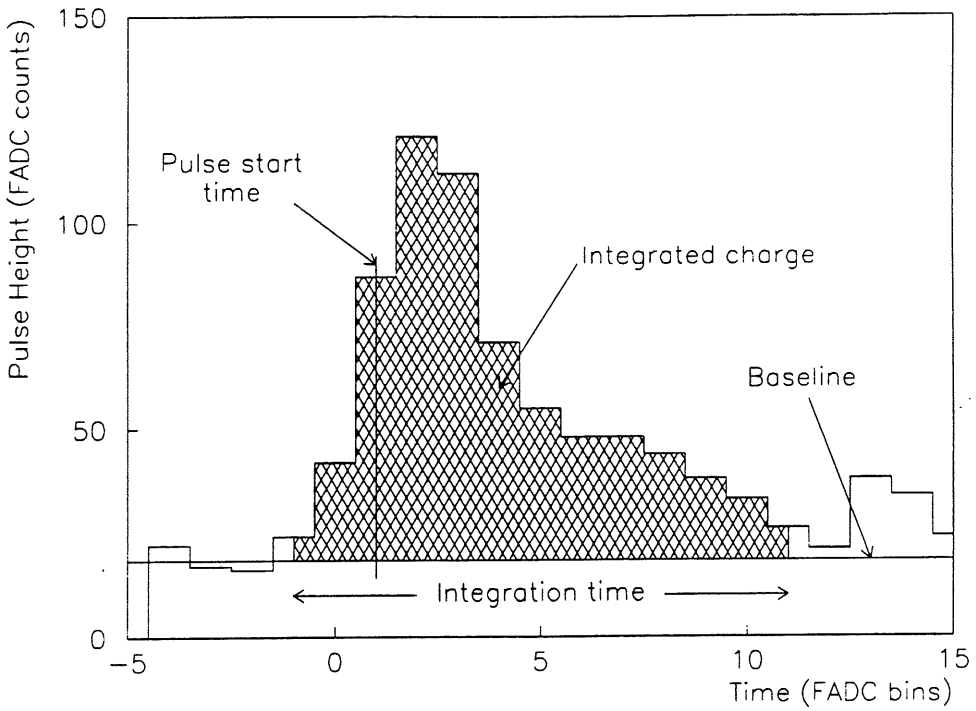

Figure 3.9: The charge integration interval on a typical RWDC pulse.

preceding the start of each pulse.

4. The bin of maximum Difference Of Samples (DOS) on the leading edge is determined separately for the pulses from each end of the wire.

5. The pulse height on either side of the maximum DOS is projected back to the baseline.

6. A transformation, calculated from the analysis of previous data, is applied to the intercept time so that the distribution of all drift times is a top hat function between $\pm\frac{1}{2}$ FADC bin of the bin of maximum DOS.

7. Charge integration of the pulse at each end of the wire is carried out over an integer number of FADC bins starting from a point 2 bins in front of the (generally non-integer) start time for that pulse.

8. The final drift time is taken as the weighted mean of the times measured at the two ends of the wire using the pulse integrals.

3.5 Test Pulse Calibration and Corrections

The calculated times described above take no account of the propagation delays of the pulses along the wires inside the tank or the cables to the FADC crates. Similarly, before the integrated charges may be used for radial coordinate determination and particle identification, the gains of individual amplifier channels must be taken into account. Appendix A describes how test pulse data were analyzed to calculate the different propagation delays, amplifier gains and the ratio of the anode resistance to the preamplifier input resistances for use in charge division calculations. The calibration constants are:

t_0: Mean propagation delay along the two signal cables to the two FADCs from the center of the chamber.

D_D: Difference in propagation delays along the two signal cables to the FADCs.

D_T: Propagation time along the anode wire.

G_{rel}: Relative electronic gains and cable attenuation factors from the two ends of an anode.

G_{prod}: Product of the amplifier gains and cable attenuations at the two ends.

$\frac{L_{eff}}{L}$: The ratio of the total resistance between the two preamplifier inputs (i.e. including the preamplifier input resistances) to the resistance of the paired anode wires only.

Making the approximation in equation A.27 that $\gamma = \alpha$ (γ is the fractional distance from the center of the hub connector to the end of the wire and α is defined in equation 3.9 on page 75) and adding a global time offset common to all wires Gt_0, the correction applied to the raw drift times becomes

$$t_{corr} = t_D - \left\{ t_0 + Gt_0 + \frac{1}{2}\alpha(D_D - \alpha D_T) \right\} \quad . \tag{3.2}$$

The determination of the term Gt_0 is discussed in section 4.2.2.

Apart from the term D_D, the values obtained for the calibration constants from test pulse data were fully consistent with the expected values based on the chamber

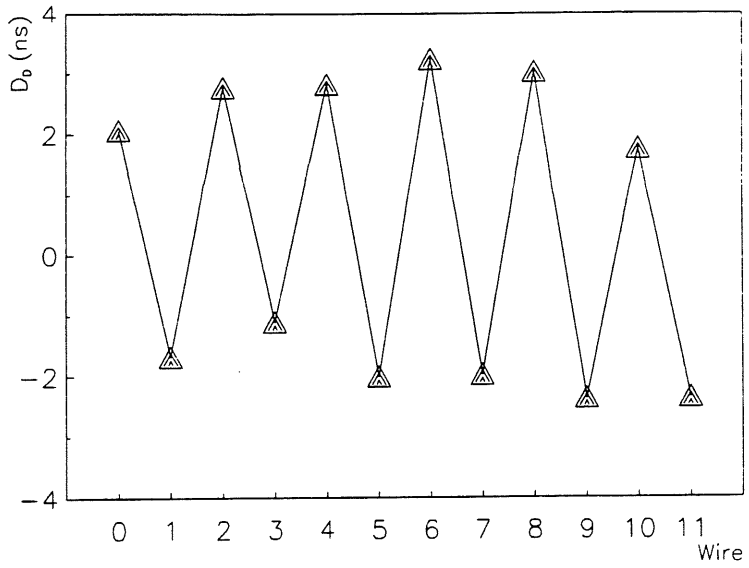

Figure 3.10: Variation of the calibration constant D_D across a typical wedge.

geometry and genuine differences in cable lengths. The D_D term does however warrant further discussion and is plotted for a typical wedge in figure 3.10. It can be seen that the magnitude of D_D fluctuates regularly from wire to wire across the wedge by $\sim \pm 2$ ns. In terms of cable lengths this would amount to approximately 60 cm. Each cable from the RWDC to the FADC crate carries signals from one end of 8 anode wires, i.e. for the front 8 wires, one cable carries the signals of all of the *R*ight end signals and a second cable carries the *L*eft end signals. The back four wires are connected in much the same way except that two cables take the signals from the back four wires of two adjacent wires. This pattern of cabling (and the variation in D_D) is repeated throughout the chamber. The signal cables used for the CERN tests came from a different manufacturer than those used with the RWDCs installed in the H1 experiment, and yet the variations in D_D are similar for both installations. It is most unlikely that irregularities in the internal structure of the cables would be common to both manufacturers, particularly since the cables used in the tests and those used in H1 are not even of the same length. The variation must therefore come either from the chambers or from the FADC system. Great care was taken to ensure even manufacture of the wires connecting the RWDC crimps to the preamplifier feedthroughs, so it must be assumed that the variation occurs at the FADCs. Again, it is known that the FADC

Variable	Mean value	rms variation	Effect in reconstruction	
			Along a wire	Between wires
t_0	6.0 ns	1.1 ns	0	1.1 ns
D_D	0.11 ns	2.1 ns	$\sim$ 1.0 ns	$\sim$ 1.4 ns
D_T	13.9 ns	1.6 ns	3.7 ns	0.4 ns
G_{rel}	0.993	0.038		
G_{prod}	1.0	0.08		
$\frac{Leff}{L}$	1.37	0.006		

Table 3.1: The magnitude and rms variation of test pulse calibration constants. The numbers in columns 4 and 5 represent the effect that the calibration constants directly associated with drift timing have on the drift time.

crate has been designed to minimize delay differences between channels so it seems likely that the variation is due to the FADCs failing to start at the same time.

Table 3.1 shows the mean and rms values of each of the above calibration constants. Also in the table are the variations in the corrections made to drift times along the length of a single anode wire (i.e. from the hub to the outer radius) and the typical variation of the correction between adjacent anode wires.

3.6 Drift Velocity Determination

The drift velocity in each gas mixture was determined by making a direct comparison between the measured drift times and the known beam position from the DWC and the traversing support (section 3.3.2) for each wire in a wedge or wedges of the RWDC as shown in figure 3.11 for wire 1 of wedge 34 in Ar:C_2H_6 50:50 gas mixture. Only data accepted by the RWDC pattern recognition as part of a track were used so as to remove random stray points. For clarity, points associated with a track on the negative side of the wire plane are assigned a negative time. The small number of points along the diagonal axis opposite that of the bulk of the data is due to tracks resolved on the wrong

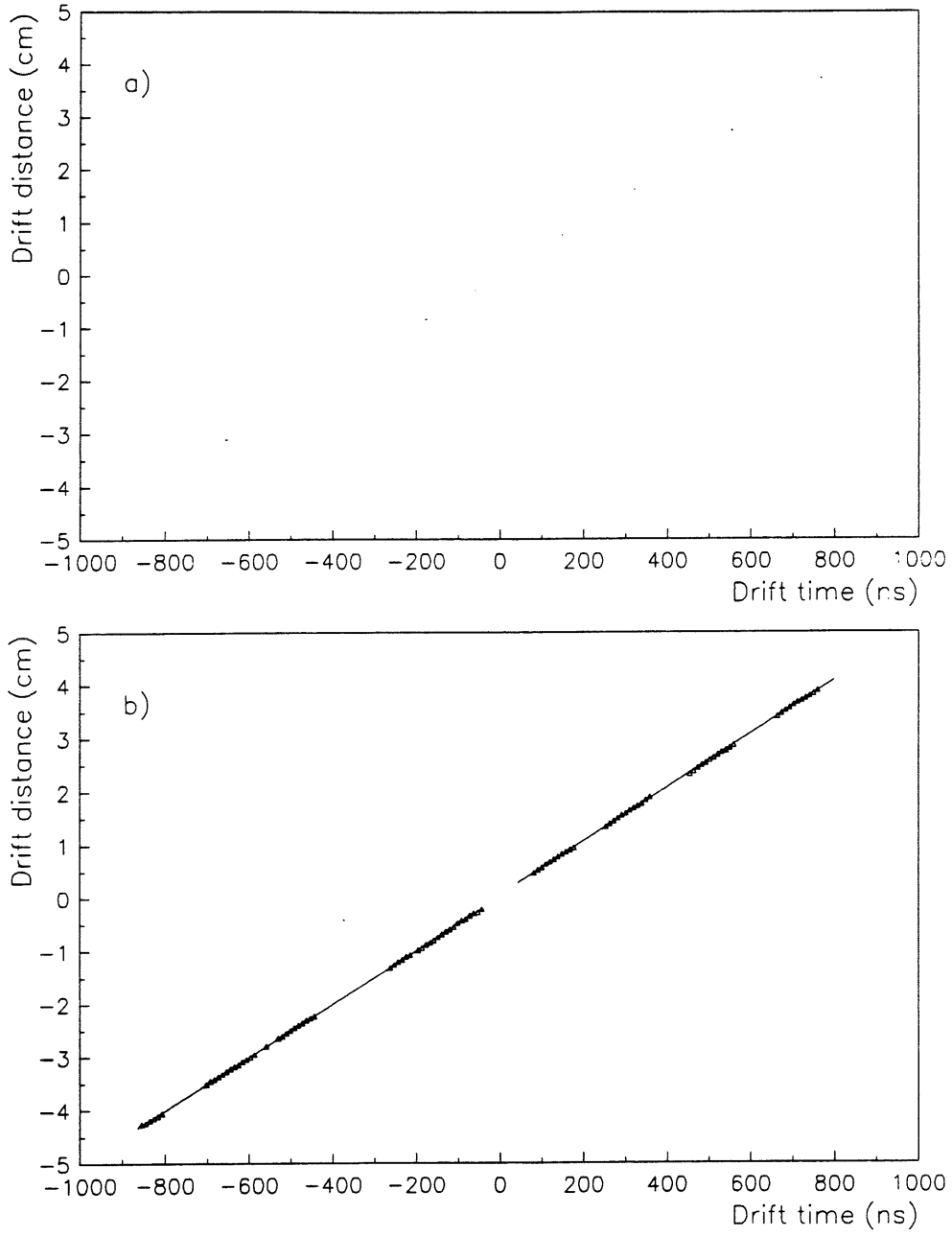

Figure 3.11: Distance – Time relationship for wire 1, wedge 34 in Ar:C_2H_6 50:50 gas mixture. a) Scatter plot of the projected drift distance from the DWC and the traversing support against the RWDC drift time, b) Mean drift distance of (a) plotted against RWDC drift time.

side of the wire plane. Figure 3.11.b shows the mean values of gaussian fits to vertical slices of figure 3.11.a. Only slices with a significant (> 200) number of points were included to restrict data used in later analysis to the center of the beam spot, which avoids the outer extremities of the beam where dispersion effects are less predictable than at the center. The mean value of the gaussian width of the slices passing the above selection criteria was 0.11 cm, which is fully consistent with the random error in the beam position discussed in section 3.3.2.3. Since the beam from the SPS was approximately 1 cm in diameter, it was necessary to take data with the beam centered at several different points across the wedge which accounts for the somewhat "blotchy" nature of the plots.

Drift velocity was determined by a simple straight line fit to the points in figure 3.11.b. Each half of the wedge is fitted separately and the region close (< 4 mm) to the wire plane ignored to avoid any non-linearities in this region. A further advantage of this method is that no errors are introduced due to an error in the global t_0 which causes the intercept with the vertical axis of the two halves of the plot to be different. The principal errors in this measurement come from errors in the position of the traversing support. This effect is visible in figure 3.12 where the difference between the individual points and the fitted lines in figure 3.11.b are plotted against drift distance. The beam spot centered at a drift distance of 2.6 cm is clearly out of line with the rest by $\sim 150\,\mu$m.

By scanning across two complete wedges of a RWDC four individual measurements of drift velocity were made on each of the 12 wires in Ar:C_2H_6 50:50 gas mixture. Figure 3.13 shows the mean value and the error on the mean which is $\frac{1}{\sqrt{4}}$ of the rms variation of four measurements. The drift velocity displays no significant deviation from a constant value over the central 10 wires but is lower on the front and the back wires. The main source of error is mechanical instability of $\sim 200\,\mu$m in the traversing support leading to an error of ~ 0.5 % in each drift velocity measurement over a drift distance of 4 cm.

Data from Xenon based gas mixtures were analyzed in a similar way except that only data from a single wedge were available giving only two measurements of drift

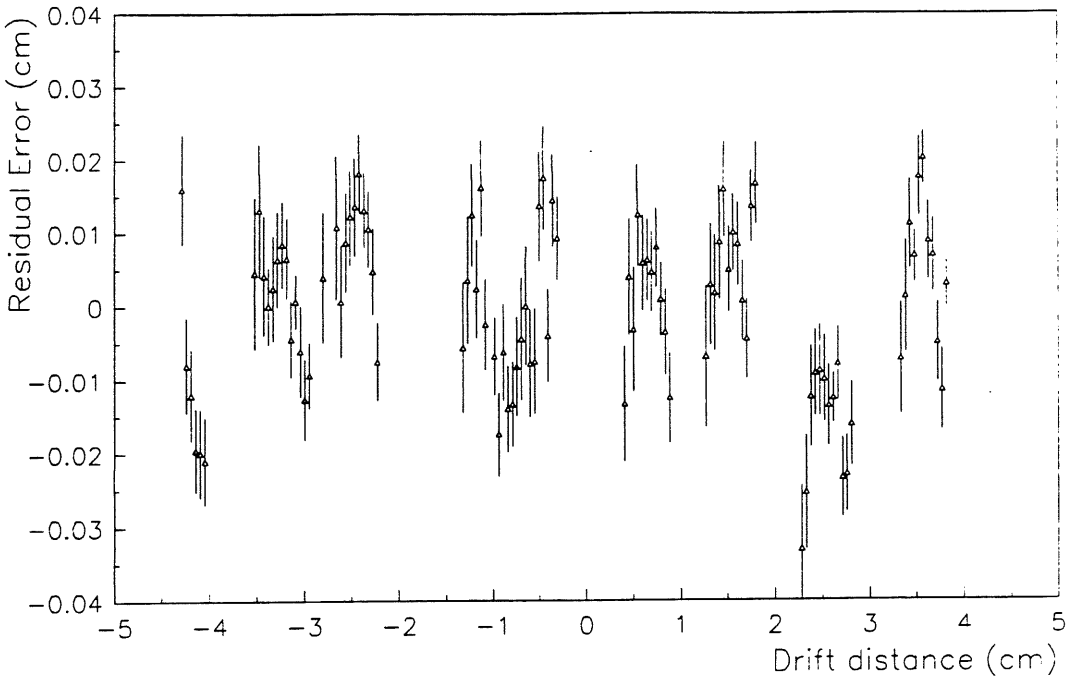

Figure 3.12: Difference between the beam coordinates from the DWC and the mean reconstructed coordinates using the fitted drift velocity for wire 1 of wedge 34.

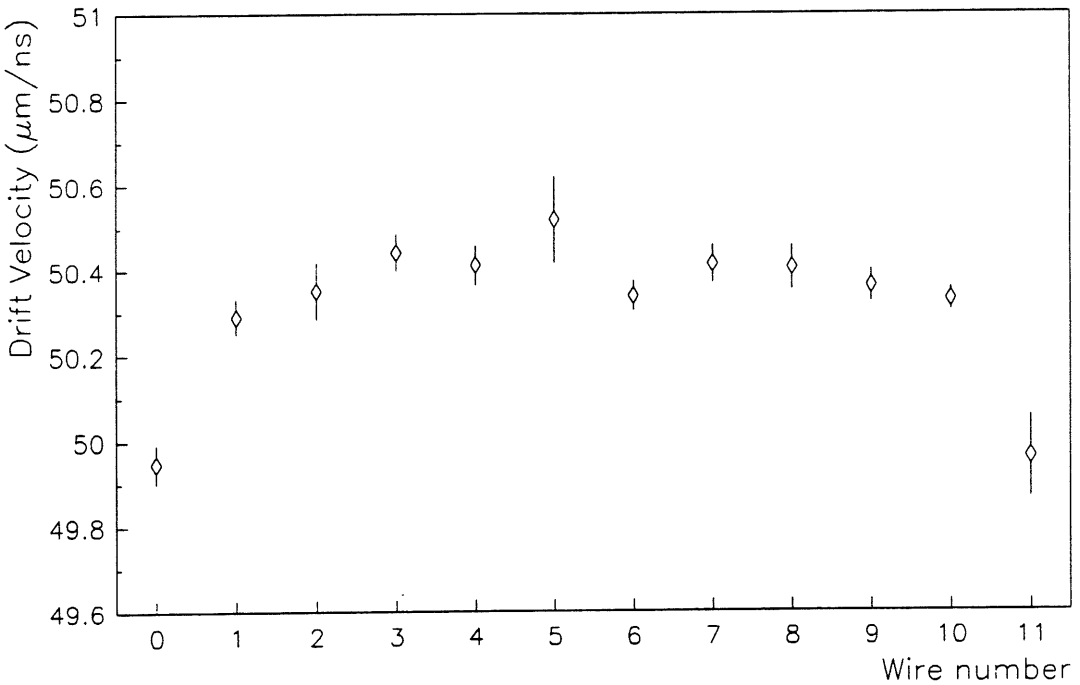

Figure 3.13: Drift velocity at ambient temperature and pressure on the 12 wires of a RWDC in Ar:C_2H_6 50:50 gas mixture. Four independent measurements on each wire are combined to give the displayed values and errors.

Gas		Electric Field kV/cm		Drift Velocity μm/ns		
		Drift	Anode	Front	Central	Back
$Ar:C_2H_6$	50:50	1.2	170	50.0±0.05	50.4±0.06	50.0±0.10
$Xe:He:C_2H_6$	30:40:30	1.2	157	32.9±0.88	34.2±0.31	34.0±0.34
	20:40:40	1.2	160	35.8±0.40	36.9±0.15	36.2±0.04
	15:45:40	1.2	160	33.3±0.01	35.4±0.59	35.0±0.37

Table 3.2: Measured drift velocity in different gas mixtures at ambient temperature and pressure. Values for the front wire, the central 10 wires, and the back wire are given separately for each mixture.

velocity for each of the twelve wires. As for the Argon based gas, the Xenon mixtures show a constant drift velocity for the central 10 wires and a slightly lower velocity on the front and back wires. The results for different gas mixtures are summarized in table 3.2.

In all gas mixtures the drift velocity on the front and back wires is lower than on the central 10 wires due to slight differences in the electric field close to the boundaries of the radial wedge. Drift velocities on the front wire are low by up to 6 % and on the back wire by up to 0.8 %. Since the voltages on the front and back field forming strips and hence the field close to the front and back wires can be varied independently of the field in the center of the chamber it may be possible to improve the performance of the front and back wires. The results from $Ar:C_2H_6$ 50:50 gas mixture, where the drop in drift velocity is the same on both the front and the back wires also indicate that the novel design of the RWDC front field formers is not adversely affecting the performance of the RWDC as a tracking device.

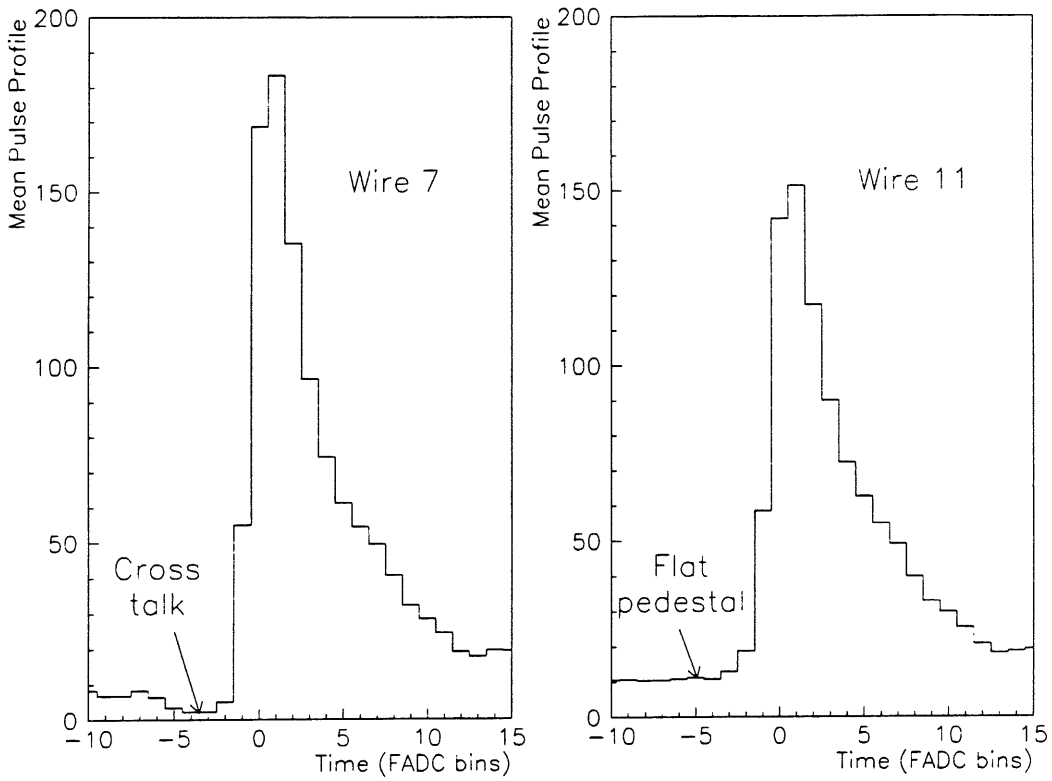

Figure 3.14: Mean profile of pulses on wires 7 and 11 for tracks angled at 10° to the wire plane. The time origin of each plot is the bin of maximum WDOS.

3.7 Cross Talk

It was reported in [25] that cross talk existed between the wires of prototype RWDCs at the level of −7 %. That is, a chamber pulse induces a small inverted image of itself on the adjacent wires. For tracks parallel to the wire plane, the ±287 μm wire stagger causes a difference in arrival time between pulses on adjacent wires of 12 ns in a typical gas with a drift velocity of 50 μm/ns. Therefore the maxima of the pulses which arrive first coincide with the center of the leading edges of the later pulses. Since the drift time is measured on the leading edge of a pulse, the measured drift time of the early pulse is not affected, whereas the leading edges of the later pulses are made smaller due to the cross talk, resulting in the measured drift times being artificially large.

Due to electrical noise, cross talk is not readily observed in single chamber pulses. It does, however, become clear when looking at the mean shape of a large number of pulses from angled tracks where the pulses on adjacent wires are separated by several

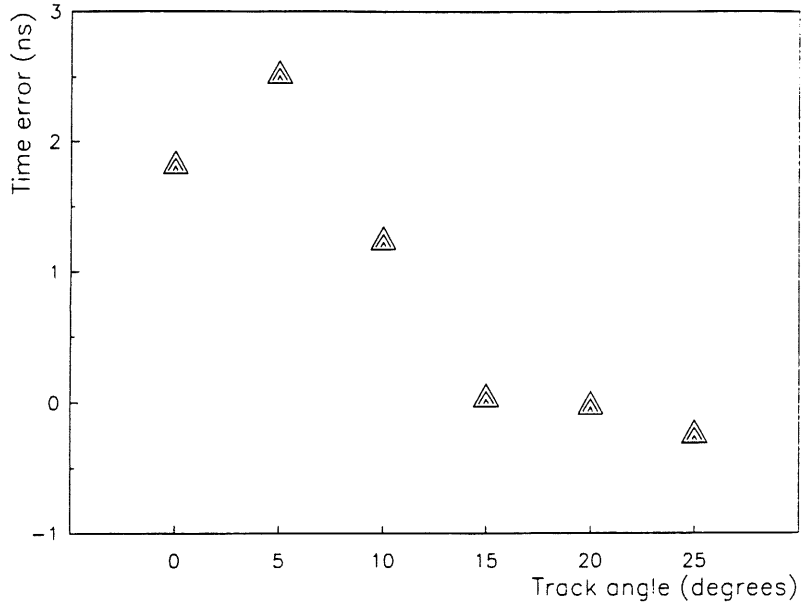

Figure 3.15: Relative timing error between odd and even wires.

FADC bins. Figure 3.14 shows the mean pulse shapes on wire 7 and wire 11 of 10000 tracks angled at 10° to the wire plane. The tracks are all on the same side of, and are approaching, the wire plane. The leading edges of pulses on wire 11 (the back wire) are, therefore, not affected by cross talk since they are always the first to arrive at the anodes. Due to the combination of track angle and wire stagger, a pulse on wire 8 will always arrive 46 ns (4.8 FADC bins) before pulses on wire 7, resulting in a marked dip in the pedestal region preceding pulses on wire 7.

The effect of cross talk on measured drift times can be studied using a 3 parameter fit to a set of drift times:

$$t_i = az_i + b + s_i \frac{1}{V_D^F} \tag{3.3}$$

where t_i, z_i and s_i are the drift time, z coordinate and stagger of each of the twelve wires. a, b and V_D^F are the tangent of the fitted track angle, the drift distance at the front window and the drift velocity. The time difference between the odd and even wires is expressed in the term $s_i \frac{1}{V_D^F}$, the actual time difference between pulses on odd and even wires being $2s\frac{1}{V_D^F}$ where s is the nominal 287 μm wire stagger. Figure 3.15 shows the relative timing error between odd and even wires given by

$$2s\left(\frac{1}{V_D^F} - \frac{1}{V_D}\right) \tag{3.4}$$

where V_D is the known drift velocity from section 3.6. As expected, at large angles the

pulses on different wires do not coincide sufficiently for cross talk to have a significant effect and there is a negligible timing error. At smaller angles however the error varies with angle, never falling to zero, since due to the wire stagger, it is impossible for signals on all wires to perfectly coincide.

3.7.1 Overview of Cross Talk Compensation Techniques

The H1 preamplifiers do not contain cross talk compensation circuitry such as that used for the OPAL jet chamber [30]. There are therefore two possible methods of compensation left available. The first is to use the flash-digitized raw data to make a direct compensation by adding a fraction of each pulse to the signal on neighbouring wires. The second is to study carefully the effect cross talk has on drift times and drift distances as a function of the relative times of pulses on adjacent wires and develop an algorithm to make a correction to the measured drift times or distances at a later stage of track reconstruction. The first method has the advantage that it has obvious physical meaning whereas the second method relies solely on a 'hand made' parameterization which may not describe fully all of the processes taking place inside the chamber. However, the large differences in the relative FADC start times described in section 3.5 make a direct compensation impractical. Furthermore, the design of the H1 data acquisition system is such that it is not possible to have data from several different FADC channels available simultaneously in the front end processor during QT analysis [21]. In order therefore to do a direct compensation, all of the raw data would have to be read out from the experiment so that the analysis could run off-line. This would result in a four-fold increase in the quantity of RWDC data written to disk which would be unacceptable both in terms of read-out time and storage space.

3.7.2 Parametric Cross Talk Compensation

To correct retrospectively for the effects of cross talk it is necessary to find some function F which can be used to calculate a new drift time t_{new} from the drift time t_{corr} (see equation 3.2) using

$$t_{new} = F\left(t_{corr}, \delta t, Q_W, Q_{CT}\right) \tag{3.5}$$

where δt is the time difference between pulses on adjacent wires, Q_W is the charge on the wire being affected by cross talk and Q_{CT} is the charge on the wire causing the cross talk.

Since large pulses will have a more significant effect on small pulses than vice versa, it seems sensible to include the term $\frac{Q_{CT}}{Q_W}$ in the function $F(t_{corr}, \delta t, Q_W, Q_{CT})$. Equation 3.5 could therefore be of the form

$$t_{new} = t_{corr} - \frac{Q_{CT}}{Q_W} G(\delta t) \quad . \tag{3.6}$$

Before proceeding, certain properties of $G(\delta t)$ are immediately obvious:

- When two pulses on adjacent wires coincide precisely cross talk will not change the shape of each pulse. Therefore the measured time of each pulse will remain the same and $G(\delta t = 0) = 0$.
- Since cross talk makes drift times artificially large, $G(\delta t)$ is always positive.
- When the track angle is steep enough so that two pulses do not coincide at all, cross talk can have no effect so $G(\delta t \Rightarrow \infty) = 0$.

The magnitude of $G(\delta t)$ must therefore rise from zero at $\delta t = 0$ to some maximum and then fall again to zero at $\delta t = t_{max}$, t_{max} being the maximum time difference at which cross talk has any significant effect. Intuitively one expects the function to rise rapidly to a maximum and then fall more slowly with δt as the maximum of the pulse causing the cross talk moves across the leading edge of the pulse being affected, i.e. the function $G(\delta t)$ should be a similar shape to the RWDC pulse profile.

For tracks parallel to the wire plane, pulses from half of the wires should arrive simultaneously and the pulses from the other 6 wires 1.2 ns later (in Ar:C_2H_6 50:50 gas) due to the wire stagger. The early pulses are unaffected, whereas the late ones are subjected to cross talk from *two* adjacent wires. For angled tracks the situation is more complicated since, in general, for tracks at an angle greater than 3.4° every pulse (except that on the front or the back wire) will have a pulse arriving before it on one side and a pulse arriving later on the other side (figure 3.16). Each pulse will therefore

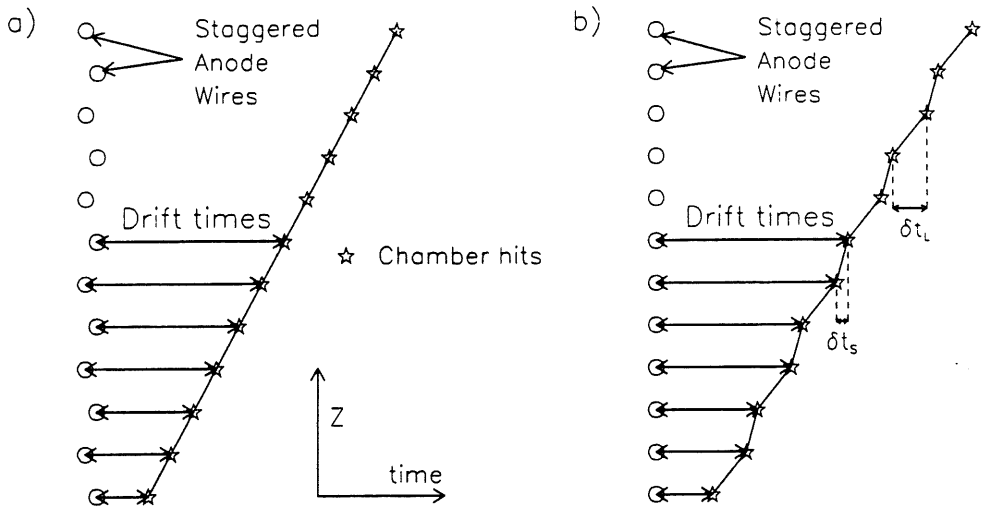

Figure 3.16: Drift time differences between adjacent wires for angled tracks. The wire stagger from (a) has been transferred to the drift times in (b) to emphasize the difference between δt_S and δt_L.

be affected by cross talk from a single pulse and pulses on odd and even numbered wires will be affected differently due to the different time intervals δt_S and δt_L.

Electrons in a RWDC drift towards the wire plane in a uniform electric field. Close to the wire plane (< 6 mm) the field increases in order to create the necessary avalanche multiplication of the signal. The fitted drift velocity V_D^F in equation 3.3 is measured from the time difference it takes electrons to traverse the extra distance between the two wire planes *in the region of high electric field.* In section 3.6 it has already been shown that the drift velocity is sensitive to changes in the field configuration. From figure 4.1 it is seen that the drift velocity in Ar:C_2H_6 50:50 gas increases to a maximum at a field of about 1 kV/cm and then falls slowly as the field is further increased. During the tests at CERN the drift field was 1.2 kV/cm in the uniform region >0.6 cm from the wire plane so any increase in the field close to the wire plane would cause a drop in drift velocity. Therefore, it is not possible to say exactly how much of the timing error in figure 3.15 is due to the effects of cross talk and how much is due to small differences in drift velocity close to the wire plane.

Determination of $G(\delta t)$ is further complicated by the two different values of δt affecting data from angled tracks. If it were assumed that the drift velocity close to the

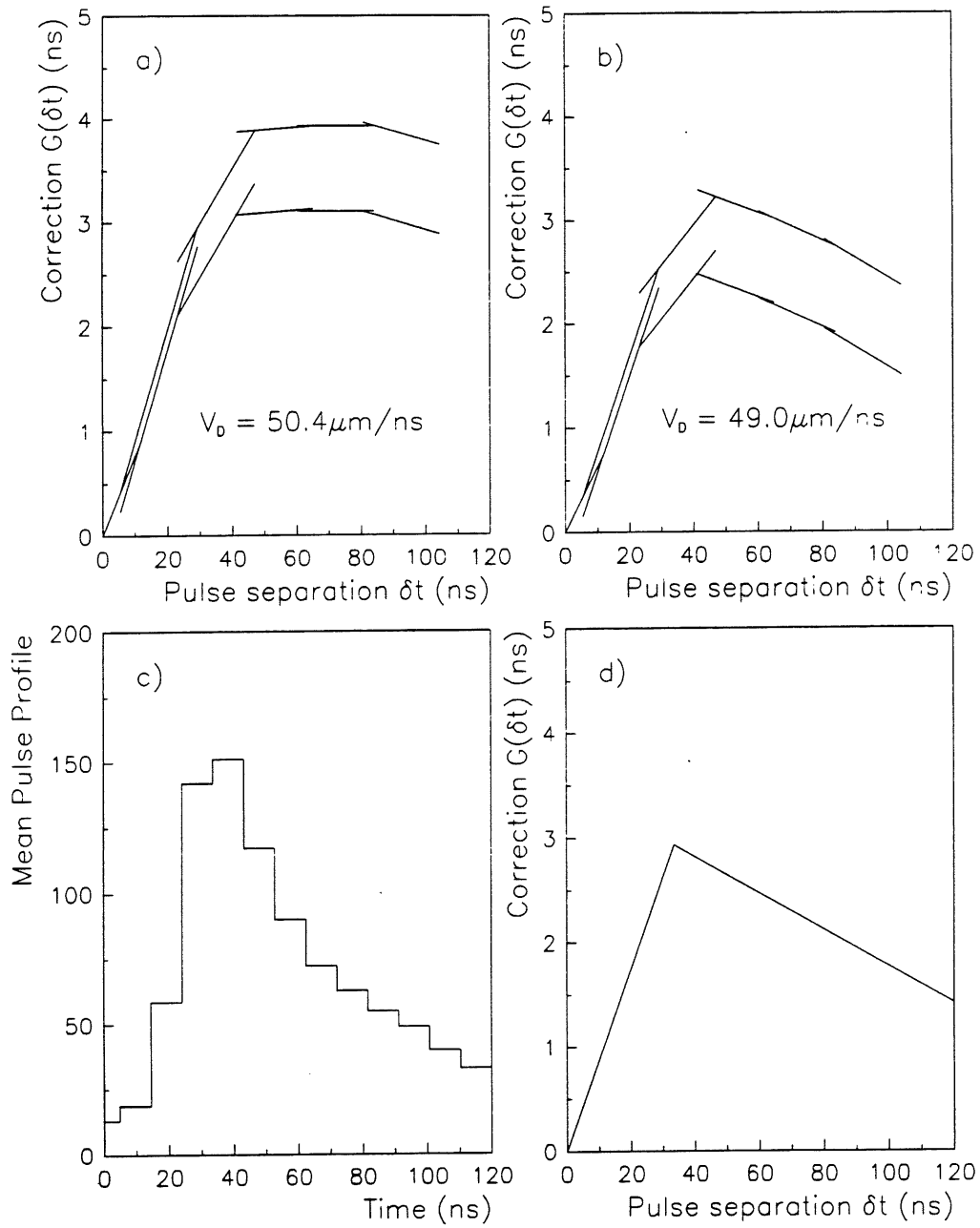

Figure 3.17: Parametric cross talk compensation. a) Measured correction with an assumed drift velocity of 50.4 μm/ns, b) as (a) but with an assumed drift velocity of 49.0 μm/ns, c) typical mean pulse profile (the time origin is at the start of the pulse), d) the parametric cross talk correction used during analysis of test data.

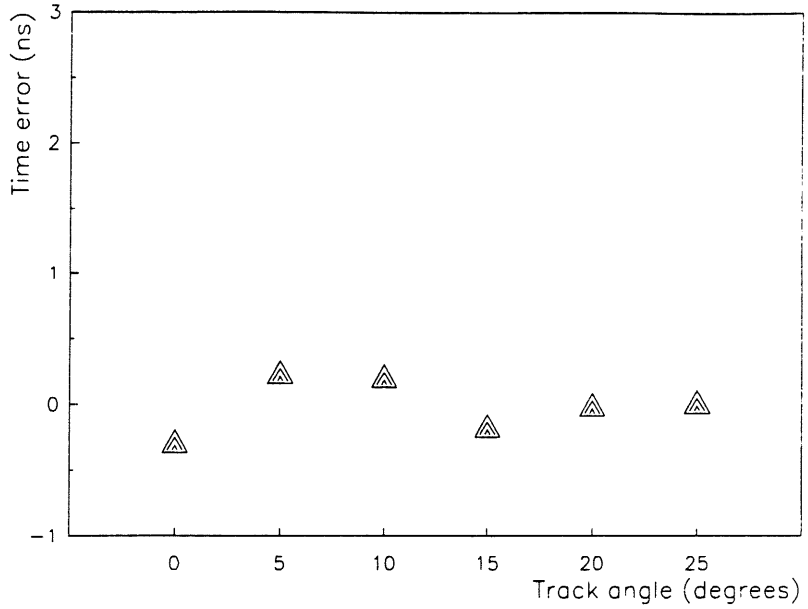

Figure 3.18: Relative timing error between odd and even wires after parametric cross talk compensation. (Compare with figure 3.15).

wires *is* 50.4 μm/ns and that the time difference in figure 3.15 *is* due entirely to cross talk, then for 0° tracks $G(\delta t = 11.9\text{ ns}) = 0.92$ ns. (The total correction at δt=11.9ns is 1.84 ns, but since all but the end wire are affected twice, the correction from each wire is only half that). At 5° however, it is only known that the difference in the correction between the two times δt_S and δt_L (i.e. $G(\delta t = 29.3\,\text{ns}) - G(\delta t = 5.45\,\text{ns})$) is 2.54 ns. It is necessary therefore to obtain the value of $G(\delta t = 5.45$ ns) from interpolation between the previous values of $G(\delta t)$ at $\delta t = 0$ and $\delta t = 11.9$ ns.

Such an interpolation is shown in figure 3.17.a where successive line segments are from data taken at track angles of 0°, 5°, 10°, 15°, 20°, and 25° respectively. Two lines are drawn to represent the maximum and minimum realistic interpolations between successive segments. Figure 3.17.b shows the results of a similar analysis with the relative time differences between odd and even wires based on a mean drift velocity in the region close to the wire plane of 49 μm/ns. Figure 3.17.c shows the mean pulse profile of wire 11 in figure 3.14 with the time origin shifted to the start of the pulse to demonstrate a similarity in shape between the mean pulse profile and the correction $G(\delta t)$.

It is clear that different interpretations of the best way to fit a function $G(\delta t)$ to the available data may produce large fluctuations in the end result. However, using the

function in figure 3.17.d to make a correction to drift times described in equation 3.6. it can be seen from figure 3.18 that there is a marked improvement in the relative drift times between odd and even wires compared to that in figure 3.15. In order to improve the quality of the data used to find $G(\delta t)$, data are needed at angles between the 5° intervals used here. Furthermore, the nature of the correction will probably differ for different gas mixtures and different chamber operating conditions which will affect the field close to the wire plane. A more thorough investigation may only be done using data from the H1 detector where tracks at all angles are present.

3.8 Radial Coordinate Determination

In the H1 experiment the radial coordinate (r) of hits in the RWDCs is determined by charge division. It is also possible to exploit the radial geometry of a RWDC to obtain a radial coordinate for a track crossing the cathode plane between two wedges since the sum of the drift times on each side of the cathode plane is related to r. This is not a realistic method of radial coordinate determination in the current RWDCs since, by design, only a small number of tracks will actually cross a cathode. It could however be ensured that tracks did cross a cathode plane by tilting the radial wedges relative to the z axis. To study the feasibility of this technique the RWDC was rotated in front of the beam forcing tracks to cross a cathode.

3.8.1 Charge Division

It was described in section 2.2 how a pair of anode wires in 2 wedges separated in ϕ by 105° are connected at the hub. A schematic diagram of the connection of two anode wires at the hub and the input resistors of the preamplifiers is shown in figure 3.19. Because of this connection charge division not only determines r but is also used to determine which RWDC wedge the track has passed through. Connecting wedges in this way makes charge division in the RWDC more complicated since the resistances and exact lengths of the two wires are not necessarily the same and additional calibration constants are required to determine the coordinates of the ends of the wire at the hub.

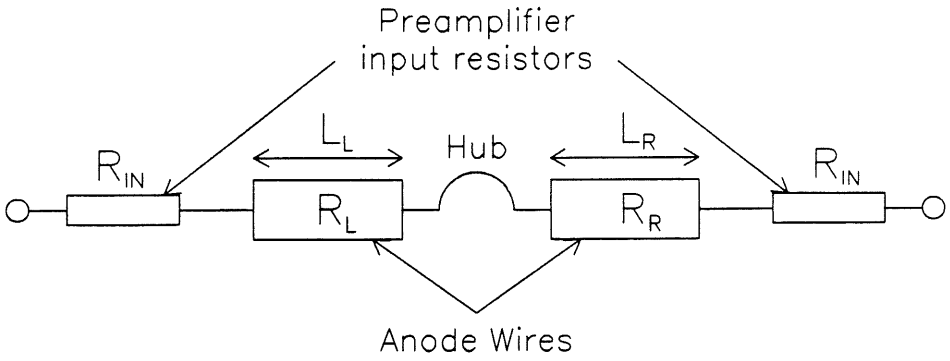

Figure 3.19: Schematic diagram showing the connection of two anode wires at the hub.

The radial coordinate of a hit on a wire in the RWDC is calculated using [31]:

$$r_{L,R} = r_{L,R}^{inner} \pm \frac{L_{L,R}}{2R_{L,R}} (\alpha R_{Total} + \Delta R) + \Psi(r) \tag{3.7}$$

where $r_{L,R}$ is the radial coordinate in either the *L*eft or the *R*ight wedge, $r_{L,R}^{inner}$ are the radial coordinates of the inner ends of the wires and $L_{L,R}$ are the lengths of the wires (figure 3.19). R_{IN} is the preamplifier input impedance which is assumed to be the same at each end. R_{Total} is the total wire resistance given by

$$R_{Total} = 2R_{IN} + R_R + R_L = (R_R + R_L)\frac{L_{eff}}{L} \tag{3.8}$$

where $\frac{L_{eff}}{L}$ is the ratio of the effective to the true wire length measured from test pulse data (section 3.5). α is defined by

$$\alpha = \frac{Q_L - \frac{G_L}{G_R}Q_R}{Q_L + \frac{G_L}{G_R}Q_R} \tag{3.9}$$

where $\frac{G_L}{G_R}$ is the relative gain of the two preamplifiers, again measured from test pulses and Q_L and Q_R are the measured charges on the pulses at either end. ΔR is the difference in the resistances of the two wires:

$$\Delta R = R_L - R_R \tag{3.10}$$

$\Psi(r)$ is a correction which has to be made to the radial coordinate to account for non-linearities due to changes in the pulse shape due to capacitive and inductive effects inside the chamber which affect the shapes of pulses as they travel along the wires. $\Psi(r)$ is discussed in detail in section 4.4 and in chapter 5.

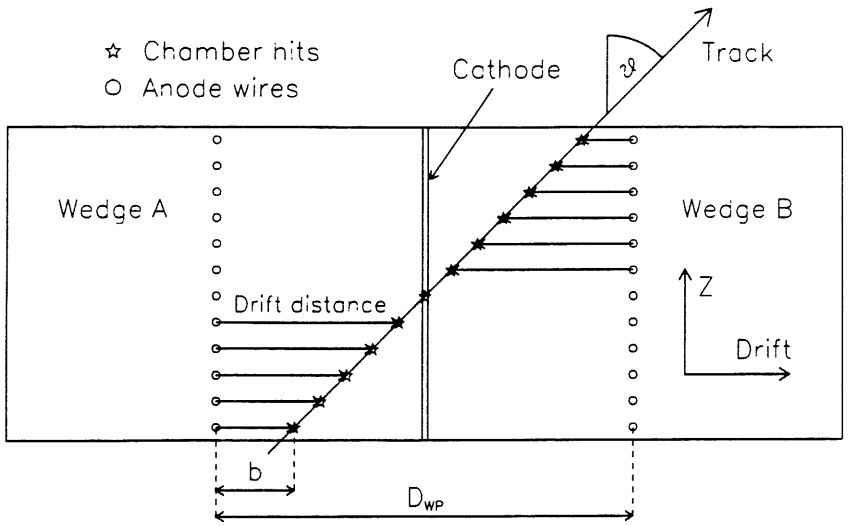

Figure 3.20: A track crossing the cathode plane boundary between adjacent RWDC wedges.

3.8.2 Radial Coordinate for Tracks Which Cross a Cathode

If a track crosses the boundary between two RWDC wedges it is possible to determine the radial coordinate of that track purely from the drift times. The first method described here applies only to tracks which are parallel to the beam pipe, the radii of which can be determined by a three parameter fit to a set of drift distances. A more complicated technique must be used when the tracks are at an angle to the beam pipe, which causes their radial coordinate to increase as they traverse the chamber.

Figure 3.20 shows a track which is parallel to the beam pipe where the left–right ambiguity of the space points has been resolved by the pattern recognition software so that the signs of the drift distances from each of the wire planes are known. Since the distance between wire planes D_{WP} varies with r according to

$$D_{WP} = 2r \tan 3.75^\circ \tag{3.11}$$

(3.75° being the angle between wire planes and cathodes in a RWDC) it is possible to determine r from a 3 parameter fit [32] using the function

$$Dr^i = az^i + b + D_{WP}N_W^i \tag{3.12}$$

where Dr^i are the drift distances from each wire plane, z^i are the z coordinates of the wires. a and b are the parameters used in a simple straight line fit, i.e. the tangent of

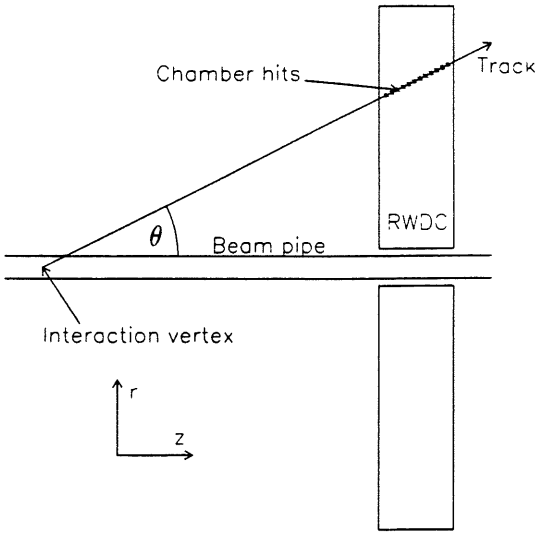

Figure 3.21: Schematic r–z view of a track originating from a vertex in the beam pipe.

the track angle ϑ and the drift coordinate of the first space point. N_W^i is set to zero in the first wedge and $N_W^i = 1$ in the second wedge. If the track were to pass through a third wedge this technique could easily be extended by setting $N_W^i = 2$ for hits in the third wedge.

Obviously, for any track originating at the interaction vertex in the beam pipe the radial coordinate of a track increases as it traverses the chamber (figure 3.21). The above technique needs to be extended to account for this extra variable. Figure 3.22 shows a section through the chamber taken along the track trajectory of figure 3.21. As the radial coordinate of the particle traversing the chamber increases so does the distance between the wire planes and the central cathode. The quantity ω in the figure is a function of the track angle to the beam pipe θ. The distance between the cathode and the wire plane D_{c-w} varies with r according to

$$D_{c-w} = r \sin 3.75^\circ \quad . \tag{3.13}$$

The radial position of the track r is given by

$$r = z \tan\theta \tag{3.14}$$

so

$$D_{c-w} = z \tan\theta \sin 3.75^\circ \tag{3.15}$$

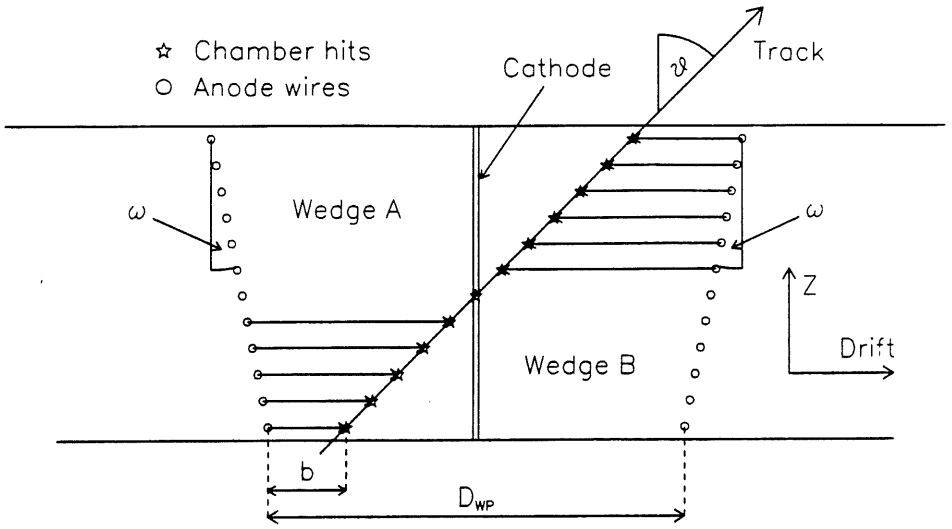

Figure 3.22: Section through two RWDC wedges along the trajectory of a track originating from the beam pipe.

and it follows that

$$\omega = \tan^{-1} \frac{dD_{c-w}}{dz} = \tan^{-1} \{\tan\theta \sin 3.75°\} \quad . \tag{3.16}$$

A four parameter fit is then used to allow for the extra variable:

$$Dr^i = az^i + b + D_{WP}N_W^i + \begin{cases} -z\tan\omega & \text{if } N_W = 0 \\ +z\tan\omega & \text{if } N_W = 1 \end{cases} \tag{3.17}$$

Figure 3.23 shows the results of the analysis of tracks crossing a cathode plane at an angle of 15°. The error is taken as the difference between the coordinate determined from the DWC and the traversing support and the radial coordinate calculated using the fit in equation 3.17. The central region of the plot, which contains 80 % of the data, has a gaussian width of 3.3 mm. It was shown in section 3.3.2 that the error on the beam coordinate is 1.1 mm, which indicates that the true error of the radial coordinate of a track segment measured in this way is $\sim$ 3.1 mm.

3.9 Summary

The test set-up described in section 3.3 enabled the study of many aspects of RWDC performance. In all of the gas mixtures tested, the drift velocity was constant on the central 10 wires but was generally lower on the front and back wires (table 3.2).

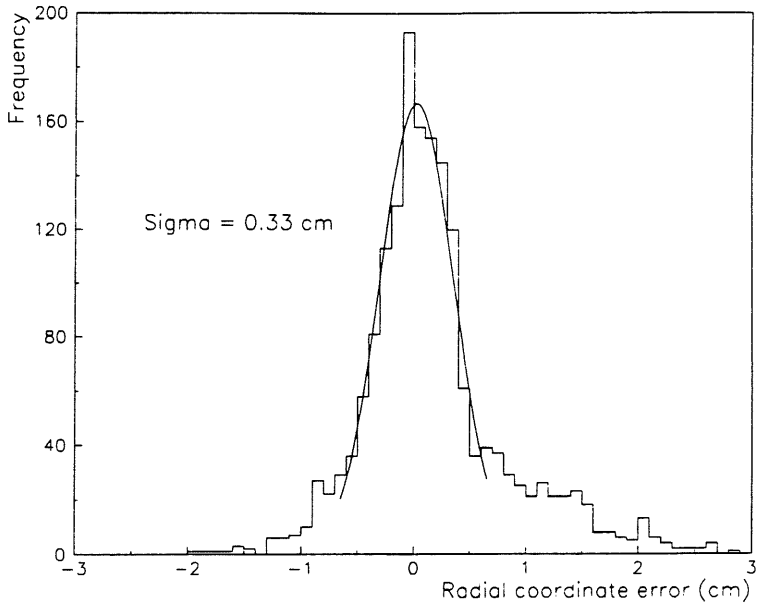

Figure 3.23: Comparison between the beam coordinate from the DWC and the traversing support and the radial coordinate determined from tracks crossing a cathode plane at an angle of 15°.

Drift velocity changes with electric field, pressure, temperature and the precise gas composition so the values obtained from these tests are not necessarily correct for use in H1 where conditions will be different. Possible methods of monitoring the drift velocity in the RWDCs installed in H1 are discussed in section 4.2.

Cross talk between adjacent wires has a large effect on the measured drift times. If two pulses are separated by $\sim$ 40 ns, the drift time of the later pulse can be increased by as much as 3 – 4 ns which corresponds to a drift error of 150 – 200 μm in a typical chamber gas. A method of correction for the effect of cross talk was presented in section 3.7.2, although it is clear that more data is required at angles between the 5° intervals available from the tests at CERN. It will also be necessary to see how well the correction works in the high multiplicity environment of H1 where pulses from more than one track may affect each other.

Charge division in a RWDC is made slightly more complicated than in a conventional chamber due to the connections at the hub and the possibility of different wire resistances in each cell. Although not directly applicable to track reconstruction in H1 a unique feature of the radial geometry is that radial coordinates may be calculated

purely from a knowledge of the drift times for tracks which cross a wire plane. Only a single value of r is obtained from each track using this technique but a single coordinate which is accurate to ± 3.1 mm gives the same overall precision as 12 coordinates each accurate to ± 12 mm. During the tests at CERN the best precision achieved from the charge division measurement (section 4.5) was 2.5 cm, giving an accuracy of 7.2 mm over 12 wires.

Chapter 4

Space Point Precision in Radial Wire Drift Chambers

4.1 Introduction

Measurements of both the drift ($r\phi$) and the charge division coordinate (r) are subject to errors which divide into two distinct categories: systematic errors and random errors. In principle, all systematic errors can be understood and eliminated during track reconstruction. Random errors will always exist in any measuring system at some level and set a limit to the ultimate resolution possible with that system. The sources of systematic and random drift and charge division errors in a RWDC are summarized in table 4.1.

This chapter discusses the sources and magnitudes of these errors and shows how the systematic errors may be eliminated both through the use of test data from CERN and by continual monitoring of RWDC data from the H1 experiment.

4.2 Systematic Drift Coordinate Errors

4.2.1 Variations in the Drift Velocity

To fully exploit a point precision in the RWDC of $\sim 200\,\mu$m at a mean drift distance of 3.2 cm it is necessary to know the drift velocity to an accuracy of 0.2 %. It has

	Systematic Errors	Random Errors
Drift coordinate	Incorrect Drift Velocity	Inherent timing resolution with 9.6 ns FADCs
	Track angle effects	
	Incorrect Gt_0	
	Geometrical errors	Diffusion of drifting electrons
	Cross talk	
Charge division coordinate	Inherent non-linearity	Electrical noise
	Lorentz angle	
	Geometrical errors	

Table 4.1: Sources of drift chamber space point errors.

already been shown in section 3.6 how slight changes in the electric field can affect the drift velocity by up to 6 %. The drift velocity also changes with the pressure and temperature of the gas and is sensitive to the exact concentrations of the different gases as well as impurities such as water. To avoid pressure differences of $> 50\ \mu$bar across the RWDC front window the pressure inside the RWDC must match the pressure inside the transition radiator gas volume, which in turn follows ambient atmospheric pressure. Due to warming by the preamplifiers, the temperature of the gas in the RWDC is generally a few degrees higher than the ambient temperature in the H1 pit and, like the pressure, varies during the day. Gas concentrations do not vary as rapidly as temperature and pressure but can change over a period of several days as gases diffuse through the front window and FTD gas tank seals. The end result is that the drift velocity in the RWDCs may vary by several percent over a 24 hour period and must therefore be continually monitored. As an example, figure 4.1 [33] shows the measured variation of drift velocity with electric field and Ethane concentration in Ar:C_2H_6 gas mixture.

Most of the methods of drift velocity monitoring described here are only sensitive to *changes* in the drift velocity rather than giving an absolute measurement to within

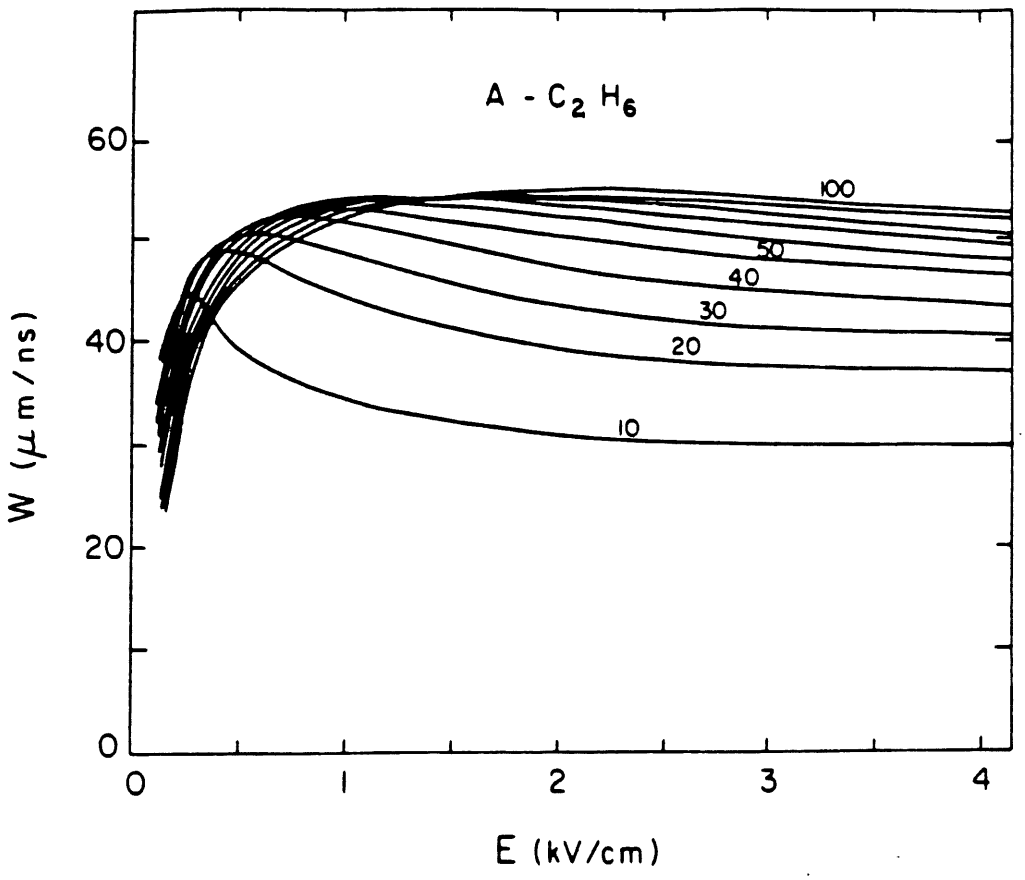

Figure 4.1: Electron Drift Velocity in Ar:C_2H_6 gas mixture for ten different ethane concentrations.

0.2 % and it is not yet clear which of the methods will be the most reliable at that. Since all of the methods described have their advantages and their draw backs, it will be necessary to try all of them and reach agreement between at least two of them.

4.2.1.1 Drift Velocity Monitor

It is possible to build a small wire chamber designed specifically to monitor the drift velocity in the RWDC gas under a given set of operating conditions [33]. Such a chamber would be connected into the gas outflow pipes from the RWDCs and mounted within the H1 solenoid so as to operate in exactly the same gas mixture and magnetic field as the RWDCs.

It has already been shown in section 3.6 that the drift velocity is sensitive to the precise field configuration, particularly close to the edges of the drift cells. It is therefore

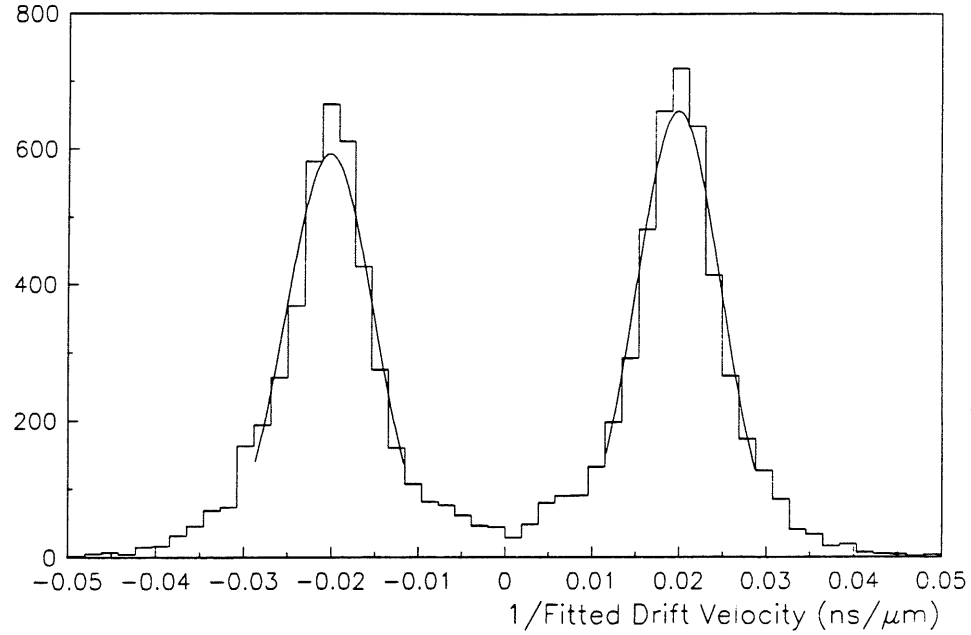

Figure 4.2: Distribution of fitted inverse drift velocities for tracks parallel to the wire plane.

unlikely that such a monitor could produce an accurate absolute measurement of the drift velocity. It would also be necessary to ensure that the pressure in the monitor is the same as that in the chambers. This would not be the case unless it was mounted very close to the outlet of one of the chambers to avoid pressure differentials due to gas flow in the pipes. Although a drift velocity monitor would not give an absolute measurement it would still be sensitive to changes in the drift velocity.

4.2.1.2 Drift Velocity From Fitted Track Segments

A fit to a set of drift times which includes the drift velocity as a free parameter (V_D^F) has been given in equation 3.3. A typical distribution of fitted inverse drift velocities for tracks parallel to the wire plane, after cross talk compensation, is shown in figure 4.2. Negative values of drift velocity in figure 4.2 correspond to tracks resolved on the negative side of the wire plane. Gaussian fits to the central regions of the two peaks give values of drift velocity of $49.51 \pm 0.23\,\mu$m/ns and $50.18 \pm 0.21\,\mu$m/ns respectively. The exact value of drift velocity obtained from this method is sensitive to the distribution of track angles and the parametric cross talk compensation described in section 3.7.2. As for the drift velocity monitor this method would again be sensitive to changes in

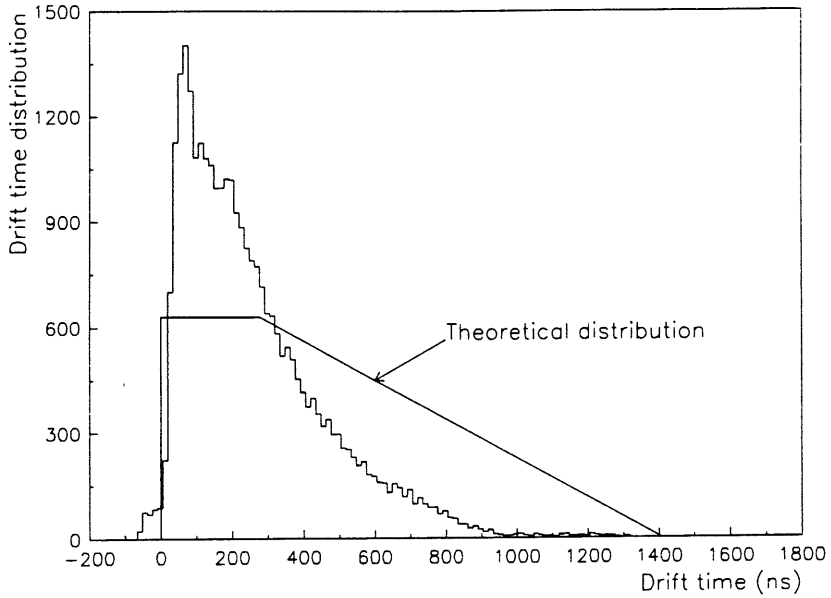

Figure 4.3: Drift time distribution in a RWDC showing a theoretical line for uniform illumination of a RWDC and a typical distribution from an *ep* physics run in H1.

the drift velocity rather than providing an absolute measurement.

4.2.1.3 Drift Time Distribution Method

A common method of measuring drift velocity is to look at the over-all distribution of drift times in a chamber. If the chambers were illuminated uniformly the distribution would be like the theoretical line drawn in figure 4.3 given nominal chamber geometry, a drift velocity of 50 μm/ns, and a Lorentz angle of 45°. In practice the illumination of the RWDCs is far from uniform, the beam intensity being much higher close to the beam pipe. Changes in the beam conditions at HERA and changes in the H1 trigger could also affect the distribution of drift times. A typical distribution of drift times from the RWDCs installed in H1 is also shown in figure 4.3 [34].

4.2.1.4 Comparison With PWDC Track Segment Data

A final method of determining drift velocity in the RWDCs is a comparison between drift times in the RWDCs and drift distances projected from track segments in the PWDCs (section 2.1). This is in fact a very similar method to that described in section 3.6 where tracks were projected into the RWDC from the DWC. This method does

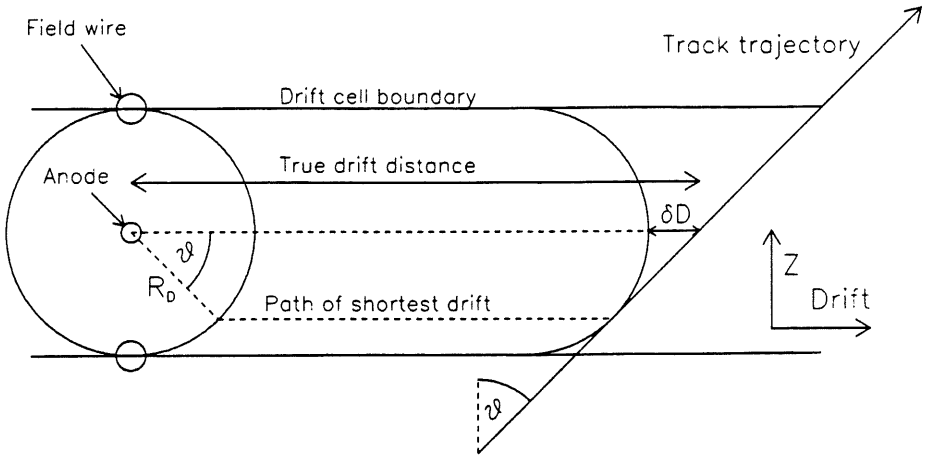

Figure 4.4: Schematic diagram of a drift cell showing a construction of the track angle correction.

of course require a good knowledge of the PWDC's but due to the very different geometries of the PWDCs and the RWDCs there should not be a strong correlation between the drift velocity obtained for the RWDC and errors in the PWDC reconstruction.

At the time of writing the pattern recognition software for the planar chambers has not yet provided enough data for this method to be tried. Potentially however it is a method which will give an *absolute* measurement of drift velocity in the RWDCs.

4.2.2 Drift Time Origin Gt_0 and Track Angle Correction

An error Δt_0 in the drift time origin Gt_0 will lead to an error in the reconstructed drift coordinates. It is necessary to know Gt_0 to an accuracy of $\sim$ 1 ns in order to keep systematic errors in a track position below 50 μm.

The simplest model of electron drift in a RWDC consists of linear drift perpendicular to the wire plane up to a constant radius R_D from the anode and then radial drift towards the anode (figure 4.4). Naïvely one would expect R_D to be equal to the spacing between anode and field wires. Due to focussing effects of the negatively charged field wires, however, R_D is smaller than the anode – field wire spacing. For track reconstruction it is necessary to know the coordinate of the track at the center of the drift cell, so a correction δD must be made to the drift distances based on the track

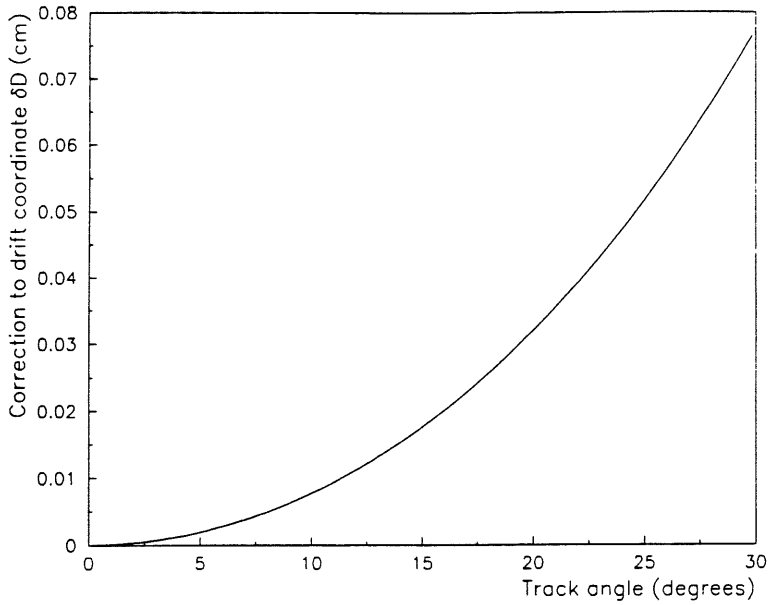

Figure 4.5: Track angle correction δD with the radius at which the drift become radial $R_D = 0.5$ cm.

angle ϑ and R_D [31] where

$$\delta D = R_D\,(\sec(\vartheta) - 1) \approx R_D \frac{\vartheta^2}{2} \quad . \tag{4.1}$$

This correction is plotted in figure 4.5 for $R_D = 0.5$ cm.

The effect of the track angle correction on the positions of space points is similar to an error in the drift time origin. In both cases all of the space points are moved towards or away from the wire plane. It is therefore necessary to examine these two effects together.

For tracks which cross a wire plane Δt_0 may be determined by making a 3 parameter least squares fit [32] to the space points:

$$Dr_i = az_i + b + \Delta t_0 V_D Side_i \tag{4.2}$$

where Dr_i are the signed drift distances from the center of the wire plane. z_i are the z coordinates of the space points and $Side_i$ is set to $+1$ for a point on the '+' side of the wire plane and -1 for point on the '$-$' side (figure 4.6). a and b are the tangent of the fitted track angle and intercept as for a linear (first order polynomial) straight line fit.

Obviously, tracks which are parallel to the wire plane will not cross it and it is not possible to measure Gt_0 using the above technique. It is however possible to measure

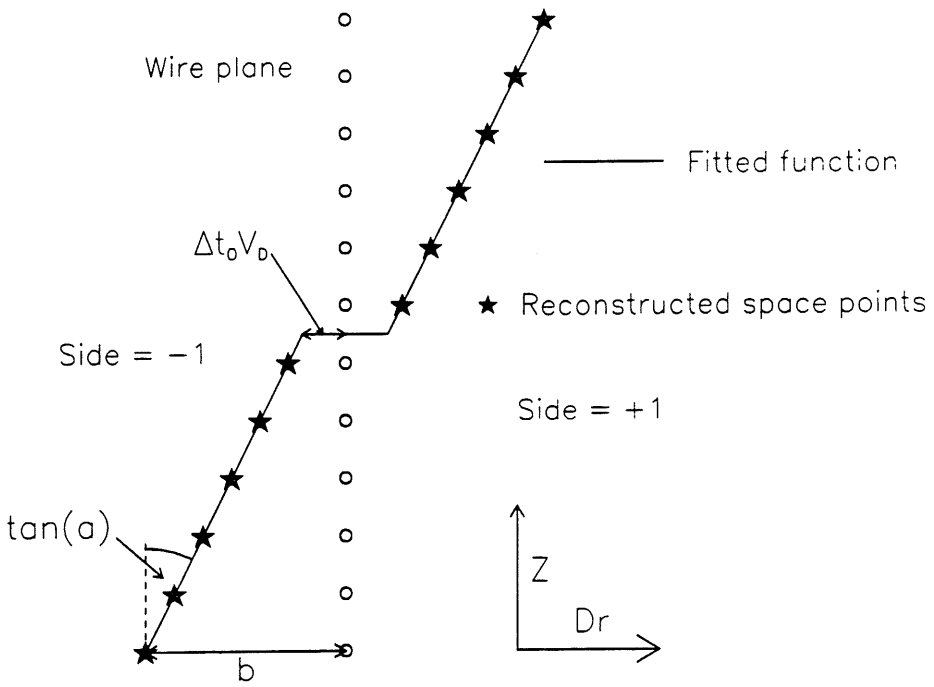

Figure 4.6: Schematic diagram showing the parameters of the fit used to determine the drift time origin for tracks which cross a wire plane.

Gt_0 for such tracks by studying the distribution of drift times in the chamber. If a wedge of a RWDC were uniformly illuminated, the distribution of drift times should ideally start with a step function similar to that in figure 4.3. In practice, the step is offset from zero by the amount Δt_0 and smeared over a few ns due to random errors inherent in the drift coordinate measurement. With test beam data it was not possible to illuminate uniformly a complete wedge since the beam spot was relatively small and had to be scanned across the chamber. However, by positioning the beam spot directly over a wire plane it was possible to produce a satisfactory step function and measure Δt_0 since the width of the leading edge of the distribution is small compared to the beam spot size.

Figures 4.7.a and 4.7.b show the distribution of drift times for a beam spot centered over the wire plane on two different time scales. The center of the leading edge gives the error Δt_0. It is measured by fitting a gaussian to the gradient of the leading edge of the distribution as shown in figures 4.7.c and 4.7.d. Figure 4.7.d represents the same data after Gt_0 has been corrected using the mean of the fit in figure 4.7.c. When determining Gt_0 in this manner it is important that all of the drift times are used rather than only

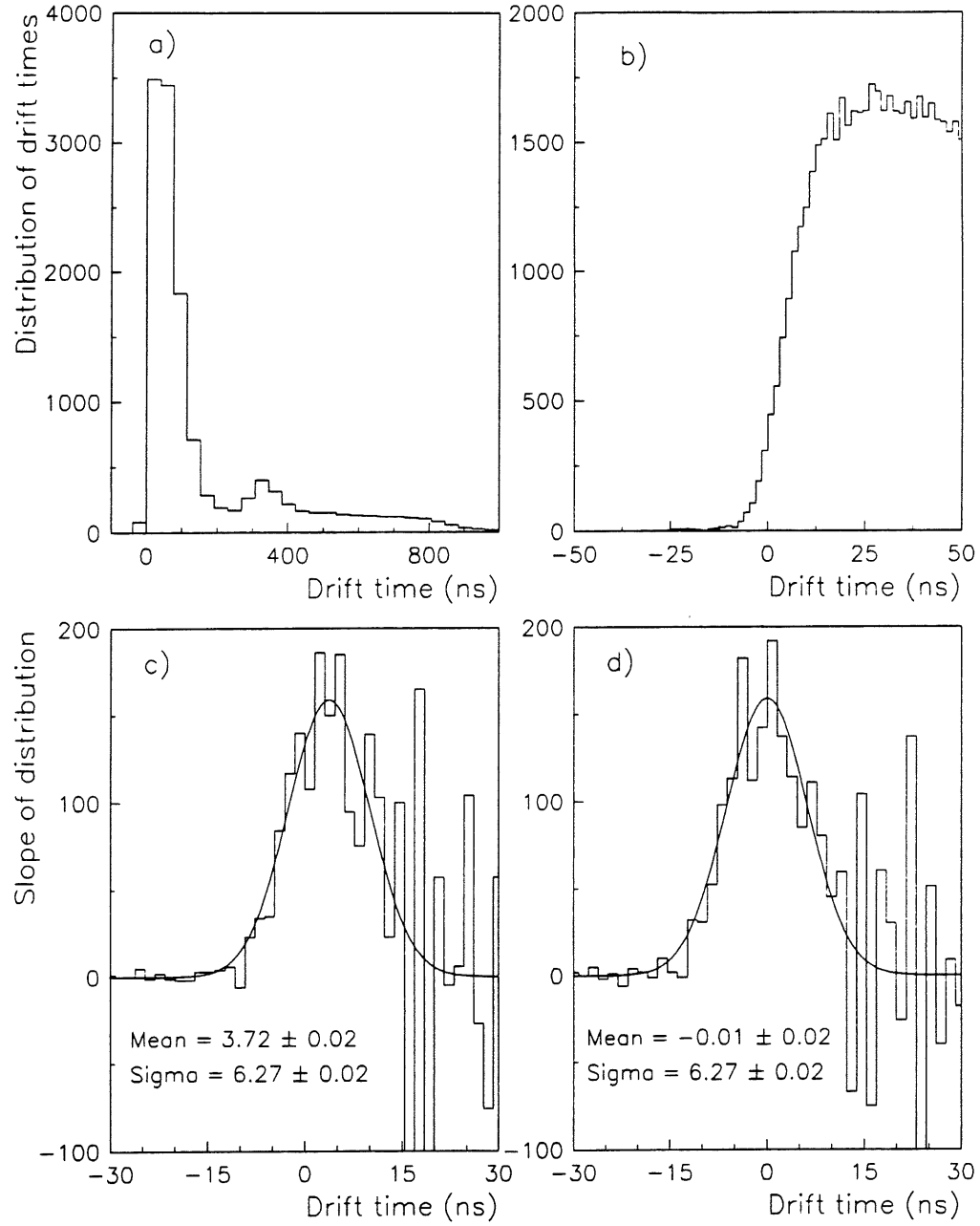

Figure 4.7: Drift time origin t_0 for tracks which do not cross a wire plane. (a) and (b) show the distribution of drift times on two different scales. (c) shows the gradient of (b), the position of the central peak of (c) being the center of the rising edge of (b) which is the error in the drift time origin, Δt_0. In (d) Δt_0 from (c) has been used to correct the global drift time origin Gt_o which moves the center of the distribution close to zero.

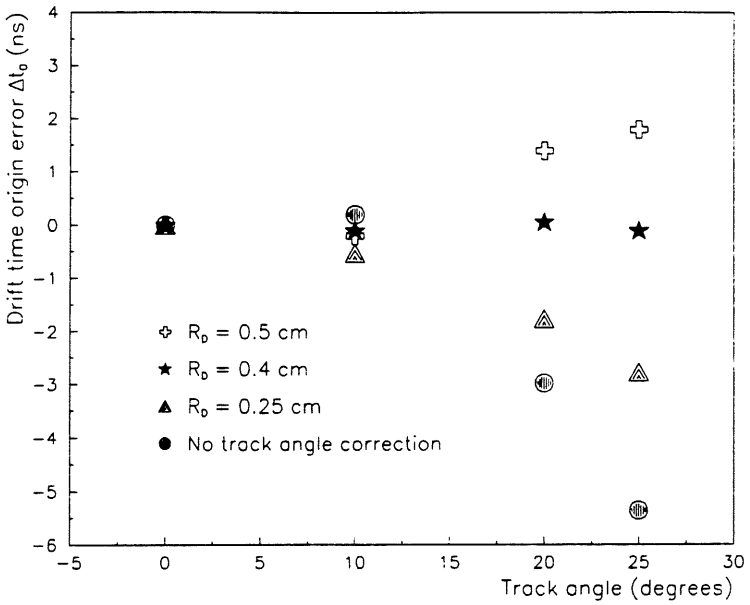

Figure 4.8: Measured errors in the global drift time origin Gt_0 with different values of the track angle correction constant R_D, the distance from the wire plane below which the drift becomes radial.

those which have been accepted by the pattern recognition. This is because variations in the efficiency of the pattern recognition for tracks very close to the wire plane may be different to those in the rest of the chamber, which would tend to move the leading edge of a plot such as that in figure 4.7.b to the right, and therefore give an incorrect value of Gt_0.

Figure 4.8 shows the error in Gt_0, which was measured using the two techniques described above, for angled tracks and for tracks parallel to the wire plane, with different values for R_D in equation 4.1. As expected, the results indicate that setting R_D = 0.4 cm, which is slightly smaller than the actual spacing between anode and field wires, produces the minimum variation in Δt_0 at angles between 0° and 30°. Data where tracks cross a wire plane were only taken at angles of 10°, 20° and 25° in Ar:C_2H_6 50:50 gas mixture. The operating fields in the Xenon based gases which will eventually be used in the RWDCs are likely to cause subtle differences in the field close to the wire planes, which is likely to affect the optimum value of R_D. It will therefore be necessary to repeat these measurements when the operating conditions of the RWDCs in H1 are altered.

4.2.3 Geometrical Corrections and Wire t_0

The wires in the RWDCs are within $\pm 38\mu$m of their nominal positions [10]. It is possible to measure the precise relative positions of the wires in each wedge and the drift time origin t_0 for each wire using the fit residuals to a simple two parameter straight line fit to track segments from each side of the wire plane.

If $\delta Dr^{\pm}$ are the mean residual errors to the fitted tracks for tracks on the + and the − sides of the wire plane, δs is the geometrical error in the position of that wire and δt_0 is the error in t_0, then for points on a track on the + side of the wire plane

$$\delta Dr^{+} = \delta s + V_D \delta t_o \tag{4.3}$$

and on the − side of the wire plane

$$\delta Dr^{-} = \delta s - V_D \delta t_o \tag{4.4}$$

where V_D is the drift velocity.

It is therefore simple to extract δs and δt_0 from measurements of δDr^{+} and δDr^{-} since

$$\delta s = \frac{\delta Dr^{+} - \delta Dr^{-}}{2} \tag{4.5}$$

and

$$\delta t_0 = \frac{\delta Dr^{+} + \delta Dr^{-}}{2V_D} \quad . \tag{4.6}$$

Figure 4.9 shows the results of the analysis of 10000 tracks on each side of a wire plane using data collected in the CERN test beam. Figures 4.9.a and 4.9.b show the mean fit residuals to the tracks for each of the 12 wires on the + and − sides of the wire plane respectively. Equations 4.5 and 4.6 were used to calculate the geometrical errors δs and the time errors δt_0 which are shown in figures 4.9.c and 4.9.d. The rms variation of the corrections applied to the wire positions is 38 μm which is completely consistent with the expected construction error (section 2.2.1) and the correction to the time origins has a rms variation of 0.35 ns. δs and δt_0 were then used to update the RWDC calibration tables and a second set of data from similar positions in the two wedges analyzed. It can be seen from figures 4.9.e and 4.9.f that there is a marked

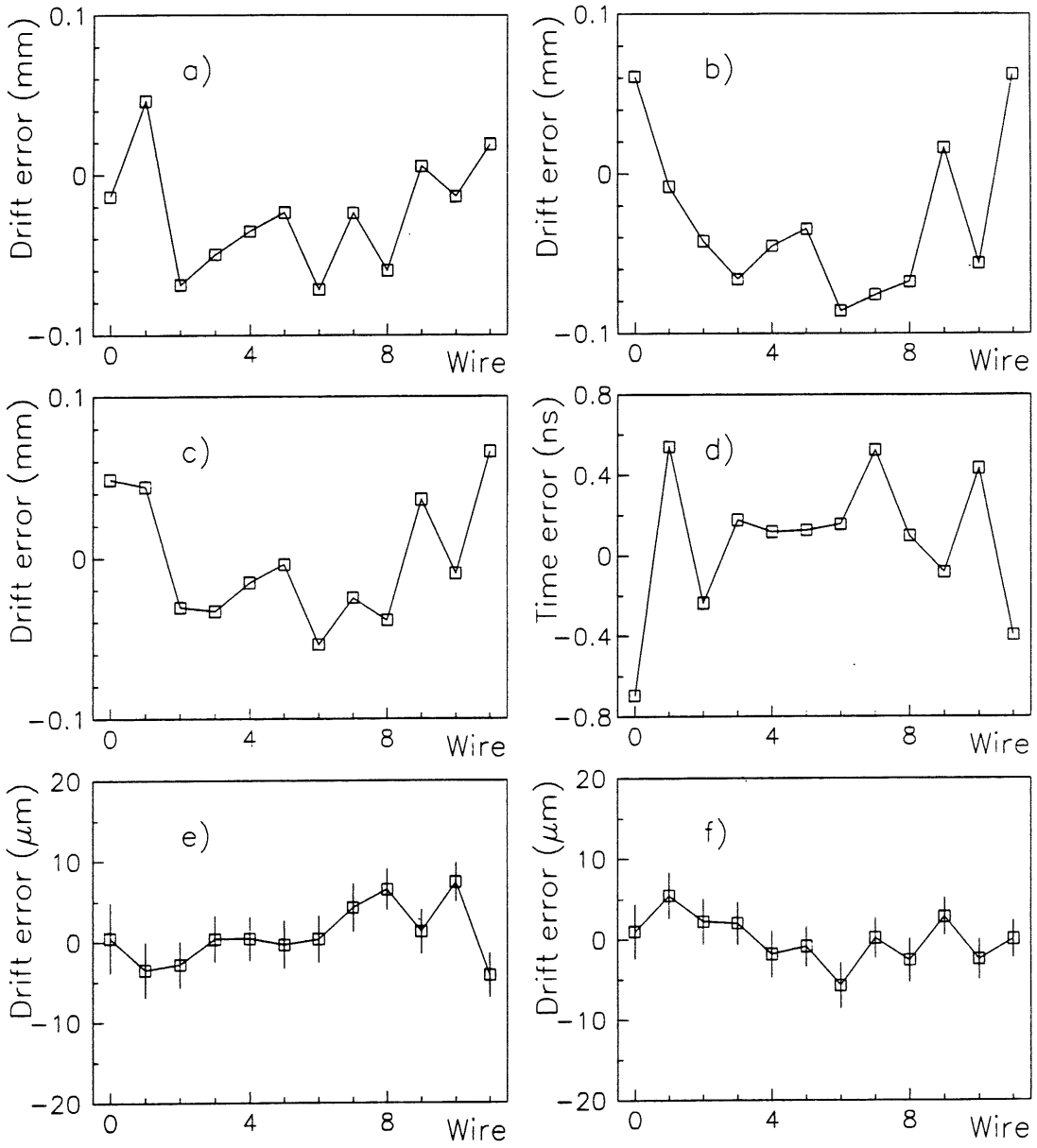

Figure 4.9: Geometrical and t_0 errors and correction. (a) and (b) are the errors $\delta Dr^{\pm}$ which are the mean fit residuals to fitted track segments on each side of the wire plane. (c) is the error in the position of each anode wire and (d) is the timing error δt_0 on each wire which are calculated from the points in (a) and (b). (e) and (f) are the results of analyzing a second set of data similar to that in (a) and (b) using the corrections from (c) and (d).

improvement from a rms variation of $\pm 400\,\mu$m to $\pm 3\,\mu$m in the mean fit residuals when the geometrical and timing errors have been eliminated.

The above analysis only allowed for a single offset in the position of each wire. It is of course possible that the offset in the position of the wire will be different at each end due to different construction errors in the Noryl hub and templates which support the ends of the wires. Test beam data were only taken on both sides of a wire plane at a single radius near the wide end of a wedge. Using data from the RWDCs in H1 it will be necessary to use the above technique at different radii to determine δs for each end wires in the RWDCs.

4.3 Random Drift Coordinate Errors

Once all of the systematic errors in the drift coordinate measurement have been removed using the methods described above, what remain are the random errors on the individual space points. There are three sources of random errors which affect drift coordinates:

1. The inherent timing resolution of FADCs sampling every 9.6 ns.
2. Diffusion of electrons in the charge cloud.
3. Non-linearities in the drift field close to the wire plane.

If drift times were taken simply as the bin of maximum DOS on the leading edge of each pulse, the best possible timing resolution would be 2.7 ns ($\frac{1}{\sqrt{12}} \times 9.6$ ns)[†]. Using the techniques described in section 3.4 where information from two bins is used it is possible to keep this minimum timing error at ~ 2.9 ns (0.3 FADC bins).

Due to diffusion of drifting electrons the distribution of individual electrons about the center of the drifting charge cloud is gaussian in shape with a width σ_x:

$$\sigma_x = \sqrt{2Dt} \tag{4.7}$$

where D is the diffusion coefficient of the gas and t is the drift time. As the drift distance increases and the charge cloud becomes more diffuse the arrival time of the

[†] If integer timing were used the distribution of errors would be a 'top hat' function of unit width. The rms variation of such a distribution is $1/\sqrt{12}$ of a unit.

charge cloud becomes increasingly uncertain. σ_x represents the uncertainty in position of individual electrons in the charge cloud. The uncertainty in the position of the center of the charge cloud is therefore $\sigma_x/\sqrt{N}$ where N is the total number of drifting electrons. The error due to diffusion is generally somewhere between σ_x and $\sigma_x/\sqrt{N}$ depending on the fraction of the total charge used in the timing algorithm.

Finally, as the field inside the chambers increases close to the wire plane and the relationship between time and distance is no longer linear there is generally a drop in the drift precision close to the wire plane. It is therefore sensible to parameterize the relationship between the space point precision σ_d and the drift distance d with

$$\sigma_d^2 = \sigma_1^2 + \sigma_2^2 d + \sigma_3^2 F(d) \tag{4.8}$$

where σ_1 is the error due to the inherent timing resolution of the FADCs and the timing algorithms. $\sigma_2\sqrt{d}$ is the error due to diffusion and $\sigma_3\sqrt{F(d)}$ accounts for the additional errors close to the wire plane. There is no obvious form for $F(d)$ except that it must only become a relevant factor at short drift distances. Here I have used $F(d) = e^{-4d}$ where d is measured in cm.

The point precision is measured by making simple straight line two parameter fits to the space points in pattern recognized track segments. Since the straight line fit has 2 free parameters, the actual error for each space point is $\sqrt{N/(N-2)}\times$ the distance between each space point and the fitted line where N is the number of space points making up the track segment. The residuals from the points on all of the wires are used together and the drift precision is taken as the gaussian width of the residuals at a given drift distance. Figures 4.10 and 4.11 show the drift precision plotted against drift distance in Ar:C_2H_6 50:50 and Xe:He:C_2H_6 15:45:40 gas mixtures respectively. Also in the figures are the three errors σ_1, $\sigma_2\sqrt{d}$ and $\sigma_3\sqrt{F(d)}$ which are derived from 3 parameter fits of equation 4.8 to the points in the figures. As expected, the error due to the timing resolution of the FADCs is smaller in the Xe based gas due to the lower drift velocity. The diffusion term, however, is larger in the Xe based gas, as would be expected from equation 4.7 for similar diffusion coefficients in each gas. σ_1 and σ_2 are listed in table 4.2 for four different gas mixtures.

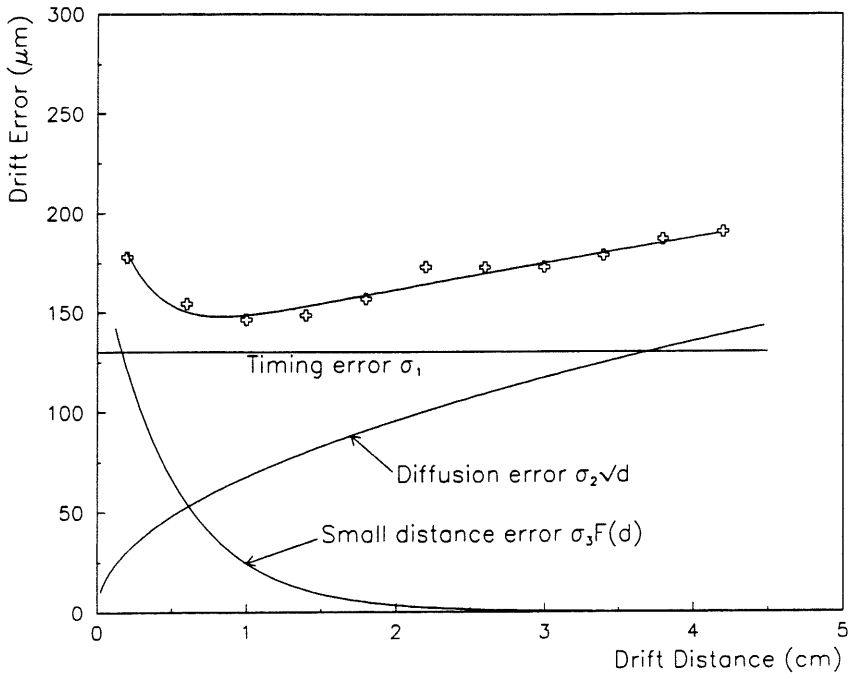

Figure 4.10: Drift precision in Ar:C_2H_6 50:50 gas mixture.

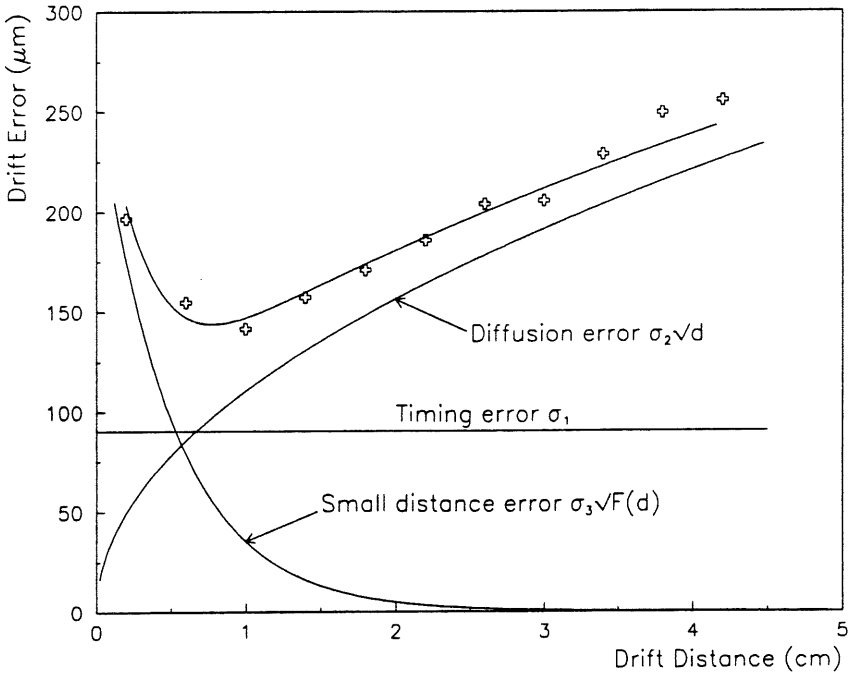

Figure 4.11: Drift precision in Xe:He:C_2H_6 15:45:40 gas mixture.

Gas		Electric Field kV/cm		Drift errors		
		Drift	anode	σ_1 μm	σ_2 $\mu m/\sqrt{cm}$	σ_3 μm
$Ar:C_2H_6$	50:50	1.2	170	130	68	180
$Xe:He:C_2H_6$	15:45:40	1.2	160	90	110	260
	20:40:40	1.2	160	110	123	250
	30:40:30	1.2	160	116	126	253

Table 4.2: Contributing factors to the drift precision of RWDCs in different gas mixtures. σ_1, σ_2 and σ_3 are defined in equation 4.8.

4.4 Systematic Charge Division Errors

A large systematic error which affects the charge division coordinate was first observed during tests of the three production RWDCs in Liverpool. A collimated Fe^{55} X-ray source was placed against the front window and the positions of the reconstructed radial coordinates compared with the measured position of the source. Figure 4.12 shows how the difference between the position of the mean reconstructed coordinate and the position of the x-ray source varied with the radial coordinate using the simplest possible form of the charge division reconstruction equation:

$$\frac{r}{L} = \frac{L_{eff}}{L}\frac{Q_L - Q_R}{Q_L + Q_R} \tag{4.9}$$

Calibration of the preamplifiers using the techniques described in section 3.5 was not possible with the test set-up used for this measurement so no correction was made for the relative gains of the preamplifiers which can account for the over-all positive shift in the results. It can not, however, account for the large fluctuations of the error with the radial coordinate.

This systematic shift was measured again during the tests at CERN by making a comparison between reconstructed charge division coordinates in the RWDC and the beam position from the traversing support and the DWC. The results, which are shown

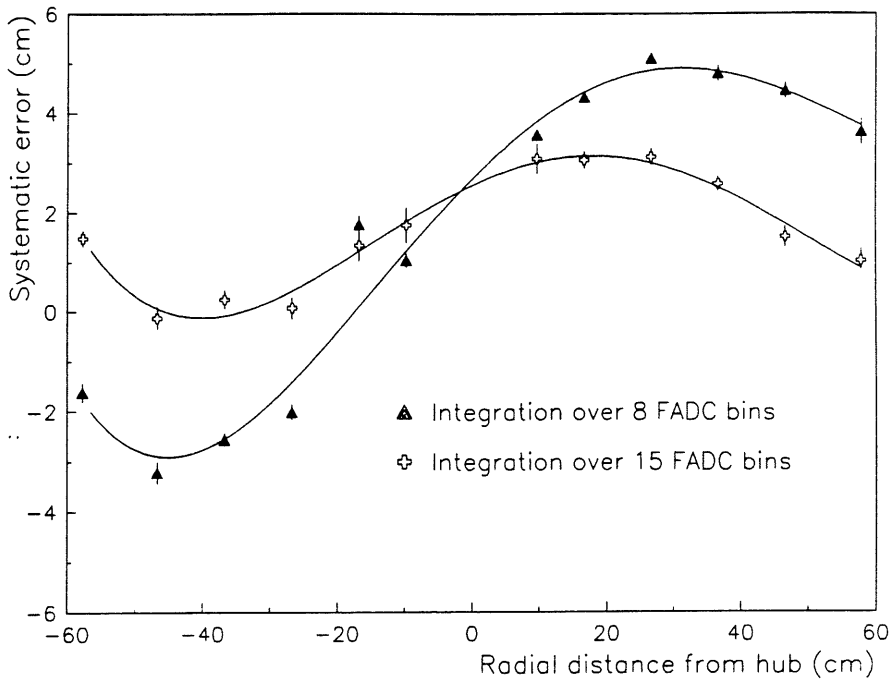

Figure 4.12: Charge division systematic error measured with a collimated Fe^{55} x-ray source. Results are shown for two different integration times. The fitted lines are 5^{th} order polynomial and are included only to guide the eye.

in figure 4.13 for different charge integration intervals, again show a large systematic error, but its form is quite different to that measured for x-rays. The reasons for the difference between the two measurements are:

- The pulse shape from x-ray ionization in the chamber is different to that from the track of an ionizing particle.
- The output of the preamplifiers used during the tests in Liverpool had been modified to overcome a problem of compatibility with the FADCs used in those tests which would also have caused a change in the pulse shape.

The systematic error shown in figure 4.13 is compensated for during reconstruction in the term $\Psi(r)$ in equation 3.7 which must clearly be different for each integration time. There is no obvious physical form for $\Psi(r)$ but it can easily be approximated for each integration time by a polynomial function of r where the order of the polynomial depends on the accuracy required. If a simple first order (i.e. a straight line) correction is used then the residual systematic errors after the correction has been applied are

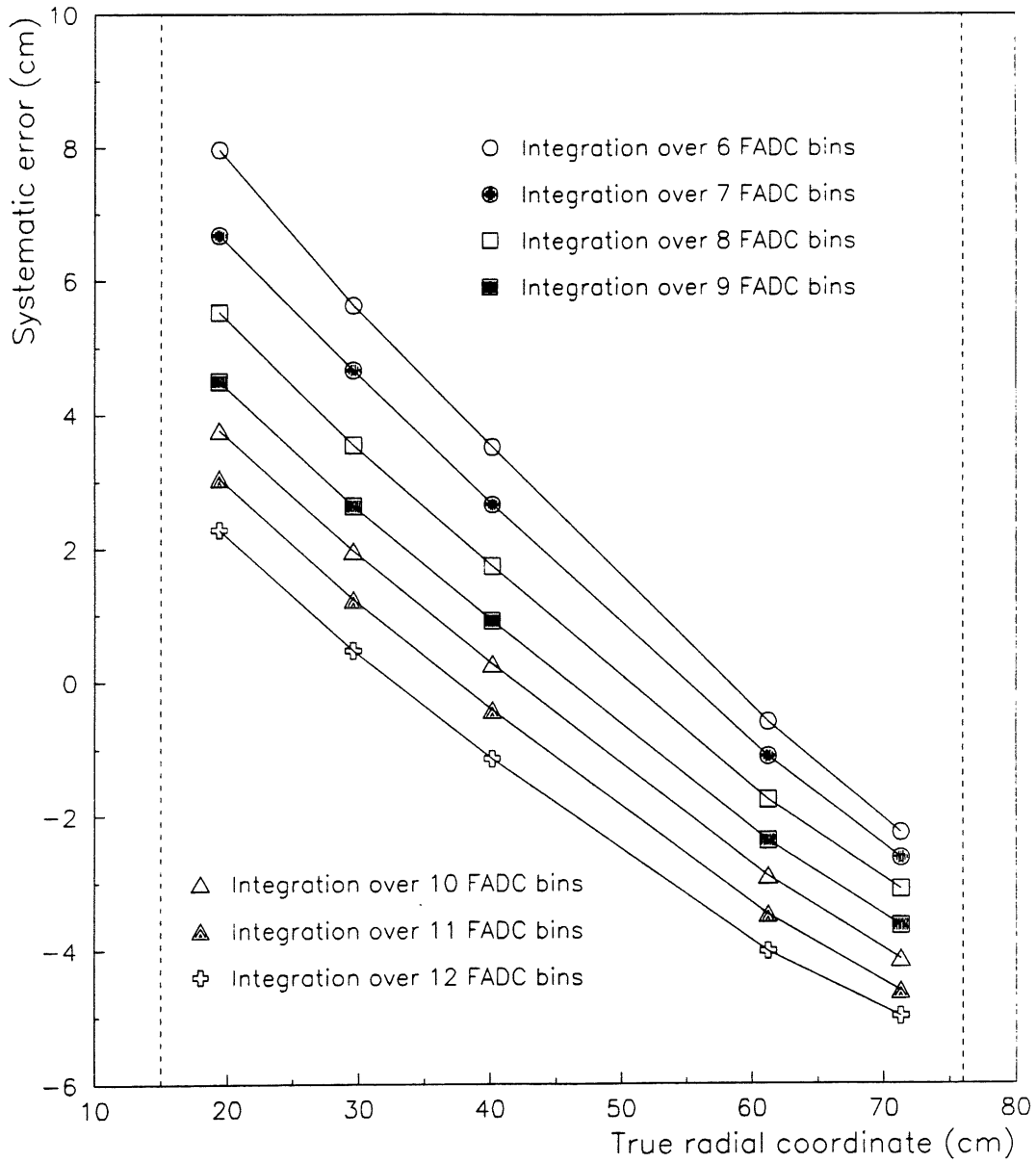

Figure 4.13: Charge division systematic error measured with a 50 GeV electron beam at CERN. The dotted lines on each side of the figure represent the minimum and maximum sensitive radii of the RWDC. (The true radial coordinate is the distance measured from the center of the beam pipe.)

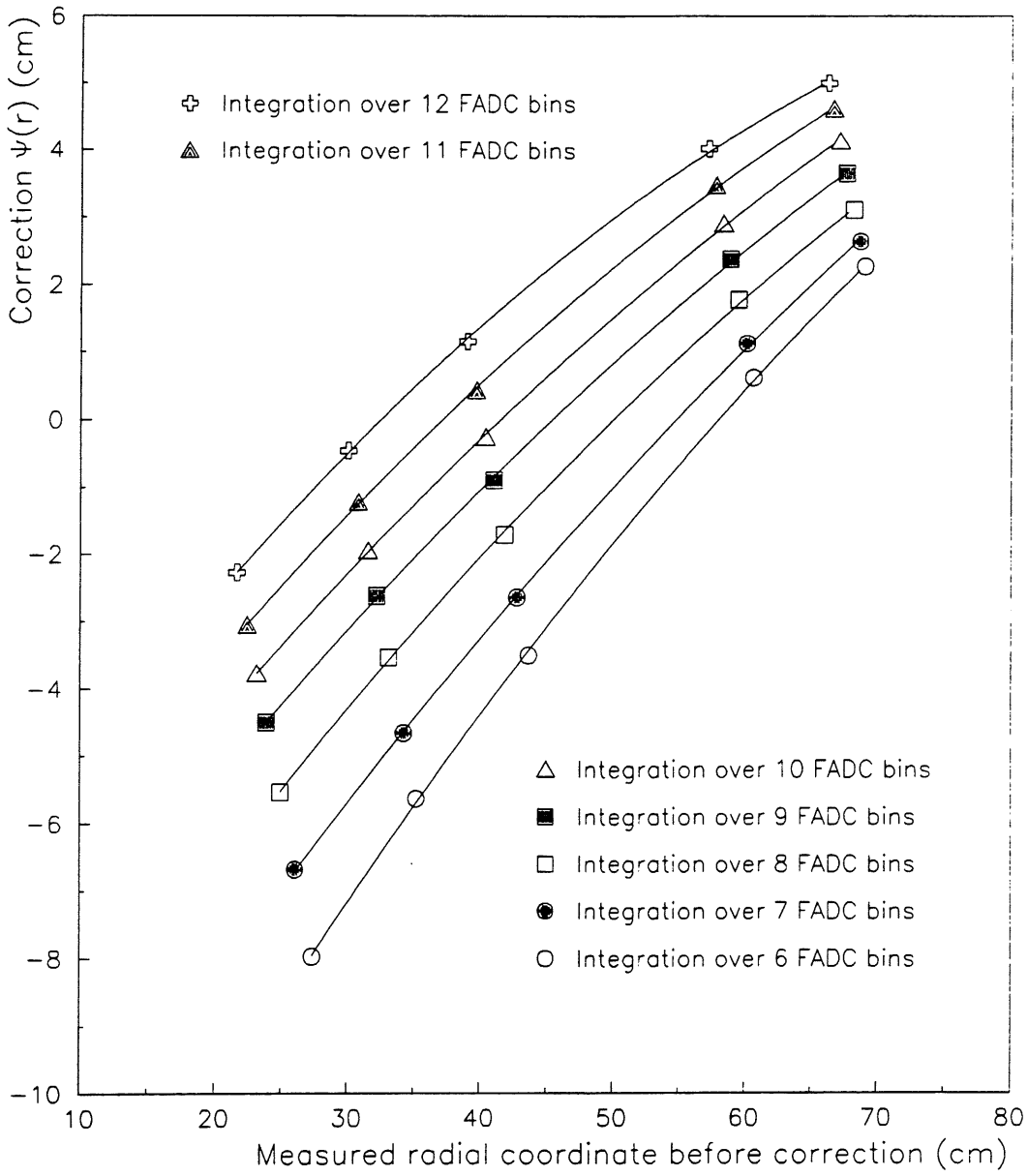

Figure 4.14: Correction to radial coordinate $\Psi(r)$. The parameters of the fitted functions, which are 2^{nd} order polynomial, are given in table 4.3.

Integration time (FADC bins)	3^{rd} order correction			2^{nd} order correction	
	$\alpha \pm 0.15$ (cm)	$\beta \pm 0.007$	$\gamma \pm 0.00007$ (/cm)	$\alpha \pm 0.35$ (cm)	$\beta \pm 0.007$
6	-17.0	0.361	-0.00123	-14.40	0.245
7	-14.1	0.307	-0.00092	-12.22	0.219
8	-12.3	0.298	-0.00105	-10.26	0.199
9	-10.5	0.275	-0.00096	-8.72	0.186
10	-9.4	0.264	-0.00093	-7.72	0.180
11	-8.6	0.270	-0.00109	-6.67	0.173
12	-7.8	0.281	-0.00133	-5.49	0.163

Table 4.3: The parameters of the correction $\Psi(r)$ used in charge division coordinate determination. The errors at the top of each column are typical for all of the values in that column.

~ 0.25 cm for all integration times. A second order correction improves matters further, leaving residual errors of ~ 0.5 mm. Figure 4.14 shows the correction $\Psi(r)$ as a function of the *measured* radial coordinate r before the correction is applied. Fitted to the data for each integration time is the second order polynomial function:

$$\Psi(r) = \alpha + \beta r + \gamma r^2 \tag{4.10}$$

the parameters of which are summarized for each integration time in table 4.3. Also in the table are the parameters of the more simple 2 parameter fit to the points:

$$\Psi(r) = \alpha + \beta r \quad . \tag{4.11}$$

Using data from H1 it will be possible to confirm and monitor the systematic charge division error by making a comparison between RWDC radial coordinates and PWDC track segments projected into the RWDCs. A detailed discussion of the way in which RWDC pulses form and the effect that the pulse shape has on the charge division coordinate is given in chapter 5.

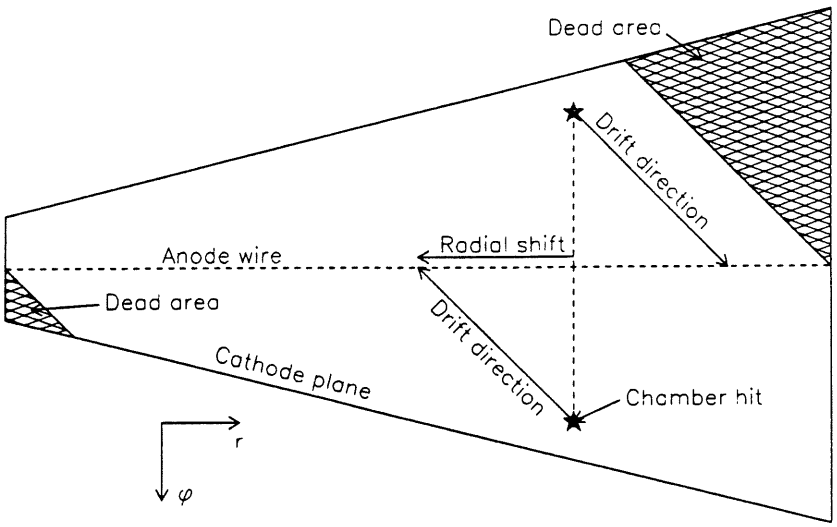

Figure 4.15: Schematic diagram of a RWDC wedge showing the effect of Lorentz angle on radial coordinates.

When the RWDCs are operated in the presence of a magnetic field it is also necessary to correct the radial coordinates for the effects of Lorentz angle. Since the electrons are drifting perpendicular to the magnetic field they experience a force which gives them a radial component of velocity (figure 4.15). In Ar:C_2H_6 50:50 gas, the Lorentz angle is approximately 45° so the correction can be as large as 5 cm. This correction can only be applied to the coordinates once the pattern recognition has resolved on which side of the wire plane the track passed and measured the drift distance.

It can also be seen from figure 4.15 that ionization created in two regions of the chamber which have been shaded will drift into the end walls of the wedge and not be collected on the anode.

4.5 Random Charge Division Errors

The principal cause of random charge division errors is electrical noise. If all the electrical noise were eliminated there would still be small random errors due to the digitization noise of the FADCs (figure 2.11) and due to the effect that the precise start time of the integrations have on the measured charge (figure 3.9). During the tests at CERN the rms level of electrical noise was high – equivalent to 6 re-linearized FADC units. There are two reasons for this:

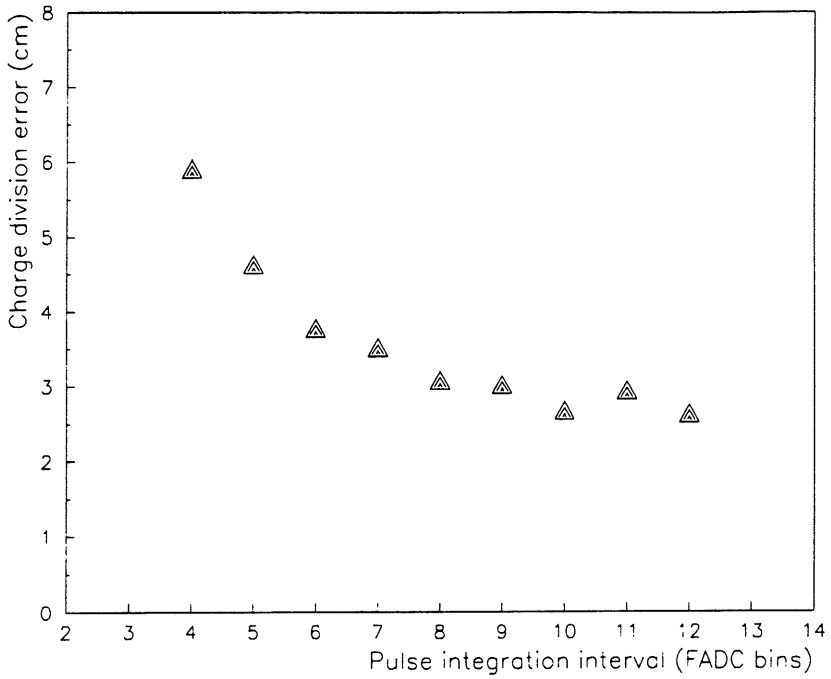

Figure 4.16: Charge division coordinate precision as a function of pulse integration time.

- The high voltage supply was not isolated from ground as it is at H1 (section 2.3.1) causing earth loops which are a common source of noise.
- In H1, the cryostat and the aluminium FTD tank act as a RF shield for RWDCs. Without this shielding the wires in the RWDC are susceptible to RF pick up.

The effect of noise is made worse if very short integration times are used. Figure 4.16 shows the precision of the charge division measurement plotted against the integration time. The maximum length of pulses in the raw data blocks from the tests at CERN is $\sim$ 12 FADC bins so it is not possible to integrate for longer time intervals than that.

To achieve the best possible precision, isolated pulses are integrated over the full 12 FADC bins. In the event of the start of a second pulse occurring before this time is up integration is truncated to the bin before the start of the second pulse.

4.6 Summary

A summary of the corrections to the drift and charge division coordinates measured using data from the test beam at CERN is given in table 4.4.

	Correction	Magnitude
Drift coordinate	Track angle effects	systematic $\leq 250\ \mu$m
	Cross talk	systematic $\leq 230\mu$m
	Incorrect wire t_0	systematic 17 μm
	Geometrical errors	systematic 38 μm
	Timing errors	random $\approx 200\ \mu$m
Charge division	Inherent non-linearity	systematic ≤ 8 cm
	Noise	random ≈ 3 cm

Table 4.4: Summary of the magnitudes of drift chamber space point errors investigated at CERN.

The greatest problem in the measurement of the drift coordinate in the RWDCs is the accurate (0.2 %) determination of drift velocity. A number of possible techniques have been discussed though as yet there is little data to give strong preference for any one of them. The second problem, in order of importance, is the determination of the global time reference Gt_0 for the FADCs. It has been shown that measurement of Gt_0 is closely connected with a correction which has to be made for the track angle. The track angle correction can be based on a simple model of electron drift in the RWDCs and gives values of Gt_0 which are consistent to within 0.1 ns for tracks angled between 0° and 30° to the wire plane. These measurements were made for tracks which had undergone the parametric cross talk compensation described in section 3.7.2, which can affect drift times by up to 4 ns. These results are therefore further evidence in favor of the parametric cross talk compensation described in section 3.7.2.

The measurements of random drift coordinate errors are consistent with those from tests of prototype chambers [25]. In a magnetic field, where electrons are no longer drifting directly toward the anodes, drift times are increased which leads to a lower *effective* drift velocity. This should reduce the effect of the timing resolution of the FADCs, giving an improvement in accuracy. This is not however the case if the drift

errors are dominated by diffusion (as for Xenon based gas mixtures).

The charge division coordinate is effected by a large systematic shift which varies both with radius and the pulse integration time. If the charge division were measured over a single wire rather than a pair of wires as is done in the RWDCs, at the center of the wire the shift would be zero since at this point the impedance in both directions would be the same. At the center of a 'wire' in the RWDCs two individual wires are connected at the chamber hub. At this point the systematic error is large (between 2 and 8 cm depending on the integration time). It is therefore clear that the shapes of the pulses change or the pulses are attenuated as they pass through the hub connections. The systematic error has been measured and a simple polynomial fit (which does however vary for each integration time) can be used to correct for it during track reconstruction. One advantage of this shift is that close to the hub the initial reconstructed points are always too far from the hub which means that space points are less likely to be 'found' in the wrong wedge.

Despite the complications of having pairs of wires connected at the hub, the charge division measurement from the tests at CERN is accurate to 2 % of the total wire length. To exploit the full dynamic range of the FADCs the noise levels should be reduced to below 1 re-linearized FADC unit. If this is achieved at H1 then the radial coordinate measurement should improve to $\sim$1 %, of a wire length as has been achieved in earlier tests.

Chapter 5

Simulation of Drift Chamber Pulses

5.1 Introduction

The principal motivation for this work was to understand the origins of the systematic and random charge division errors shown in sections 4.4 and 4.5. If the RWDC anodes acted as a simple current divider (figure 5.1) the charge collected at each end would be in inverse proportion to the resistance to ground at each end and the correction to the charge division coordinate $\Psi(r)$ in equation 3.7 would not be required. It is shown in section 5.2 that only $\sim \frac{1}{3}$ of the charge from a pulse is collected in a realistic integration time of 12 FADC bins. For a simple current divider this would not affect the reconstructed coordinate since the same fraction of the charge from each end would be collected in any case. The principal result from the model of the charge dividing mechanism presented here is that, due to the capacitance and inductance of the anodes and the connections between the pairs of anodes at the chamber hub, the shapes of the pulses emerging from each end are different, i.e. the ratio of the two pulse heights at a given moment in time changes. The ratio of the two integrated charges is therefore a function of the integration time which results in the large deviations from the simple model of charge division shown in figure 4.13.

The model splits into two main parts. The first is a description of how charge from

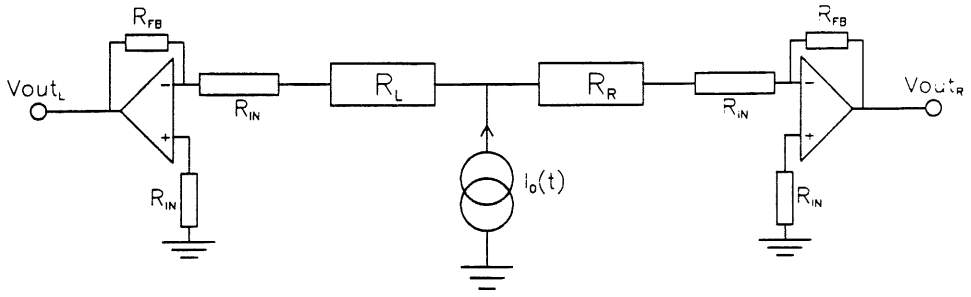

Figure 5.1: Simple model circuit of charge division.

a track passing through a chamber arrives at the surface of the anode and how this charge moves onto the anode as a function of time. This leads to an equivalent current source for the chamber. The second is a description of an equivalent electrical circuit used to model the way that current divides between the two ends of the anodes in a RWDC.

Section 5.4 describes how a Monte Carlo approach which combines the equivalent current source and the equivalent circuit response is used to simulate RWDC pulses. Simulated pulses were analyzed in the same way as RWDC test beam data to study the different types of point precision error in the RWDCs.

5.2 Equivalent Current Source for a RWDC

The current induced on an anode wire is subject firstly to the arrival of charge at the anode surface as a function of time and secondly to how the charge, once it is at the surface of the anode, moves onto the wire before dividing between the two ends. A charged particle passing through the chamber will generally create ~100 electron-ion pairs at random across each drift cell. What is calculated here is therefore a probability distribution of electron arrival times. During the simulation of pulses the probability distribution in figure 5.2 (see later) is not used but 'electrons' are scattered at random along the path of a 'track'. Depending on the position of the 'electron' in the simulated drift cell and on a random amount of diffusion the arrival time of each 'electron' is calculated independently and the final pulse in the Monte Carlo simulation is made up from the sum of that calculated for each individual 'electron'.

5.2.1 The Arrival of Electrons at an Anode Wire

The factors controlling the arrival time of individual electrons at the surface of an anode are:

- The different drift distances travelled by electrons produced at different points along the particle trajectory due to the geometry of the drift cell.
- The random diffusion of electrons within the charge cloud.

5.2.1.1 Variation of drift distance with z

It was described in section 4.2.2 how electron drift in a RWDC may be approximated by linear drift towards the wire plane followed by radial drift towards the anodes once the electrons are within a distance R_D of the anodes (figure 4.5). Since the time taken to traverse the radial region surrounding the wire is constant for any starting coordinate, the time of arrival of electrons may be calculated as the time taken to reach the boundary of the radial drift region.

The arrival time t of an electron originating from a position z ($-a < z < a$) along a track relative to that of an electron drifting along the center of the cell is then given by

$$t = \frac{R_D}{a} \frac{\left(a - \sqrt{a^2 - z^2} + z \tan \vartheta\right)}{V_d} \tag{5.1}$$

where ϑ is the angle of the track to the wire plane, and V_d is the electron drift velocity (refer to figure 4.4 for a definition of the coordinates). From the measurements of the global drift time origin of angled tracks (Gt_0) in section 4.2.2, R_D = 0.4 cm. This measurement comes from the analysis of tracks at angles of up to 30° and therefore may not apply beyond a distance $\pm\frac{a}{2}$ in z from the anode. If it is assumed that the relationship *does* apply to the whole of the drift cell, then (in the case $\vartheta = 0$ and assuming uniform distribution of charge accross the drift cell) it is possible to calculate the rate of arrival of electrons at the anode by differentiating equation 5.1:

$$\frac{dN}{dt} = \frac{N}{R_D} \frac{t_d - t}{\sqrt{t\,(2t_d - t)}} V_d \tag{5.2}$$

where t_d is the maximum difference in arrival times given by $t_d = \frac{R_D}{V_d}$ and N is the total number of electrons.

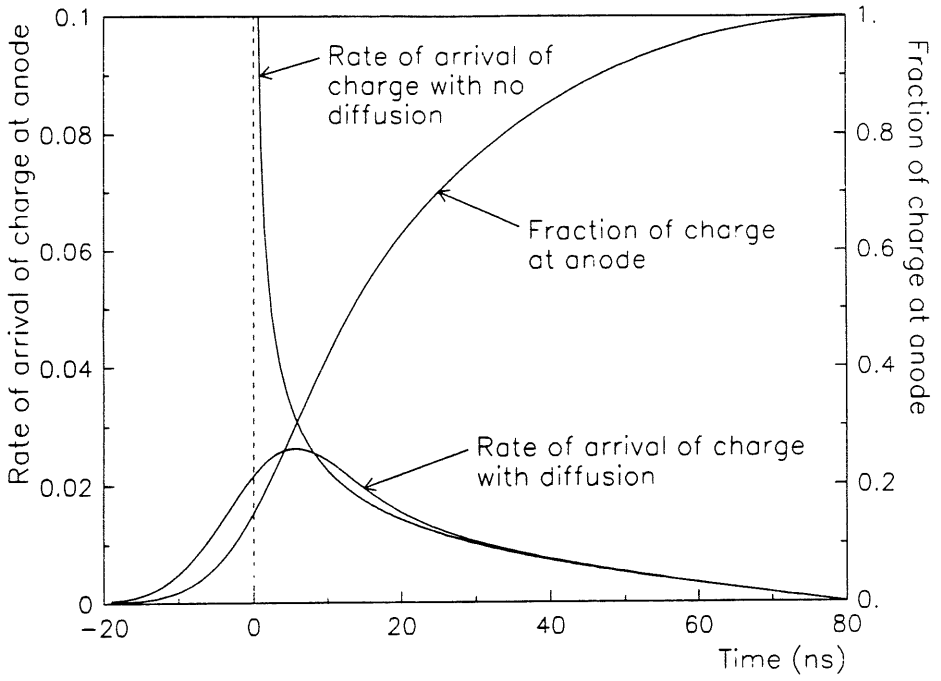

Figure 5.2: Rate of arrival of electrons at an anode wire, for a typical drift velocity of 50 μm/ns, both with and without electron diffusion. (The time origin is the arrival time of the first electron in the absence of diffusion.)

5.2.1.2 Electron Diffusion

Due to diffusion of the drifting electrons caused by multiple collisions with gas molecules. the distribution of charge about the center of a charge cloud is given by [35]

$$\frac{dN}{N} = \frac{1}{\sqrt{4\pi Dt}} e^{-x^2/4Dt}\, dx \tag{5.3}$$

where $\frac{dN}{N}$ is the fraction of electrons in an element dx a distance x from the center of the charge cloud at a time t, and D is the diffusion coefficient for the gas. The spatial distribution of charge around the origin is therefore gaussian with a standard deviation of

$$\sigma_x = \sqrt{2Dt} \ . \tag{5.4}$$

The resulting distribution in the arrival time of individual electrons at the anode leads to changes in the slope of the leading edge of drift chamber pulses, the leading edge rising more slowly as the drift distance (and hence t) is increased. In practice diffusion is in both the longitudinal (i.e. parallel to the electric field) and transverse (i.e. perpendicular to the electric field) directions. Since electrons accelerate in the longitudinal

direction between collisions with gas molecules the diffusion coefficient in each direction is generally different. For the purposes of simulating pulses, only longitudinal diffusion is included since the effect of transverse diffusion of the final arrival time of individual electrons will be small.

The probability distribution of arrival times of electrons at the anode can then be calculated from a time convolution of equations 5.2 and 5.3. Using a longitudinal diffusion coefficient $\sigma_x = 0.035$ cm [35] and nominal RWDC geometry the results of the convolution are shown in figure 5.2.

5.2.2 The Current Induced on an Anode Wire by a Charge

As explained in section 2.2.2, most of the electrons collected on an anode wire are not primary ionization caused by a charged particle passing through the chamber but are the product of avalanche gas gain close to the anode created when the primary electrons drift into the region of high electric field close to the anode surface. Therefore, at the moment of arrival of electrons on an anode wire, there is an equal and opposite charge surrounding the anode due to the positive ions created during the avalanche process. Since the total charge in the region is effectively zero, there will be no movement of electrons on the anode until the positive ions have begun to migrate away from the anode surface.

The following equations describe how the positive ions move through the electric field in the chamber and hence the mirror current induced by a charge e on the anode: The velocity of positive ions is given by (ignoring pressure changes):

$$\frac{dr}{dt} = \mu^{+} E(r) \quad . \tag{5.5}$$

For each ion starting at the anode surface which is at a potential V_s the work done dW in moving a distance dr is

$$dW = V_s i(t) dt = e \frac{dV}{dr} dr = eE(r) dr \tag{5.6}$$

so

$$\frac{dQ}{dr} = \frac{eE(r)}{V_s} \quad . \tag{5.7}$$

Therefore the current i moving on the anode is

$$i = \frac{dQ}{dt} = \frac{\mu^+ e}{V_s}[E(r)]^2 \tag{5.8}$$

where $E(r)$ is the electric field at a distance r from the center of the wire, μ^+ is the mobility of positive ions, and V_s is the electric potential at the surface of the anode.

In order to solve equation 5.8 it is first necessary to integrate equation 5.5 to get the radial position of the ions as a function of time:

$$t = \frac{1}{\mu^+}\int_{r_s}^{r} \frac{dr}{E(r)} \quad . \tag{5.9}$$

Due to the dependance of this equation on $E(r)$ a good understanding of the electric field in the region close to the anode is necessary.

Equations 2.1 and 2.2 in section 2.2.2 describe the electric potential in a RWDC. They may be differentiated to give the electric field

$$\underline{E}(x,z) = \frac{1}{2}[r_s E_s \nabla U(x,z) + E_g \nabla U(x,z-a)] \tag{5.10}$$

where

$$\nabla U(x,z) = \frac{\left(\frac{\pi}{2a}\right)}{\sinh^2\left(\frac{\pi x}{2a}\right) + \sin^2\left(\frac{\pi z}{2a}\right)}\left[\underline{i}\sinh\left(\frac{\pi x}{a}\right) + \underline{k}\sin\left(\frac{\pi z}{a}\right)\right] \tag{5.11}$$

where $\underline{i}$ and $\underline{k}$ are unit vectors in the directions of the x and z axis (refer to figure 2.3).

Substitution of equation 5.11 into equation 5.9 would lead to an integration which could only be done numerically, which is neither practical for use in the simulation of pulses nor helpful in gaining an understanding of the physics of the chamber. Also, it would be necessary to calculate the distribution of the paths taken by the positive ions in the directions $\underline{i}$ and $\underline{k}$.

Fortunately, at small distances from the anode (where $r \ll a$), equation 5.11 simplifies to

$$\underline{E}(x,z) = \frac{E_s r_s}{x^2+z^2}[\underline{i}x + \underline{k}z] \quad . \tag{5.12}$$

This is radially symmetric in all directions from the anode wire and simplifies still further to

$$E(r) = E_s\left(\frac{r_s}{r}\right) \quad . \tag{5.13}$$

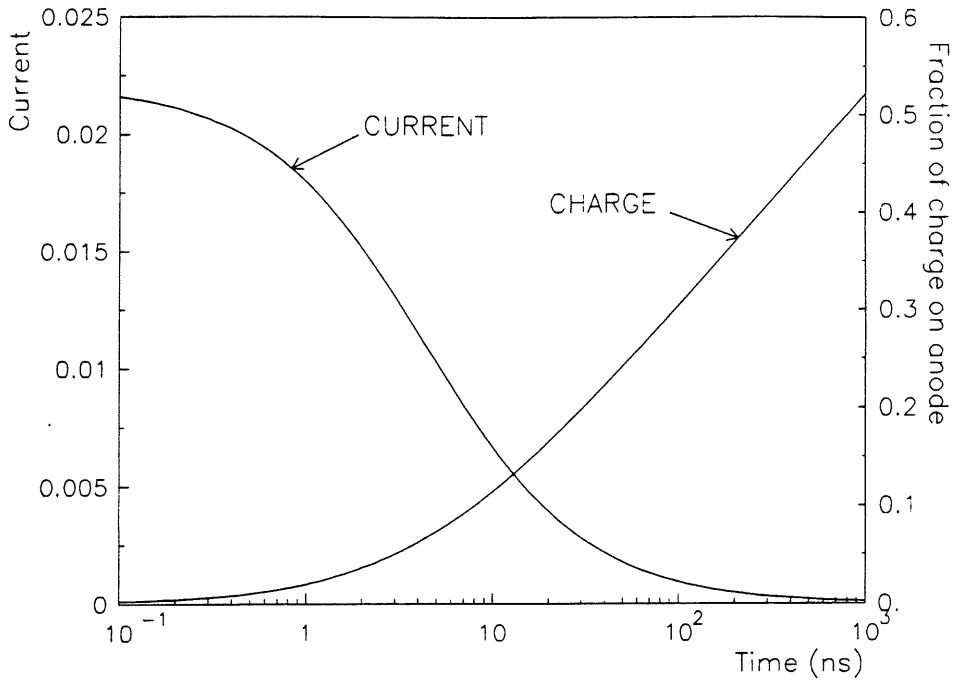

Figure 5.3: Induced current on an anode wire for unit charge and typical RWDC operating conditions.

This can be easily substituted into equation 5.9 and integrated to give

$$t = \frac{1}{\mu^+ E_s r_s} \int_{r_s}^{r} r\, dr = \frac{r_s}{2\mu^+ E_s} \left(\frac{r^2}{r_s^2} - 1 \right) \tag{5.14}$$

which is then used in equation 5.8 to give the current $i(t)$:

$$i(t) = \frac{\mu^+ e E_s^2}{V_s} \left(\frac{1}{1 + \frac{t}{t_0}} \right) \tag{5.15}$$

where

$$t_0 = \frac{r_s}{2\mu^+ E_s} \,. \tag{5.16}$$

It is now possible, using values for μ^+, E_s and V_s which are typical for the field configurations and gases used in the RWDC ($\mu^+ = 1.7 \times 10^{-4} \mathrm{m}^2/\mathrm{V/s}^\dagger$, $E_s = 170 \mathrm{kV/cm}$, and $V_s = 2228\,\mathrm{V}$) to calculate the distance r travelled by the positive ions in time t. The maximum integration time used for the analysis of the CERN test data and data from the RWDCs in H1 is 120 ns, during which time the ions would have moved 134 μm. Even after 1 μs they would only have moved 380 μm, which satisfies the condition of

† This value of μ^+ was quoted in an internal note of the ZEUS experiment [36] obtained by interpolation between data for CH_4 in Ar and C_4H_{10} in Ar taken from [35].

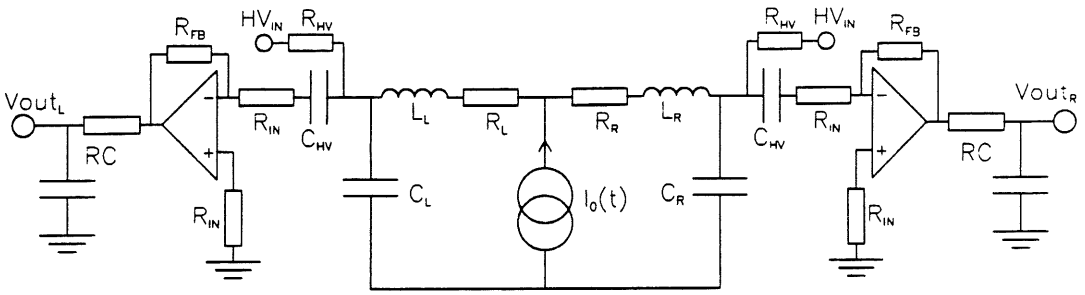

Figure 5.4: Equivalent RWDC circuit including resistance, capacitance and inductance of the anode, the HV supply and the amplifier rise time

being small compared to the 5 mm spacing between anode and field wires and validates the assumptions made in equation 5.13.

Both the current and the total charge collected (obtained by integrating equation 5.15) as a function of time are shown in figure 5.3. It can be seen that over a typical charge integration time of 120 ns, well under 40 % of the total charge is collected. It is also clear that after the first microsecond, although only slightly over 50 % of the charge is on the wire, the current has dropped almost to zero. The remaining charge moves onto the wire slowly over a relatively long period of time as the positive ions move more slowly in the low field regions away from the anode wires.

5.3 Impulse Response of an Equivalent RWDC Circuit

The equivalent circuit used to model pulse formation in a RWDC is shown in figure 5.4. The impedance of the anode wire on each side of the hit position is represented by a capacitor ($C_{L,R}$), an inductor ($L_{L,R}$) and a resistor ($R_{L,R}$). The calculation of $C_{L,R}$, $L_{L,R}$ and $R_{L,R}$ is discussed in appendix B.1 where it is also shown that that the capacitance and inductance are approximately uniformly distributed along the length of the anodes. In the simulation, capacitance and inductance are therefore divided between the two ends of the circuit in the same way as resistance. The resistance of the hub is negligible ($< 0.1\,\Omega$) but there is additional capacitance of $\sim$ 16.5 pF and inductance of $\sim$ 0.2 nH seen by pulses propagating through the hub. For a hit at a distance r from the hub in the Left hand wedge which has a total length L the values

R_W	447 Ω	Resistance of a single anode
C_W	17 pF	Capacitance of a single anode
C_H	16.5 pF	Capacitance of hub connection
L_W	1.2 μH	Inductance of a single anode
L_H	0.2 μH	Inductance of hub connection
R_{HV}	1.0 MΩ	High voltage feed resistor
R_{IN}	200 Ω	Preamplifier input resistance
RC	7.3 ns	Output filter decay constant

Table 5.1: Values of components used in the equivalent RWDC circuit.

of the components used in the model are:

$$\begin{aligned} R_L &= (1 - \tfrac{r}{L})R_W \\ R_R &= (1 + \tfrac{r}{L})R_W \\ C_L &= (1 - \tfrac{r}{L})C_W \\ C_R &= (1 + \tfrac{r}{L})C_W + C_H \\ L_L &= (1 - \tfrac{r}{L})L_W \\ L_R &= (1 + \tfrac{r}{L})L_W + L_H \end{aligned} \tag{5.17}$$

where R_W, C_W, C_H, L_W and L_H are the resistance and capacitance of a single anode wire, the hub capacitance and the inductance of a single wedge and of the hub connector respectively.

The amplifier input (described in section 2.3.3) is represented by the high voltage feed resistor R_{HV}, the decoupling capacitor C_{HV} and the input resistor to the operational amplifier R_{IN}. The most important feature of the preamplifier response, and the only one which is included, is its rise time which is represented by a simple RC integrator on the output of an ideal[‡] operational amplifier. The value of RC is selected to give a 10 % to 90 % rise time for square pulses of 16 ns, 10 ns of which comes from the preamplifier and 6 ns from capacitance effects in the long signal cables [19]. The

[‡] An ideal operational amplifier has infinite input impedance, zero output impedance, infinite gain, and infinite bandwidth.

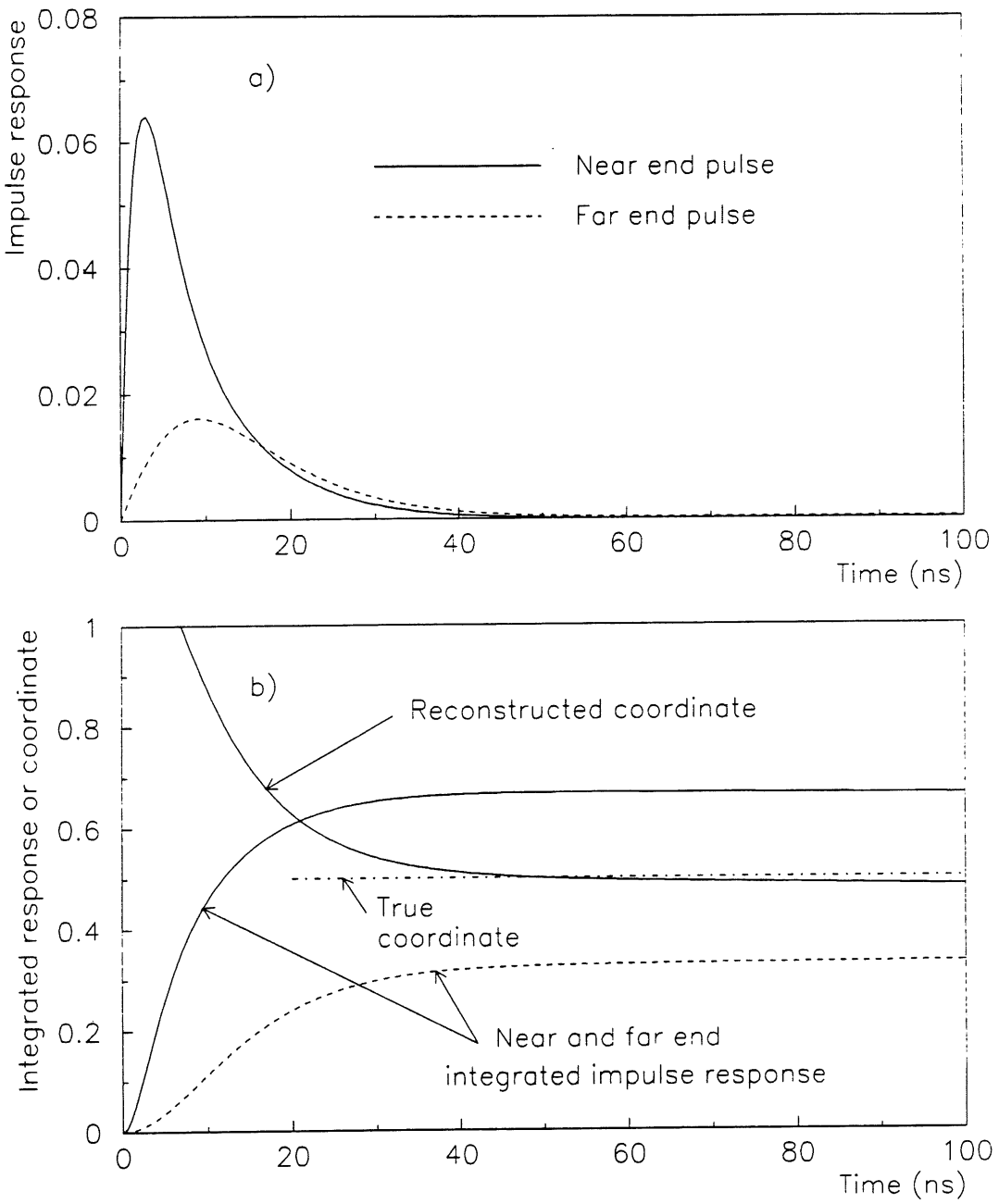

Figure 5.5: a) Computed impulse response for a RWDC with the impact position half way along one wedge, b) Integrated impulse responses and the resulting reconstructed radial coordinate.

values of all of the components used in the simulation are summarized in table 5.1[§].

Once the values of the circuit components have been selected, the circuit frequency response is calculated as a function of s (where $s = j\omega$). For a single input current $I(\omega)$ there arise two output voltages $Vout_L(\omega)$ and $Vout_R(\omega)$, one for each end of the circuit. The details of this calculation are given in appendix B.2. The two impulse responses (i.e. the output from each end of the circuit in response to an input current which is the Dirac δ-function) are calculated by taking the inverse Laplace transforms of the complex frequency responses [37]. The two impulse responses both turn out to be the sum of 8 exponential decays (appendix B.3).

$$Vout\,(t) = \sum_{i=1}^{8} F_i e^{-\alpha_i t} \tag{5.18}$$

where the coefficients F_i and α_i are different for the two ends of the wire. Depending on the relative values of $R_{L,R}$, $L_{L,R}$ and $C_{L,R}$ it is possible for F_i and α_i to be complex. If this is the case, the solutions contain oscillating as well as exponentially decaying terms in a similar way to solutions to the damped harmonic oscillator equation.

The impulse response of the model RWDC for a chamber hit half way along one wedge (i.e. $\frac{3}{4}$ of the way along a total wire length) is shown in figure 5.5.a. Figure 5.5.b shows the integrated impulse responses of the two ends of the wire as a function of time and the reconstructed radial coordinate $\frac{r}{L}$ using

$$\frac{r}{L} = \frac{L_{eff}}{L}\frac{Q_L - Q_R}{Q_L + Q_R} \tag{5.19}$$

where Q_L and Q_R are the integrated impulse responses from the two ends, L is the length of the wire and $\frac{L_{eff}}{L}$ is defined in section 3.5 on page 60. It can be seen that the reconstructed coordinate varies with integration time, particularly if that time is small (< 50 ns). It can also be seen that the widths of the pulses derived from a δ-function are small compared with the arrival time of electrons at the anode surface, and the time constant of the currents induced on an anode by each electron. The true error on a reconstructed radial coordinate may only be evaluated when these have both been taken into account.

[§] The preamplifier feedback resistance is not included in the table since it is not directly used in the calculation but is replaced by the gain of the preamplifiers which is 105 mV/μA.

5.4 Monte Carlo Simulation of Flash Digitized RWDC Pulses

There are a number of random processes envolved in the generation of drift chamber pulses which need to be accounted for in the simulation. This is done as follows:

1. The number of primary ion pairs produced by a charged particle traversing a drift cell is random and is generally parameterised by a Landau like distribution [35]. In the simulation the coordinates of a random number of electrons are generated (typically about 100) at random along the length of the track.

2. For each electron the nominal drift time to the anode is calculated using equation 5.1. From this drift time the probable error due to diffusion in the position of the particle can then be calculated from equation 5.4 and an extra time added (or subtracted) at random to each of the above times using equation 5.3.

3. The time delay for the signals from each individual electron to travel to the preamplifiers is then calculated using a propagation speed of 1.4×10^8 m/s (appendix B.1.3).

4. To make the simulation of the flash digitization realistic the start time of the FADCs for each pulse is made random. Pulses simulated at the same drift distance in the chamber would otherwise all have precisely the same start time which would be both un-realistic and would cause problems during analysis since the software has been designed specifically for a random distribution of start times across a FADC bin (section 3.4). The FADC start time is kept in the output for each simulated pulse to enable studies of drift timing effects.

5. For each FADC bin at each end of the circuit it is therefore possible to calculate the relative arrival time of a pulse from each individual electron. The ouput voltage $V(t)$ at each end is calculated by convoluting equation 5.15 (i.e. the current from 1 electron) with the chamber impulse response (equation 5.18) for

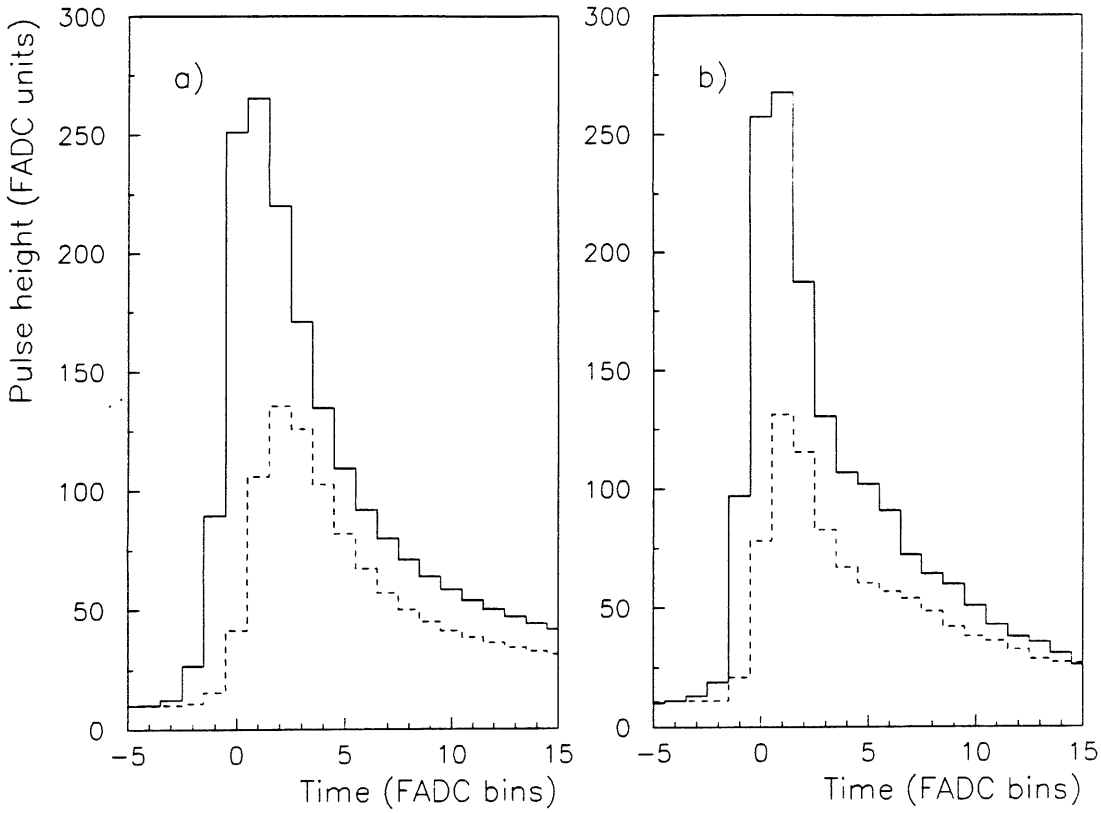

Figure 5.6: a) Average of 1000 simulated RWDC pulses at an impact position half way along one wedge. b) Average of $\sim$ 1000 RWDC pulses from a 50 GeV e^- beam at the same point in a RWDC wedge.

each end of the chamber:

$$Vout(t) = V_i(t) * i(t) = \int_0^t V_i(r) i(t-r) dr \tag{5.20}$$

where t is the time that has elapsed between the arrival of the start of the pulse at the wire end and the time of the FADC bin under consideration, $V_i(t)$ is the impulse response (equation 5.18) and $i(t)$ is the current.

6. This process is repeated for every electron generated in step 1 above, the results from each electron being added together to generate a complete pair of RWDC pulses.

7. To study the effects of electrical noise, numbers generated at random in a gaussian distribution may be added to the contents of each 'FADC bin'.

8. The final step in the simulation is to de-linearise the generated pulses using a look-up table which is the inverse of that used to re-linearise real data described in section 2.3.4. (In the H1 FADC crates this is actually done by means of a non-linear amplifier immediately preceding each FADC.)

9. The generated pulses are then written to disk in the same format as real data so that they may be easily analyzed using the same software packages.

The average of 1000 simulated pulses is shown in figure 5.6.a. For comparison the average of 1000 RWDC pulses from a 50 GeV e^- beam (without transition radiator) at the same point in a RWDC wedge is shown in figure 5.6.b.

5.5 Simulated Radial Coordinate Errors

5.5.1 Random Radial Coordinate Errors

Pulses of a similar height to those observed in the tests at CERN were generated with different levels of random noise. Figure 5.7 shows the rms variation of the reconstructed coordinates of 500 such pulses as a function of the level of the noise and the pulse integration time. Also shown are the results from the CERN test beam studies already presented in figure 4.16. Measurements of the variation in the pedestal regions preceeding RWDC pulses indicate a noise level in the tests at CERN of $\sim$ 0.6 % of the FADC full scale (fsd).

It is clear from a comparison of the radial coordinate errors observed in the test beam and those simulated with a similar level of 'noise' that the simulation is reasonably good at reproducing both the absolute levels of error and the variation with integration time. It appears from the simulation that there is an absolute lower limit on the radial precision possible of $\sim$ 1 cm (0.7 % of the total wire length). There are two possible sources of this error:

1. The 'digitization noise' of the FADCs (discussed in section 2.3.4 on page 37). The level of this type of noise has been minimized through the use of non-linear FADCs which improves the signal to noise ratio at small signal levels. The only

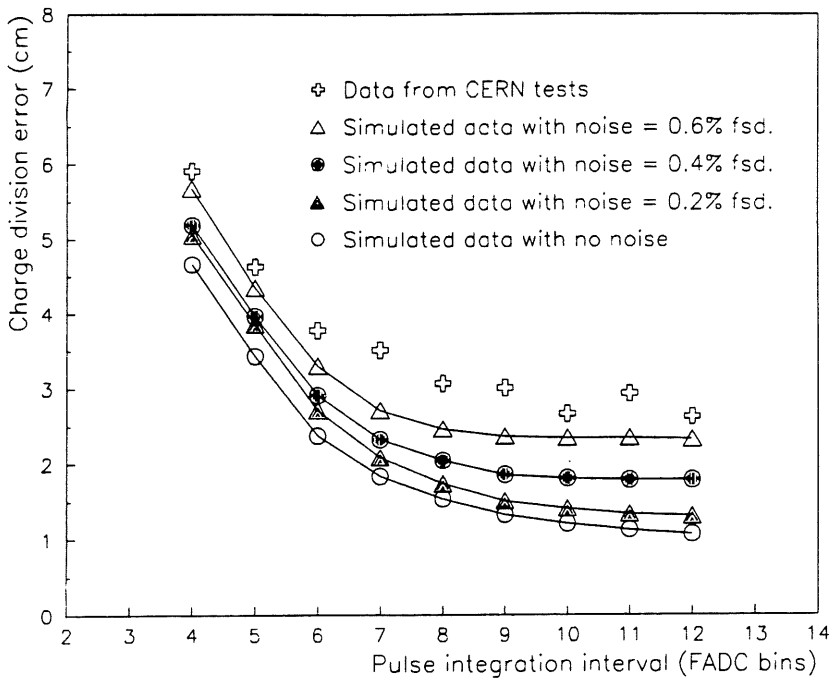

Figure 5.7: Simulated random charge division coordinate errors as a function of pulse integration time and the level of electrical noise. (The noise values are quoted as a percentage of the full scale of the FADCs.)

way to make further improvements would be to increase the number of bits used by each FADC.

2. The exact start time of the integration of each pulse. Due to the length of the wires in the RWDCs and the different start times of the FADCs at each end of a wire (section 3.5) the start time of the integration is determined separately for each end (section 3.4). The result of the integration is therefore dependent on the precision of the drift timing which is $\sim \frac{1}{3}$ of a FADC time bin for the total pulse but is less accurate for small pulses. This contribution to the error is likely to be largest over short integration times when the fractional error on the integrated charge will be most affected by the precise start time of the integration.

5.5.2 Systematic Radial Coordinate Errors

The simulation is less successful at quantitatively reproducing the large systematic errors described in section 4.4. It does however reproduce the main trends of the systematic error both with integration time and position on the wire (figure 5.8).

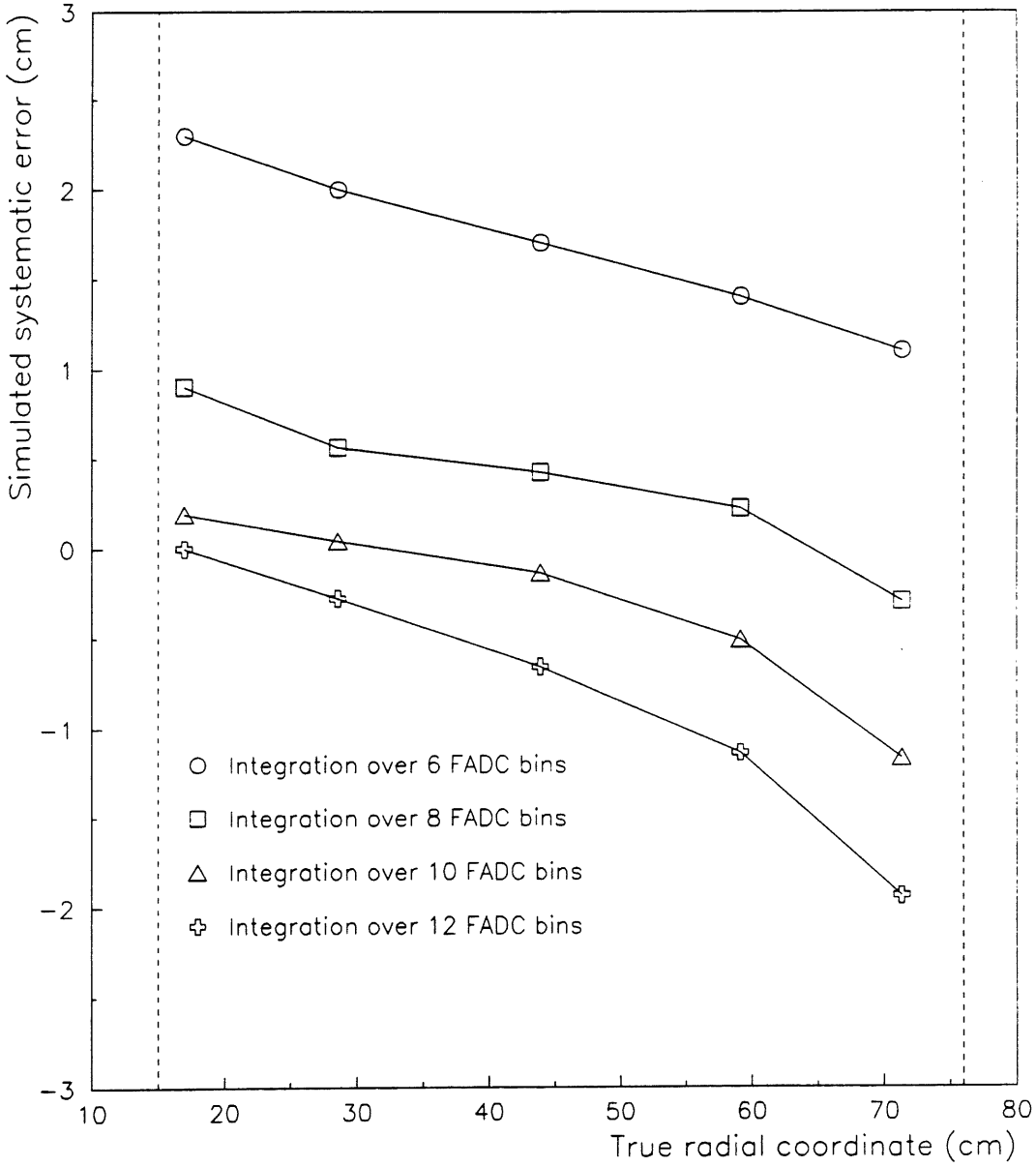

Figure 5.8: Simulated systematic radial coordinate error. The dashed lines mark the minimum and maximum sensitive radii of a RWDC.

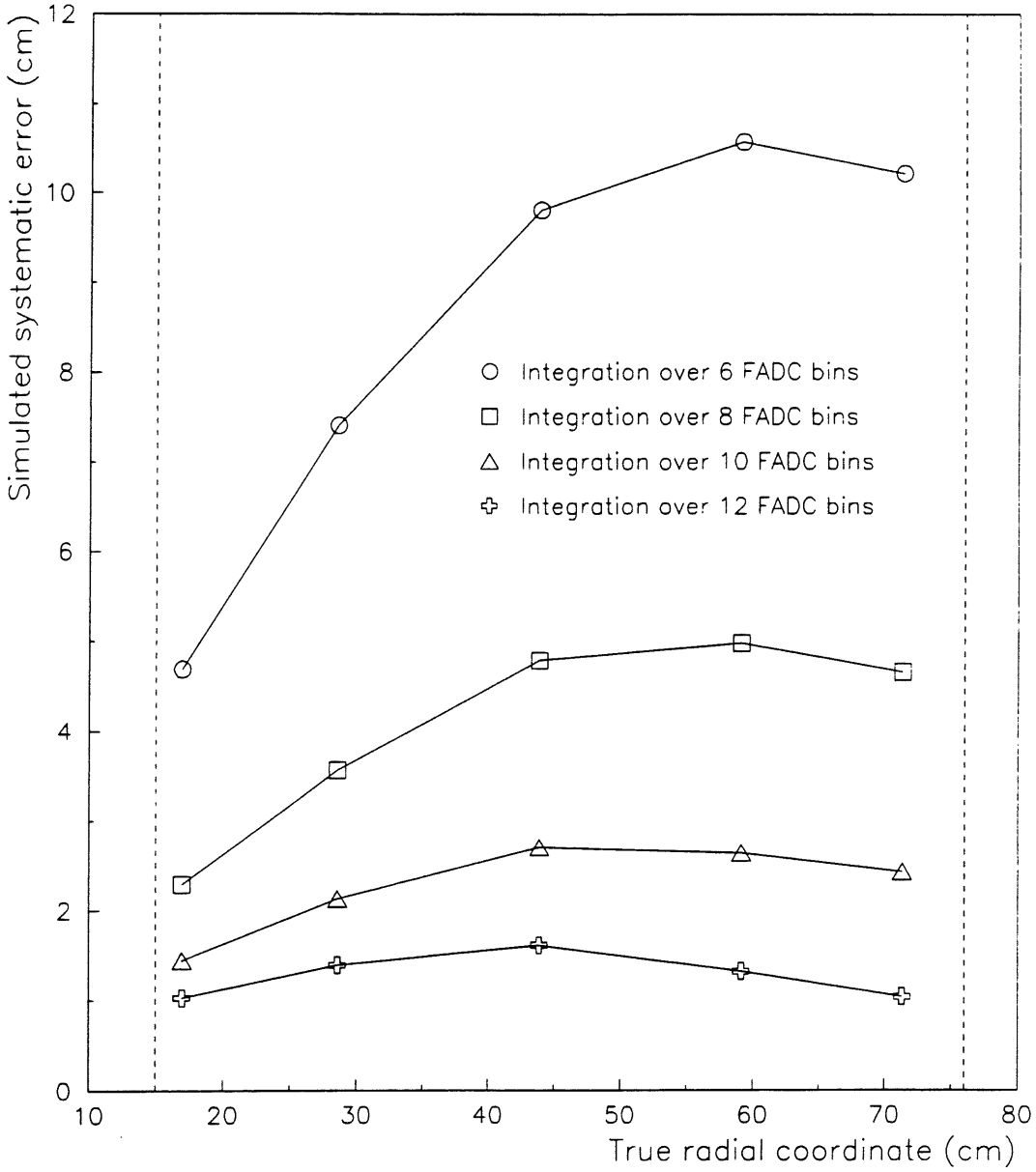

Figure 5.9: Simulated systematic radial coordinate error using a different charge integration method to that described in section 3.4. Integration of both pulses is started at the mean drift time of the two pulses.

With no hub capacitance or inductance the model produces no systematic shift at the center of the chamber so it is clear that the hub reactance is responsible for the large dependence on the reconstructed radial coordinate close to the hub on the integration time. The model also allows some insight into the effects of the QT code on the reconstructed coordinate. For example, if the same integration start time was used on both pulses[¶], the simulated systematic error changes to that shown in figure 5.9 which differs from the previous systematic error by up to 10 cm. Due to the differences in the FADC start times it is not possible to use this charge integration method with real chamber data.

5.6 Simulated Drift Coordinate Errors

Drift coordinate errors were studied using the simulated pulses in much the same way as the radial coordinate errors. Figure 5.10 shows the rms variation in the reconstructed drift coordinate as a function of drift distance in the absence of noise and with the same level of noise as observed in the CERN test data. No attempt was made to model the non-linearities in the drift field close to the wires so the characteristic loss of precision close to the wire plane is not observed. It is possible to parameterise this error in a similar way to that for real data (equation 4.8 in section 4.3) except that only two parameters are needed to describe the total error σ_d :

$$\sigma_d^2 = \sigma_1^2 + \sigma_2^2 d \quad . \tag{5.21}$$

σ_1 and σ_2 are summarized in table 5.2. σ_2, which is the result of electron diffusion is the same for both levels of noise and σ_1 is increased only slightly by the addition of noise.

In section 4.2.2 it was found that the very regular pulses produced by the trigger logic could be timed to an accuracy of ~ 0.2 ns which is an order of magnitude better than the 3 ns achieved with real chamber data or the 2 ns from the simulation. It seems therefore, that the random elements which go into making chamber pulses (section 5.4)

[¶] In this example the integration start time is taken as the unweighted mean of the individual start times of the two pulses.

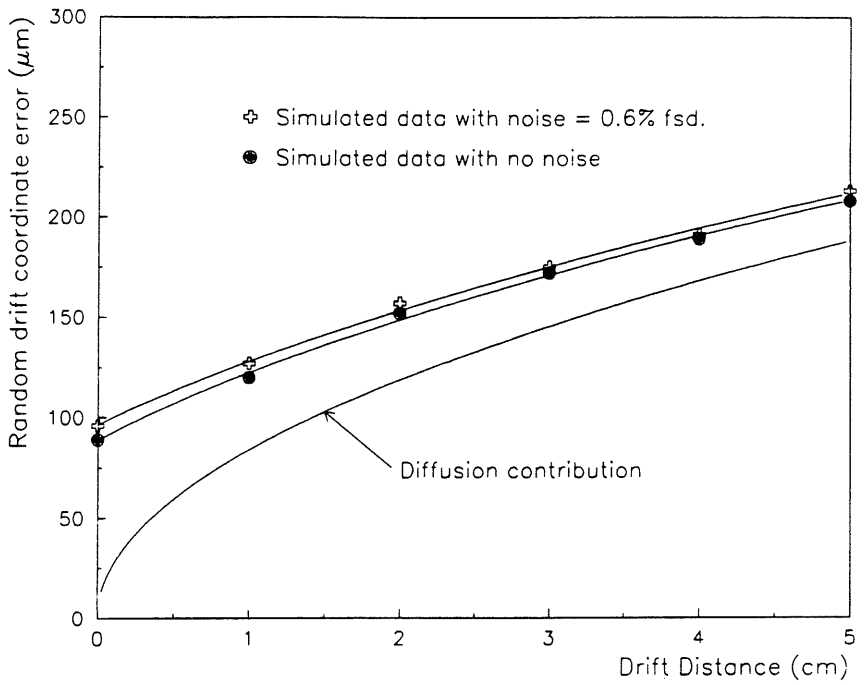

Figure 5.10: Simulated drift coordinate precision as a function of drift distance for a noise level comparable to that seen during tests and in the absence of noise.

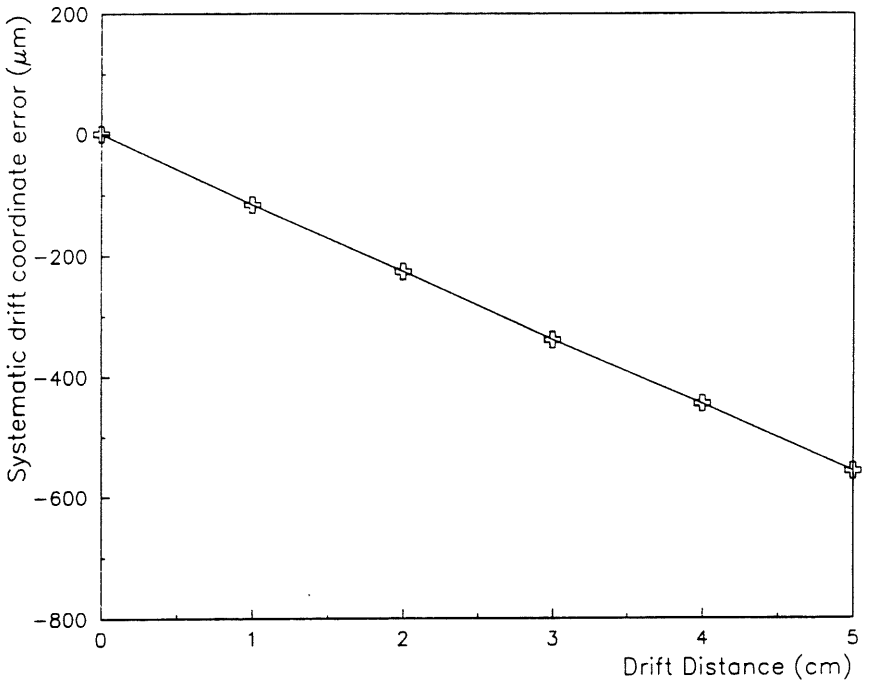

Figure 5.11: Simulated systematic drift coordinate error which results from using the same drift velocity in the generation of pulses as in their reconstruction.

	Drift errors	
Noise	σ_1 (μm)	σ_2 μm/$\sqrt{\text{cm}}$
None	89	84
0.6 % fsd.	96	84

Table 5.2: Contributions to the simulated drift coordinate space point errors.

are the principal contributors to the minimum timing resolution of chamber pulses possible with FADCs.

Also of interest is the systematic shift in the drift coordinates of reconstructed simulated pulses (figure 5.11) which exists even though exactly the same drift velocity was used in the reconstruction as in the simulation of the pulses. The drift velocity is the mean velocity of all the electrons in the charge cloud. Due to diffusion some electrons will reach the anodes before the nominal drift time as can be seen in figure 5.2. The timing method described in section 3.4 uses a projection of the leading edge of pulses onto the baseline. Clearly as the drift distance, and hence the amount of diffusion, increases the time at which this projection meets the baseline will come further in front of the arrival time of the center of the charge cloud resulting in shorter drift times and a systematic error in the reconstructed coordinate. From figure 5.11 this error is $\sim -110\,\mu$m/cm. This indicates that the 'drift velocity' used in the reconstruction needs to be 1.1 % larger than that used in the simulation of pulses.

No systematic error of this type was observed in the analysis of real chamber data since the drift velocity used in that analysis was measured directly by a comparison of known drift distances and the drift times measured from genuine pulses (section 3.6). The drift velocities shown for different gas mixtures in table 3.2 are therefore slightly larger than the true mean velocity of the clouds of drifting electrons. They are however still the correct values to use during track reconstruction.

5.7 Discussion and Conclusions

It was shown in section 5.2 that the shape of pulses in a drift chamber is determined by the geometry of the drift cells and by the electric field in the chamber.

- The geometry of the drift cell controls the arrival time of individual electrons at the anode surface.
- The electric field close to the anode determines the speed at which positive ions from the avalanche multiplication process move away from the anode, and hence the rate at which the electrons at the surface of the anode may move onto the wire and be collected at the preamplifiers.

The arrival time of electrons at the anode is spread over ~80 ns (figure 5.2). The positive ions produced during avalanche multiplication start off moving very fast in the high electric field but then slow down as they move away from the wire. The current from a charge already at the anode falls rapidly to half of its initial value in $\sim$ 5 ns. At this point, however, only about 10 % of the charge is on the wire and even after 1 μs only about half of the charge is collected.

The width of the impulse response of the RWDC equivalent circuit is comparable to that of the induced current from a charge already at the anode, both of which are considerably narrower than the arrival time distribution of the drifting electrons. To design a chamber with narrow pulses it would therefore be necessary to concentrate as much on the geometrical paths taken by drifting electrons as on reducing the capacitance of the chamber and hence the width of the impulse response.

Although unable to reproduce quantitatively the large systematic errors observed in charge division measurements from the RWDCs, the model does qualitatively reproduce the variations in the systematic error both with the charge integration time and with the coordinate along the length of the wire. At first sight, this result is contrary to that of V. Radeka and P. Rehak [38] who show that *under certain conditions* the amount of charge collected at each end of the anode is in simple inverse proportion to the resistance to ground and is essentially independent of the inductance and capacitance of the anode. This result only applies if *all* of the charge is collected at each end of

the wire and they show that this is most rapidly achieved when the total resistance of the anode $R = 2\pi\sqrt{L/C}$ where L and C are the inductance and the capacitance of the anode per unit length. The condition of total charge collection is impossible to satisfy in the RWDCs (and probably most other realistic drift chamber designs) since the arrival time of charge on the anode and the movement of that charge along the anode takes much longer than a realistic charge integration time of $\sim$ 120 ns.

The simulation of pulses also shows that the reconstructed charge division coordinate is extremely sensitive to the pulse timing and charge integration methods used. The only practical solution to these problems is an independent calibration of the charge division coordinate as was done using the CERN test beam and can be achieved in the H1 FTD using track segment information from the PWDC's. In fact, the H1 tracking detectors have been designed so that such a calibration may be performed by every sub-detector which uses charge division for coordinate determination. The CJC may calibrate its charge division coordinate (z) using the drift coordinates of the two z-chambers CIZ and COZ. Conversely the CIZ and COZ use charge division to measure ϕ and can therefore use the ϕ coordinates from the CJC for calibration. The forward muon system (which has a similar complication to the RWDCs in that the anodes in adjacent drift cells are linked at one end and charge division is used for coordinate determination in a pair of cells) contains modules where the drift measures θ and the charge division measures ϕ and modules where the drift measures ϕ and charge division measures θ. A cross calibration between the two types of module should be easily realized.

Section 5.6 showed that the measured 'drift velocities' in section 3.6 are not the true mean velocity of drifting electrons but are made artificially large due to the effects of electron diffusion. For track reconstruction it is this slightly large value of drift velocity which should be used. If a different timing algorithm were used which used information from the whole pulse rather than the leading edge alone, it is likely that this effect would become smaller or even disappear completely. This effect does not cause any problems if the drift velocity used for track reconstruction is measured in the RWDCs. If an independent drift velocity monitor were used however, the operating

conditions in the monitor and the pulse analysis techniques would have to be the same as those for the RWDCs if a realistic measurement of velocity were to be achieved.

Chapter 6

Transition Radiation Detection

6.1 Ionization Energy Loss Processes in Drift Chamber Gases

For a charged particle passing through a drift chamber gas, the dominant energy loss process is due to electromagnetic interactions between the particle and the atoms and molecules of the gas. The *mean* energy loss per unit length is reasonably described by the Bethe-Bloch formula [35] :

$$\frac{dE}{dx} = -\frac{2\pi N z^2 e^4}{mc^2}\frac{Z}{A}\frac{\rho}{\beta^2}\left\{\log\left(\frac{2mc^2\beta^2 E_M}{I^2(1-\beta^2)}\right) - 2\beta^2\right\} \tag{6.1}$$

where N is the Avogadro number, M and e the electron mass and charge. Z, A and ρ are the atomic number, atomic mass and density of the gas and I is its ionization potential. β and z are the velocity (in units of c) and charge of the ionizing particle. E_M is the maximum energy transfer possible at each projectile – gas molecule collision which is

$$E_M = \frac{2mc^2\beta^2}{1-\beta^2} \tag{6.2}$$

for simple two body relativistic kinematics. The actual energy loss is the result of a small number of interactions and is therefore subject to large statistical fluctuations as is clear from the distributions in figure 6.4.

It can be seen from equation 6.1 that the mean energy loss varies as a function of β and that it can be divided into four more or less distinct regions:

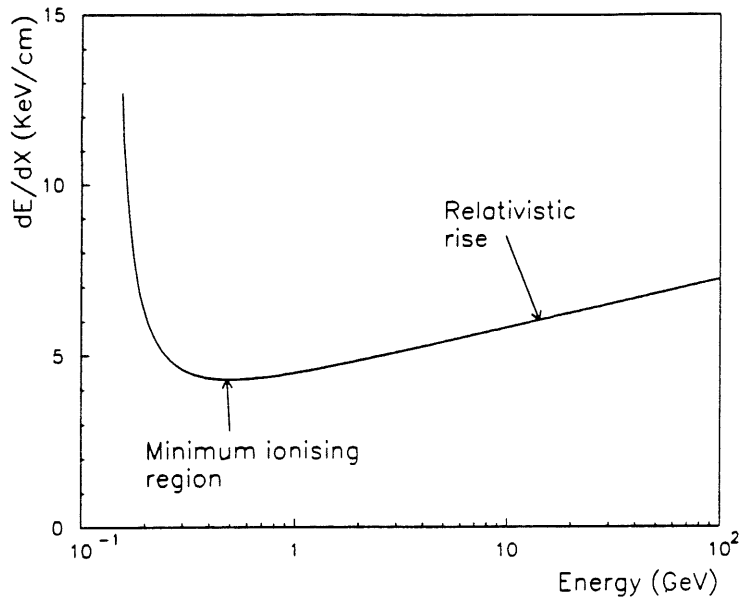

Figure 6.1: Calculated mean energy loss for a π^- in pure argon as a function of particle energy.

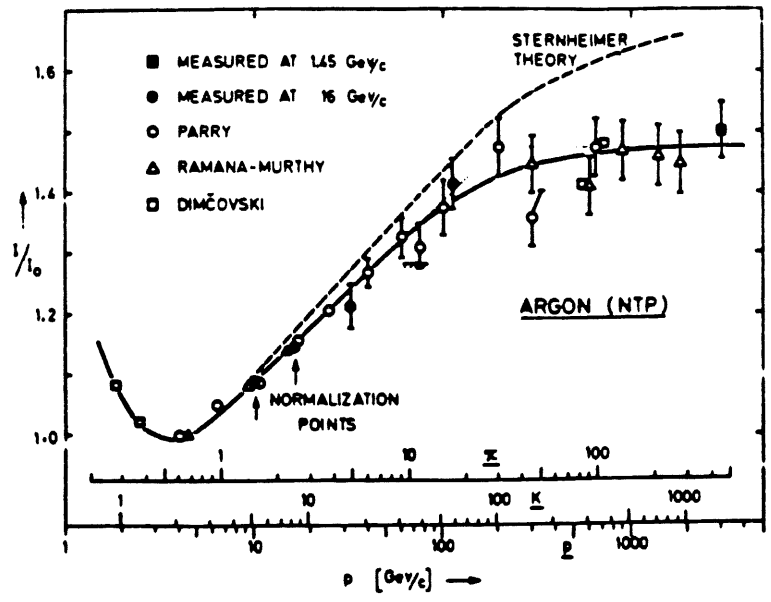

Figure 6.2: Relativistic rise of the energy loss in argon, as a function of particle mass and momentum; the vertical scale gives the relative increase above the minimum of ionization [35].

1. Due to the $\frac{1}{\beta^2}$ term there is a rapid reduction in the energy loss at low β.

2. At slightly higher β, the energy loss reaches a minimum value at $\beta \sim 0.97$, which is known as the 'minimum ionizing region'.

3. At $\beta > 0.97$, the $(1 - \beta^2)$ term causes what is known as the 'relativistic rise', the energy loss increasing logarithmically as $\beta \rightarrow 1$.

4. According to the Beth-Bloch formula above, this rise would continue indefinitely. However, when the energy loss reaches approximately 1.5 $\times$ its value in the minimum ionizing region, polarization effects in the chamber gas result in saturation and the level of ionization reaches a constant value.

The Bethe-Bloch expression for pions in pure argon at energies of up to 100 GeV is plotted in figure 6.1. Figure 6.2 shows the measured ionization energy loss from protons, kaons and pions showing clearly the plateau reached in the energy loss at high β.

Due to their low mass (and consequently high β) the energy loss of electrons above an energy of a few GeV is already in the plateau region. Figure 6.3 shows the truncated mean[†] energy loss over 3 test beam events of the ionization in the RWDC to reproduce the effect of tracks passing through all three super modules of the forward track detector. The error bars are the rms variation of the truncated mean and *not* the errors on the mean values. The figure shows clearly the constant level of dE/dx for electrons and the relativistic rise for pions.

6.1.1 δ-Ray Production

The electrons from ionization of the chamber gas may be ejected with any energy up to the maximum E_M (defined in equation 6.2). Electrons emitted with an energy of a few keV or more are capable of travelling up to a few mm in the chamber gas and are known as δ-rays. The energy of a δ-ray is rapidly lost in inelastic collisions, creating further ionization which results in a considerably larger pulse. δ- rays thus cause the long tail at high energy loss in energy loss distributions for charged particles (figure 6.4).

[†] The truncated mean is the mean of all except the largest pulse in each chamber. This has the effect of suppressing the long tail of the Landau distribution of ionization and results in narrower mean charge distributions than those shown in figure 6.5.

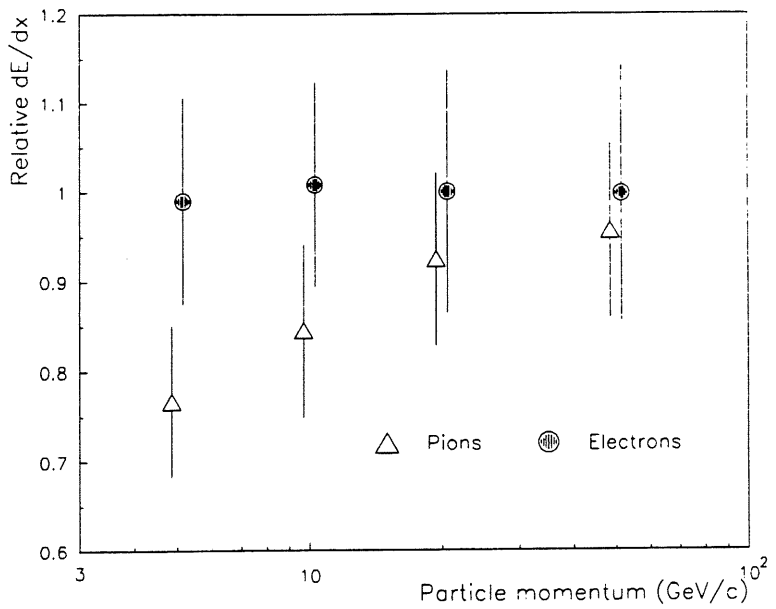

Figure 6.3: Truncated mean energy loss (dE/dx) for pions and electrons with no radiator in Xe:He:C_2H_6 30:40:30 gas mixture. The 'error bars' are the rms variation of the truncated mean dE/dx over 3 events and *not* the error on the mean.

The large pulses arising from δ-rays from pions passing through the chamber therefore form one of the main backgrounds affecting good TR discrimination between pions and electrons.

6.2 Transition Radiation

It is clear from figure 6.3 that above an energy of a few GeV, dE/dx alone is not sufficient to distinguish between pions and electrons in the RWDCs. The inclusion of transition radiating material immediately upstream of each RWDC produces additional ionization when electrons pass through the FTD giving a marked improvement in the e/π discrimination.

Transition radiation (TR) is produced when a relativistic charged particle crosses the boundary between two materials with different dielectric constants. The phenomena was first predicted by Ginzberg and Frank [39]. The energy is emitted in the form of an X-ray, with an emission angle which is very small ($\theta \simeq \frac{1}{\gamma}$ where γ is the Lorentz factor $= (1-\beta^2)^{-\frac{1}{2}}$) so the X-ray is detected along with the dE/dx of the particle as it passes through the chamber. The production of transition radiation is strongly dependent

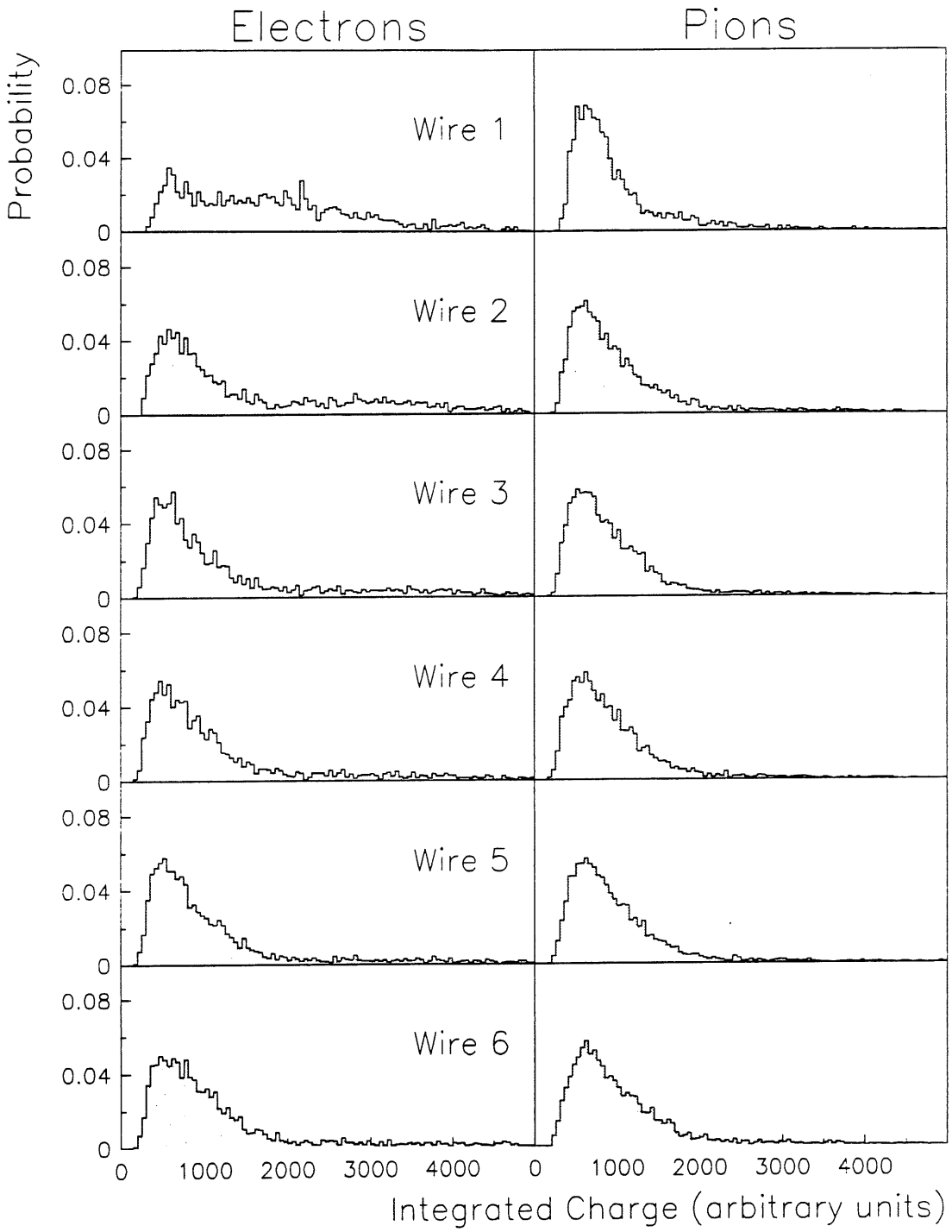

Figure 6.4: Integrated charge distribution for 5 GeV electrons and pions on the first 6 wires in a RWDC in Xe:He:C_2H_6 30:40:30 gas mixture. Only chamber hits accepted as part of a fitted track segment are included in the distributions.

on γ and will generally only be produced when electrons pass through the radiating material at particle momenta of up to ~100 GeV/c. At higher energies (>100 GeV) pions will also produce TR resulting in a reduction in the usefullness off TR as a means of electron identification.

The probability of producing a photon at each boundary is small ($\sim \alpha$) so the radiator in front of each RWDC consists of 400 polypropylene foils each 19 μm thick with a mean spacing of 230 μm. Not only are more photons produced as a result of the incident particle crossing more dielectric boundaries, but constructive interference between radiation from successive boundaries increases the overall radiated energy.

Since the X-rays interact electromagnetically at a single point in the chamber, a TR X-ray is observed as a large pulse on just one of the wires of the chamber. The likelihood of the finding X-ray decreases exponentially with the distance travelled through the chamber so they are generally found on one of the front wires in the chamber. Figure 6.4 shows the integrated charge distribution on the front 6 wires of a RWDC for electrons and pions in Xe:He:C_2H_6 30:40:30 gas mixture. The TR signal is clearly visible when electrons are used, particularly on the front wire but also on the second, third and fourth wires.

6.3 e/π Separation Using Transition Radiation

6.3.1 Beam Purity and Event Selection

As described in section 3.2, electrons were produced at CERN by directing a secondary beam from the SPS onto a lead target. Pions were produced from a 40 cm long copper target. Unlike the electron beam which is reasonably pure ($\pi/e < \sim 1$ %) [24] the pion beam is contaminated by electrons. Electrons were removed from the pion beam by using a 5 mm thick lead absorber at momenta of between 20 and 50 GeV/c. At lower momentum the absorber could not be used since the pions would also be absorbed, so Cherenkov counters were relied upon to act as a veto for electrons in the trigger. Two Cherenkov counters were available containing He and N_2 respectively. The gas pressure in the Cherenkovs could be varied to provide the optimum e/π discrimination at each

energy. The effectiveness of the Cherenkov counters was assessed as follows:

Particle momentum	5 mm Pb absorber	Cherenkovs used	Beam contamination	Cherenkov efficiency	Trigger contamination
5 GeV/c	no	He and N_2	43 %	99 %	~0.5 %
10 GeV/c	no	He and N_2	40 %	98 %	~0.8 %
20 GeV/c	yes	He and N_2	19 %	96 %	~0.8 %
50 GeV/c	yes	–	–	–	?

Table 6.1: Purity of the pion beam used at CERN.

1. The efficiency of the Cherenkovs was measured at each energy by measuring the fraction of the *pure electron* beam of that energy producing output from the Cherenkovs.

2. The Cherenkovs were then used in the *pion* beam of the same momentum. Again the fraction of the beam vetoed by the Cherenkovs was measured.

3. Although some of the vetoes from the pion beam could have come from real pions and not contaminating electrons, this would be small compared to the number of vetoed electrons. The Cherenkov efficiency measured with the electron beam could then be used to estimate the number of electrons left in the pion beam.

Table 6.1 shows the level of contamination in the pion beam at different energies and the techniques used to purify the beams. At 50 GeV, pions are travelling fast enough to produce Cherenkov radiation even at the lowest pressure possible in the counters installed in the CERN beam. There is therefore no good estimate of the contamination of the 50 GeV pion beam.

To simulate the effect of the three supermodules in the H1 forward track detector, 3 events from the single RWDC in the test beam were analyzed together as though they formed a single track through the complete FTD. Only events containing a single track

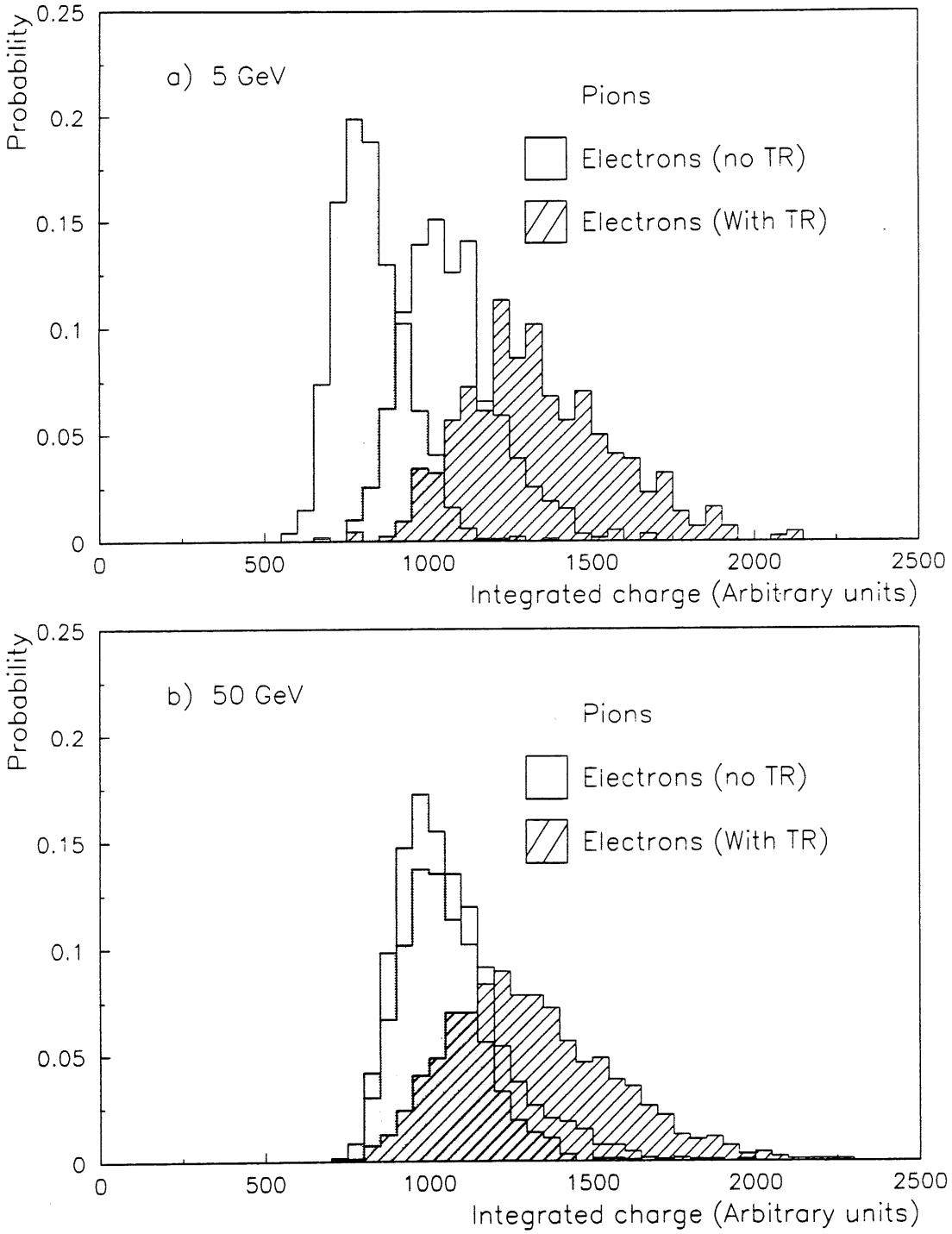

Figure 6.5: Mean charge distribution over 3 events for pions and electrons both with and without TR in Xe:He:C_2H_6 30:40:30 gas mixture.

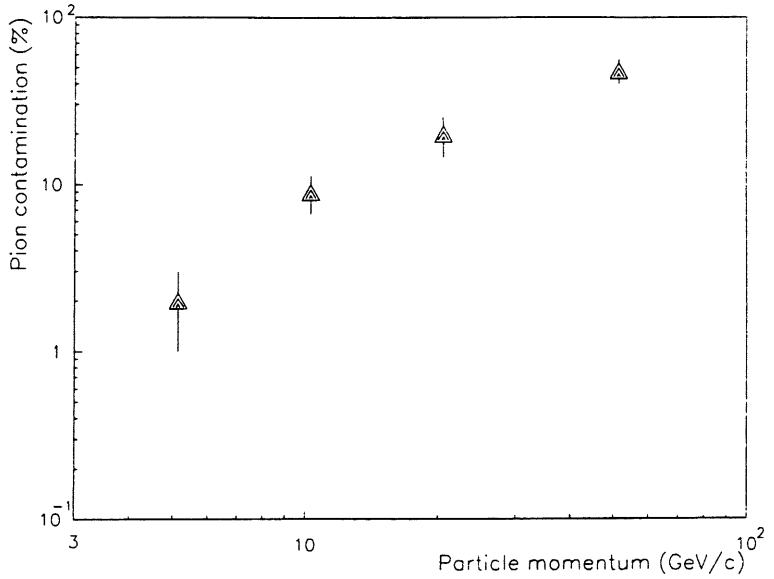

Figure 6.6: Pion contamination for 90 % electron acceptance using the mean charge method in Xe:He:C_2H_6 30:40:30 gas mixture.

with $\geq$ 9 pattern recognized hits were used so the three events were not necessarily consecutive. With an electron contamination of the pion beam at the level of $\sim$ 1 %, the probability of three events from the test beam all being pions is only 1 in 10^6 and the probability of having two pions and one electron is 3 in 10^4. The effect of beam contamination on the results of the test beam analysis is small enough to be ignored provided that the measured contamination is greater than the uncertainty in the purity of the beam.

6.3.2 Simple Mean Charge Method

The most simple method of separating electrons and pions using transition radiation is to compare the mean charge on all wires. Data taken using a 20 GeV pion beam were analyzed to determine the relative gain of each wire using the dE/dx spectra for each wire in the wedge under test. A correction was then applied to the charge integral from each wire so that the mean dE/dx was the same throughout the wedge. Figure 6.5 shows the mean charge over 3 events for pions and electrons both with and without transition radiator in Xe:He:C_2H_6 30:40:30 gas mixture at beam momenta of 5 and 50 GeV/c.

The pion contamination for 90 % electron acceptance at different energies is shown in figure 6.6. At 5 GeV the contamination is low ($\sim$ 2 %) but as the relativistic rise in the dE/dx increases the mean pulse charge integrals for pions the e/π discrimination gets considerably worse, reaching $\sim$50 % at a momentum of 50 GeV/c.

6.3.3 Maximum Likelihood Method

The simple mean charge method described above averages the very strong signal from the TR on the front wire over all 12 wires in the RWDC. The analysis then follows essentially the same path as that for dE/dx alone and therefore does not use all of the information available from the chamber. The maximum likelihood method analyzes the charges wire by wire and therefore exploits the distribution of the TR X-rays in the chamber.

Normalized spectra for each wire like those shown in figure 6.4 were used as a priori probability density functions f_e^i and f_π^i where i is the wire number ($1 \leq i \leq 12$). For a given event (or rather a group of 3 events) the joint probability W_e of the particle being an electron is

$$W_e = \prod_{j=1}^{N} f_e^i(E_j)^{\ddagger} \tag{6.3}$$

where E_j is the charge on each wire and the number of wires (N) varies between 27 and 36 for three track segments. Similarly the joint probability of the particle being a pion is

$$W_\pi = \prod_{j=1}^{N} f_\pi^i(E_j) \quad . \tag{6.4}$$

The likelihood quotient P_π (i.e. the likelihood that the particle is a pion) is then calculated from:

$$P_\pi = \frac{W_\pi}{W_e + W_\pi} \quad . \tag{6.5}$$

It can be seen that calculating a similar likelihood quotient for electrons P_e is not necessary since $P_e + P_\pi = 1$.

The likelihood quotients for a sample of 20 GeV electrons and pions in Xe:He:C_2H_6 30:40:30 gas mixture are shown in figure 6.7 and the pion contamination for 90 %

‡ Separate indices i and j are used since the analysis is over 27–36 wires yet only 12 probability distributions are required.

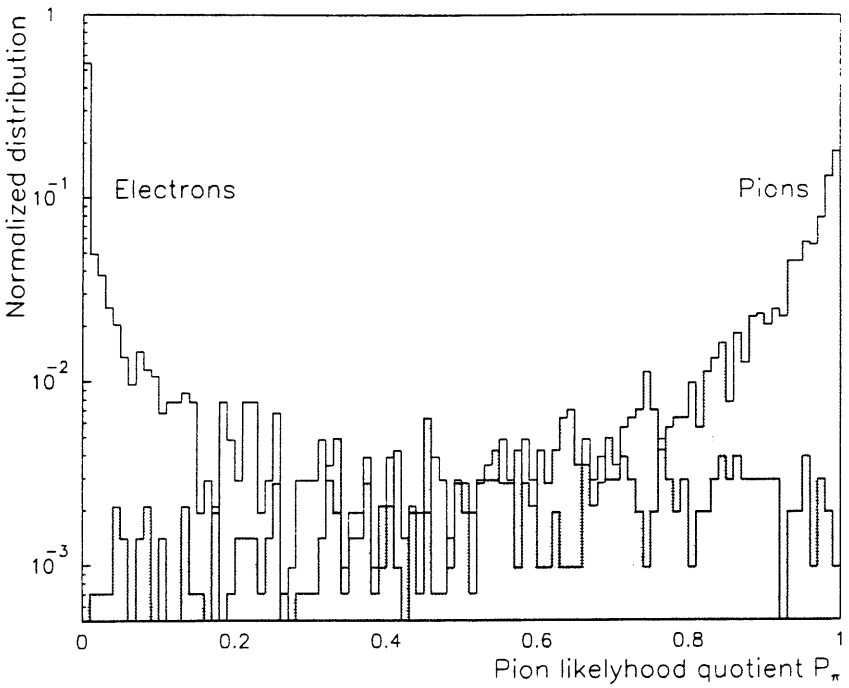

Figure 6.7: Likelihood distribution for 20 GeV electrons and pions in Xe:He:C_2H_6 30:40:30 gas mixture.

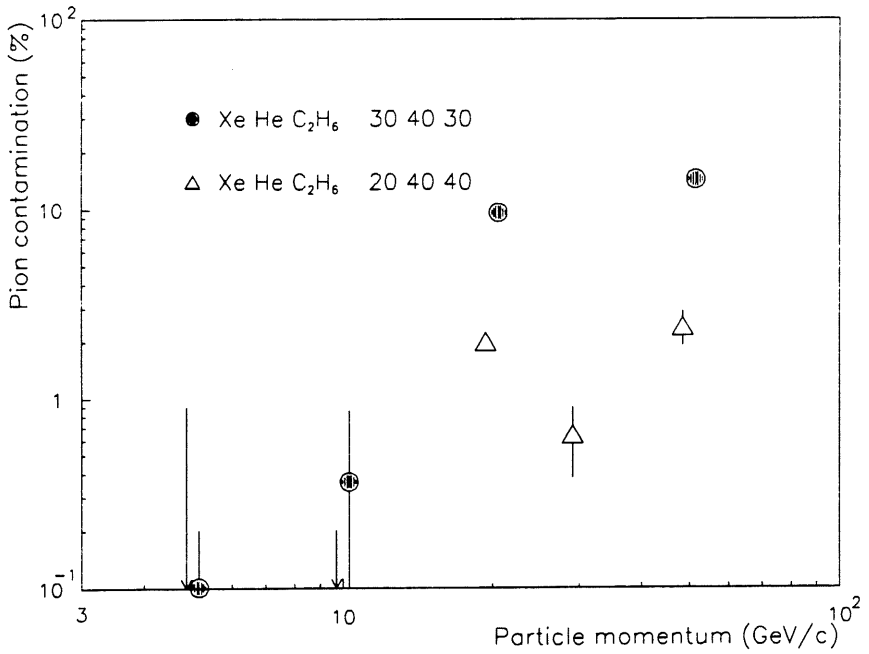

Figure 6.8: Pion contamination for 90 % electron acceptance using the maximum likelihood method in Xe:He:C_2H_6 30:40:30 and Xe:He:C_2H_6 20:40:40 gas mixtures.

electron acceptance at different energies using two different Xenon based gas mixtures are shown in figure 6.8. There are typically 1000 entries in the likelihood distributions for each particle type at energies above 20 GeV in each gas mixture. At lower energies, the sample is considerably lower since the rate of the CERN beam is lower at these energies limiting the number of events which could be recorded. At 5 and 10 GeV there were only 100 and 500 entries respectively. This puts a lower statistical limit on the measured contamination at these energies of up to 1 %. At 5 and 10 GeV in Xe:He:C_2H_6 20:40:40 gas mixture no pion events were mistakenly identified as electrons and at these energies in Xe:He:C_2H_6 30:40:30 gas mixture only one pion at 5 GeV and two at 10 GeV were mistakenly identified as electrons.

The e/π separation is clearly better in the gas mixture containing only 20 % Xenon. There are two possible reasons for this:

- The gain of the front wire in the Xe:He:C_2H_6 30:40:30 gas mixture was approximately half that on the other wires in the chamber. This would lead to a reduced efficiency on that wire and a reduction in the fraction of transition radiation detected.

- In the Xe:He:C_2H_6 20:40:40 gas mixture, not only was the gain on the front wire similar to that in the rest of the wedge, but a smaller fraction of the TR X-rays would deposit their energy in the vicinity of the front wire in any case.

It was shown in section 2.2.3 (figure 2.8) how the gain of the front wire may be adjusted independently of the other wires in the chamber. Unfortunately the front field former potential was not optimized during the tests at CERN so it is possible that the e/π separation in the 30:40:30 gas mixture could be improved.

6.4 Discussion and Conclusions

The results presented above were taken from data at a single point in the chamber with the electron and the pion data generally being collected within 30 minutes to 1 hour. The maximum likelihood method compares the electron and pion spectra on a wire by wire basis and, therefore, would not have been affected by an over all change in gas

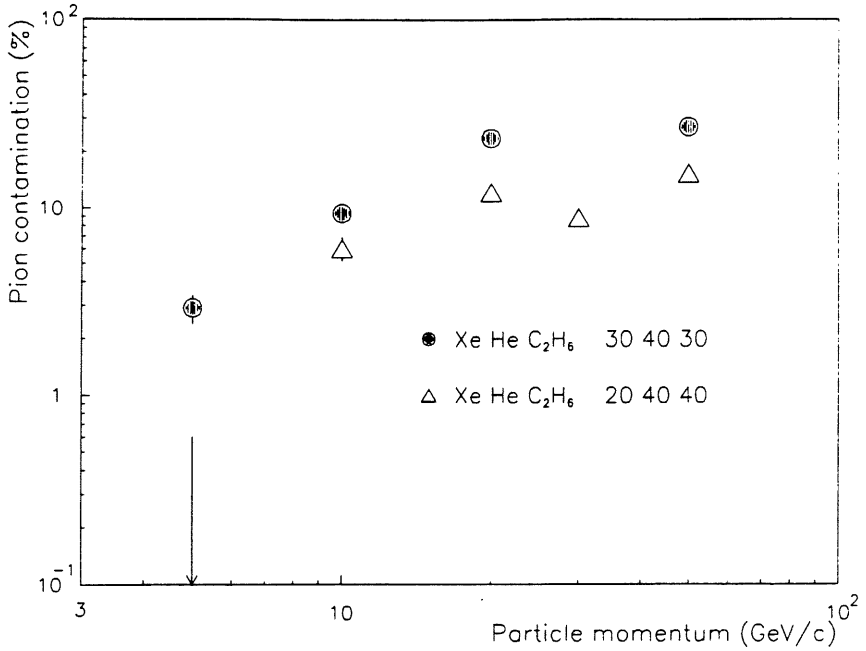

Figure 6.9: Pion contamination for 90 % electron acceptance using the maximum likelihood method for only two RWDC track segments in Xe:He:C_2H_6 30:40:30 and Xe:He:C_2H_6 20:40:40 gas mixtures.

gain. In H1 there are several factors which will affect the gas gain and will have to be accounted for:

- For small changes of pressure P, the avalanche gas gain G varies according to

$$\frac{\Delta G}{G} = -\alpha \frac{\Delta P}{P} \tag{6.6}$$

  where $\alpha \approx 12.5$ [25]. That is, a 1 % change in pressure can result in a change in the gas gain of over 12 % ! Gas gain will also vary with the gas composition and will therefore need to be carefully monitored.

- Since the data was all taken at a single point in the chamber, it was not necessary to correct for possible variations in gain with both the radial and the drift coordinates. Real tracks will also be at an angle to the wire plane which leads to an increase in the track length within a drift cell and consequently the amount of primary ionization produced in that cell. This may of course be easily corrected for using tracking information. The ionization from a TR X-ray remains constant

however, so the correction will tend to reduce the magnitude of the TR ionization compared with the dE/dx ionization.

- Due to the different chamber operating conditions in the 1.2 T H1 magnetic field, it will be necessary to create new electron and pion probability distributions for the maximum likelihood analysis. This requires an a priori form of electron identification which should be possible using the H1 calorimeter and needs to be done as a function of particle momentum for each wire.

Only tracks angled between 7° and 16° to the beam pipe will pass through all three supermodules of the FTD, tracks angled between 17° and 24° will only pass through 1 or two RWDCs. Figure 6.9 shows the pion contamination for 90 % electron efficiency using the maximum likelihood method for tracks which are only detected in two RWDCs (whether it be due to the geometry of the FTD or the failure of the pattern recognition software to link all 3 track segments). Comparing figures 6.8 and 6.9 it is clear that there is a significant increase in the pion contamination when only two track segments are available.

So far the RWDCs in H1 have only been operated with Ar:C_2H_6 50:50 gas mixture. When a Xenon based gas mixture is eventually put into the chambers, the prospects for e/π separation using TR look very promising, particularly in Xe:He:C_2H_6 20:40:40 gas mixture. Ultimately the e/π separation is going to depend on our ability to accurately monitor the operating conditions in the RWDC and the efficiency of the pattern recognition software at finding and linking track segments.

Chapter 7

Conclusions

7.1 Introduction

The HERA accelerator and the H1 detector have been built to study interactions between leptons and quarks at a center of mass energy of up to 314 GeV. To fully exploit the physics potential of such interactions the H1 detector is asymmetrical in design with enhanced charged track detection and particle identification in the forward proton direction.

Radial Wire Drift Chambers (RWDCs) play a central role in the forward region both as a tracking device and to detect Transition Radiation (TR), which is used to separate electrons and pions in the dense multi-track environment of the FTD. Despite the complexities of the radial geometry of the chambers, they are electrostatically very similar to more conventional drift chamber designs. The requirement of total ionization collection close to the front of the chambers for efficient TR detection has led to a very careful design of the front window of the RWDCs. The gain of the front wire can be varied independently of the other wires in the chamber.

A full sized RWDC was tested in a high energy electron/pion beam at CERN during the summer of 1991 [44]. The tests confirmed the results of previous prototype tests using an electron beam at DESY and allowed a thorough investigation of the techniques which are needed to accurately calibrate the chambers installed in H1. The results presented in chapter 6 are the first investigation of the e/π separation possible

Run 24647 Event 1562 Class: 12 14 Date 21/09/1992

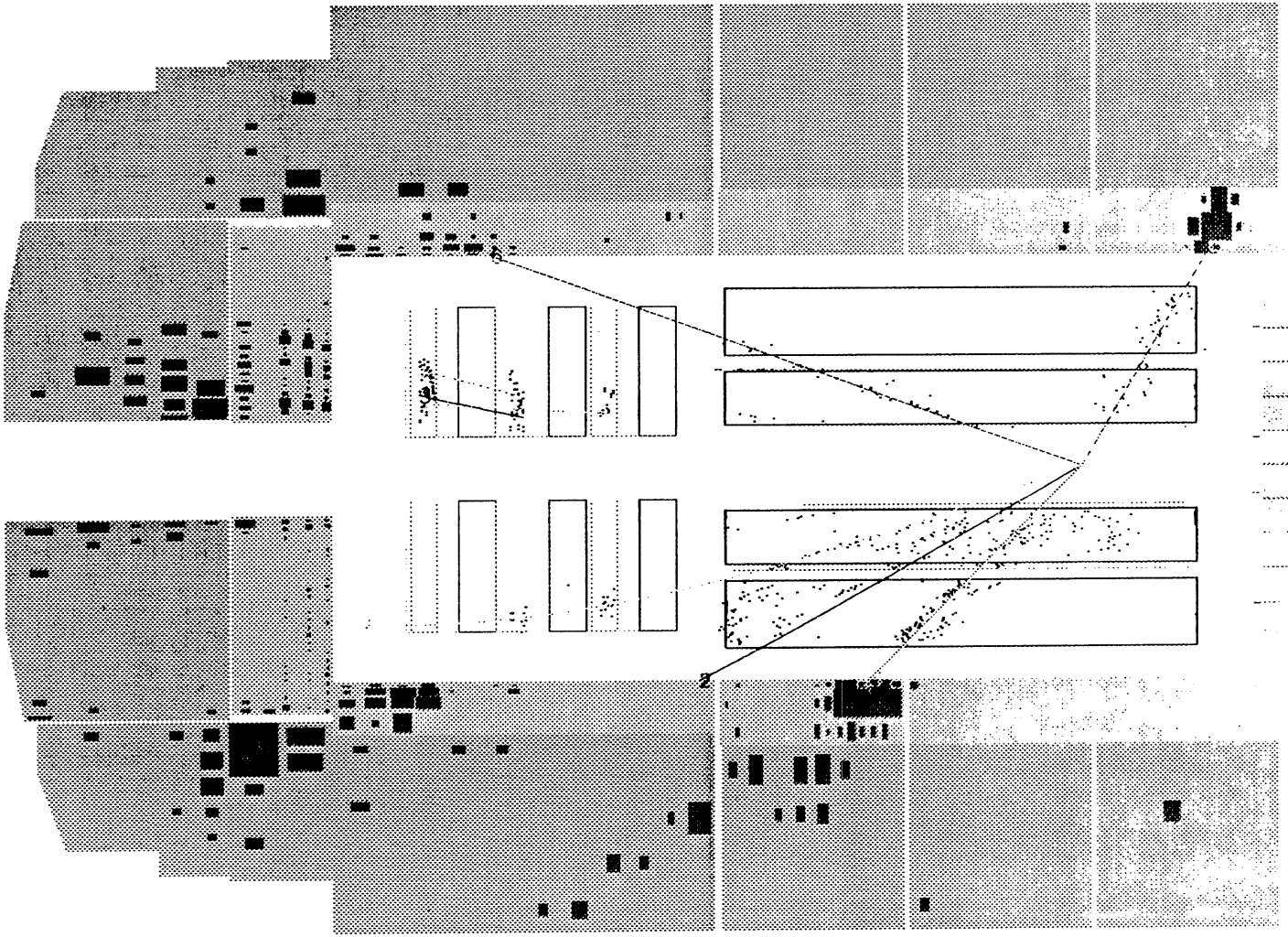

R

Z

Figure 7.1: (previous page) A typical DIS interaction in the H1 Detector.

with the chambers using a real pion beam.

The first data at HERA at full beam energy, colliding one bunch of protons with one bunch of electrons was taken on Sunday May 31 1992. Luminosity was initially $\sim$ 0.01 % of the design value. On Sunday July 19, 20 bunches of electrons and 20 of protons were succesfully injected into HERA and the luminosity was increased to $\sim 1.9 \times 10^{29}$ cm^{-2}s^{-1}, which is $\sim$ 1 % of the design value.

A typical DIS interaction in the H1 detector is shown in figure 7.1. Five tracks have been reconstructed in the CTD and three in the FTD, one track being successfully linked between the two sub-detectors.

7.2 Drift Coordinate Precision in RWDCs

Drift coordinate errors were discussed in detail in chapter 4. An important result of the test beam studies using different gas mixtures is that the point precision was similar in all of the mixtures tested. This means that the choice of gas used in H1 can be based on the requirements of good TR detection without adversely affecting the performance of the RWDCs as a tracking device.

To fully exploit the space point precision of the RWDCs, careful calibration will be necessary to remove all sources of systematic error. Drift coordinates are affected by cross talk between adjacent wires in the chambers at a level of up to 100μm. Due to the design of the H1 FADCs and the front end processing electronics, direct compensation by adding a fraction of the pulse from adjacent wires to each pulse is impractical. It does, however, appear possible to parameterize the effect of cross talk on the drift times and make a correction to the drift coordinates on the basis of the time difference between pulses on adjacent wires during later stages of track reconstruction. The other sources of systematic error in the RWDCs were discussed in section 4.2. Accurate measurement of the electron drift velocity still poses a problem for the RWDCs which must be resolved. When sufficient data become available, it will also be possible to

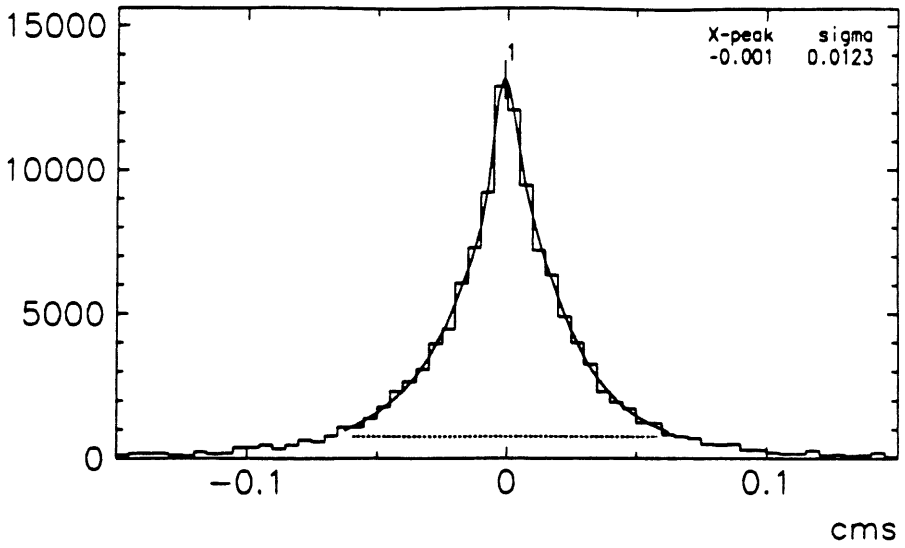

Figure 7.2: Drift residuals to fitted track segments in all three RWDCs installed in H1.

make corrections for the precise positions of each wire in the chambers and to improve the individual wire t_0 measurements, which were originally measured from test pulse data, using the techniques described in section 4.2.3.

Figure 7.2 shows the residuals to straight lines fitted to track segments in all three RWDCs installed in H1 [40]. The width of the distribution is 190 μm, however, the results plotted in the figure are simply the residuals to the fitted track segments and do not allow for the two free parameters in the fit. Since the number of space points per track segment is $\sim 6^{\dagger}$, the true drift coordinate error is $\sim 230\,\mu$m which is considerably worse than the results for Ar:C_2H_6 50:50 gas mixture presented in section 4.3. No parametric cross talk compensation has yet been implemented for H1 data analysis and the geometrical and t_0 corrections have not been made. It is therefore likely that this result will improve once a full calibration has been implemented.

7.3 Radial Coordinate Errors in RWDCs

The radial coordinate, which is measured by charge division on a pair of anode wires linked at the hub, is dominated by a large systematic shift of up to 8 cm. This shift varies both with the radial coordinate and with the charge integration time. There is no evidence to suggest that this shift is unique to the RWDCs, although the situation

† Up until November 1992 only the front 8 wires of the RWDCs were instumented, so 6 space points per track represents an efficiency of 75 %

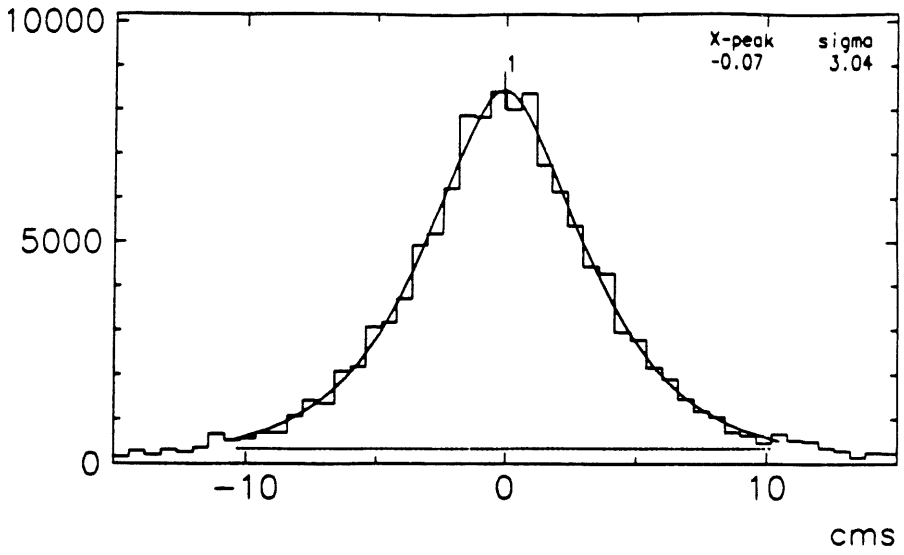

Figure 7.3: Radial residuals to fitted track segments in all three RWDCs installed in H1.

is evidently made more complicated by the hub connections and the effect they have on pulses propagating through them. Test beam data were used to measure this effect and simple parameterizations which can be used to correct for it were presented in section 4.4.

A simulation of drift chamber pulses presented in chapter 5, although not able to quantitatively reproduce the systematic error, shows that it is a result of changes in the shapes of the pulses resulting from the capacitance and inductance of the wires in the RWDC wedges. In the 1.2 T magnetic field of H1, pulse shapes are likely to be different than those from the test beam studies where there was no magnetic field. This would be due to changes in the drift trajectories of electrons towards the anode wires and also to changes in the migration of positive ions away from the anodes (sections 5.2.1 and 5.2.2 respectively). The corrections that need to be made to the radial coordinates are therefore likely to be different and will have to be measured using track information from the PWDCs, which have a homogeneous resolution in both x and y. The correction could also be affected by any changes in the gas mixture used or the chamber operating conditions which will affect the shapes of pulses in the chamber.

Figure 7.3 [40] shows the residuals to fits to the charge division coordinates of RWDC track segments in all 3 RWDCS in H1. The width of the distribution is 2.8 cm. As for the drift coordinate, this result takes no account of the free parameters in the

fit, so the radial coordinate error is $\sim$ 3.4 cm which is again worse than the test beam results presented in section 4.5. It is hoped that, due to the lower noise levels present in H1 data compared to the test beam data, this can also be improved upon when the systematic errors have been fully understood and corrected. The ultimate aim is to achieve a charge division coordinate precision of 1.3 cm (1 %) of the total length of a pair of wires in a RWDC.

7.4 Transition Radiation Detection

The electron-pion separation using transition radiation was measured at CERN in two Xenon based gas mixtures; Xe:He:C_2H_6 30:40:30 and Xe:He:C_2H_6 20:40:40. In the ideal conditions of the test beam, it was found that with the 20:40:40 mixture, the pion contamination for 90 % electron efficiency varied between zero at momenta of 5 and 10 GeV/c and 2.4 % at 50GeV/c. The results for the 30:40:30 show a higher contamination, which reaches 15 % at 50 GeV/c.

So far, the RWDCs installed in H1 have only been operated using Ar:C_2H_6 50:50 gas mixture and no attempt has so far been made to look for transition radiation. When the RWDCs are operated in a Xenon based gas mixture in 1993, it will be necessary to isolate a sample of electrons using the liquid argon calorimeter and a sample of non-radiating particles, to construct probability distributions similar to those shown in figure 6.4. A good understanding of the gas gain and individual wire gain calibration will also be necessary if the e/π separation achieved in the test beam is to be repeated in H1. From the results of the CERN tests however, the outlook for particle identification using the RWDCs looks very promising.

Appendix A

Calibration Constants From Test Pulse Data

A.1 Determination of Calibration Constants

This section describes how the parameters listed in section 3.5 are extracted from QT analyzed test pulse data. A schematic diagram of the layout of the test pulses relative to the wires and preamplifiers is shown in figure A.1. The two ends of the wire are pulsed alternately and the data analyzed using the QT code described in section 3.4. During the tests at CERN, 1000 test pulses were input to each end of the wires instrumented on a single occasion. At H1, test pulses are taken regularly to continuously monitor the RWDCs and their associated read-out. Calibration constants for the CERN tests were based on average measurements using all of the test pulses.

The available information consists of the final "drift" time T_D which is the weighted mean of the times at the two ends of the wire:

$$T_D = \frac{Q_L T_L + Q_R T_R}{Q_L + Q_R} \tag{A.1}$$

where T_L, T_R, Q_L and Q_R are the times and pulse integrals measured from FADC data at each end of the anode. Also available are the pulse integrals Q_L and Q_R and the time difference between the pulses at the two ends:

$$\Delta T = T_L - T_R \tag{A.2}$$

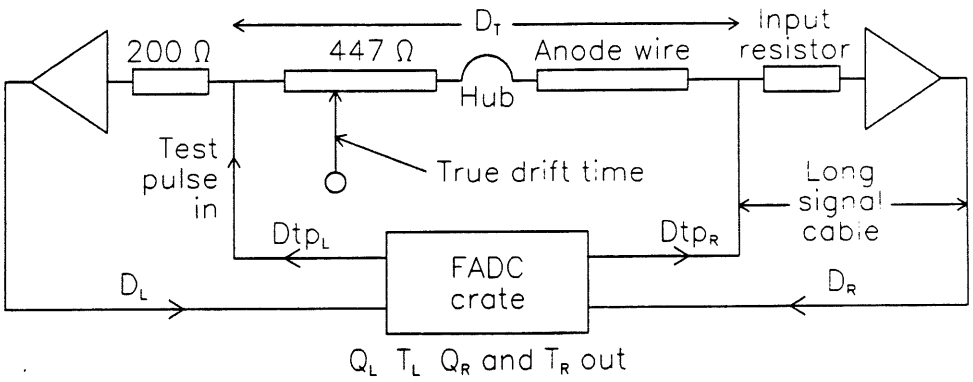

Figure A.1: Layout of test pulse inputs.

For a test pulse at the *L*eft end of the wire the difference in arrival times of the signal at each end is

$$\Delta T_L = D_L - (D_R + D_T) \tag{A.3}$$

similarly for a pulse at the *R*ight end:

$$\Delta T_R = (D_L + D_T) - D_R \tag{A.4}$$

Where D_L, and D_R are the propagation delays along and the output signal cables as depicted in figure A.1.

The term D_D is defined by:

$$D_D \equiv D_L - D_R \tag{A.5}$$

and is therefore easily extracted from equations A.3 and A.4

$$\Delta T_L + \Delta T_R = 2(D_L - D_R) = 2D_D \quad . \tag{A.6}$$

D_T is given by

$$\Delta T_L - \Delta T_R = -2D_T \tag{A.7}$$

To calculate the relative amplifier gains and the gain products it is necessary to make the distinction between a pulse integral at the *L*eft end which derives from a *L*eft end test pulse: Q_L^L and a pulse integral again measured at the *L*eft end but this time created by pulsing the *R*ight end Q_L^R. The terms Q_R^L and Q_R^R are similarly defined as pulse integrals from the *R*ight end of the wire which derive from test pulses at the *L*eft

and *R*ight ends respectively. It is also necessary to define $C_{L,R}^{L,R}$ which are the charges *entering* the preamplifiers as opposed to $Q_{L,R}^{L,R}$ which are the *measured* charges and therefore include the amplifier gains and signal cable attenuations. If G_L and G_R are the combined amplifier gains and cable attenuations at each end then $Q_L^{L,R} = G_L C_L^{L,R}$ and $Q_R^{L,R} = G_R C_R^{L,R}$.

If the preamplifier input impedance is the same at each end, then the two ratios of the larger charge C to the smaller one will be the same:

$$\frac{C_L^L}{C_R^L} = \frac{C_R^R}{C_L^R} \equiv \frac{1}{\beta} \tag{A.8}$$

so

$$\frac{Q_L^L}{Q_R^L} = \frac{G_L}{G_R}\frac{1}{\beta} \tag{A.9}$$

and

$$\frac{Q_L^R}{Q_R^R} = \frac{G_L}{G_R}\beta \tag{A.10}$$

β is then calculated using:

$$\beta = \left(\frac{Q_L^R Q_R^L}{Q_L^L Q_R^R}\right)^{\frac{1}{2}} \tag{A.11}$$

and the relative gain $\frac{G_L}{G_R}$ is calculated from

$$\frac{Q_L^L}{Q_L^R}\frac{Q_R^L}{Q_R^R} = \left(\frac{G_L}{G_R}\right)^2 \quad . \tag{A.12}$$

In order to extract the gain product it is necessary to assume that the magnitude of the test pulse input to each end of the wire is the same and therefore that $C_L^R = C_R^L$ and $C_L^L = C_R^R$. Then:

$$\left(Q_L^L + Q_L^R\right)\left(Q_R^L + Q_R^R\right) = G_L(1+\beta)C_L^L G_R(1+\beta)C_R^R = C_L^L C_R^R(1+\beta)^2 G_L G_r \tag{A.13}$$

Since an absolute measurement of individual gain products is unnecessary and the term $C_L^L C_R^R(1+\beta)^2$ is assumed to be constant for all wires, for convenience the gain products for all wires were normalized so that the mean gain product is 1.

The t_0 for each wire is defined as the mean propagation time from the center of the wire to the FADCs:

$$t_0 \equiv \frac{1}{2}(D_L + D_R + D_T) \tag{A.14}$$

To calculate t_0 it is necessary to make an assumption about the times taken for the test pulse signals to propagate from the FADC crate to the preamplifier input Dtp_L and Dtp_R. Test pulses are sent to the preamplifiers along the same cables that return the preamplifier output signals to the FADCs. As described in section 2.3.3 each test pulse is distributed to four individual channels on the preamplifier boards. Therefore, the time for signal propagation to the preamplifiers from the FADCs is taken as the average of the four separate propagation times from the preamplifiers back to the FADCs:

$$Dtp_{L,R} = \frac{1}{4}\sum_{i=1}^{4} D^i_{L,R} \tag{A.15}$$

The final times (equation A.1) measured from test pulses at each end are:

$$T^L_D = Dtp_L + \frac{D_L}{1+\frac{G_R}{G_L}\beta} + \frac{\frac{G_R}{G_L}\beta D_T}{1+\frac{G_R}{G_L}\beta} + \frac{\frac{G_R}{G_L}\beta D_R}{1+\frac{G_R}{G_L}\beta} \tag{A.16}$$

and

$$T^R_D = Dtp_R + \frac{\frac{G_R}{G_L}\beta D_L}{1+\frac{G_R}{G_L}\beta} + \frac{\frac{G_R}{G_L}\beta D_T}{1+\frac{G_R}{G_L}\beta} + \frac{D_R}{1+\frac{G_R}{G_L}\beta} \tag{A.17}$$

The test pulse propagation time can be obtained from equations A.15, A.16 and A.17:

$$T^L_D + T^R_D - 2\frac{\frac{G_R}{G_L}\beta D_T}{1+\frac{G_R}{G_L}\beta} = Dtp_L + Dtp_R + D_L + D_R \tag{A.18}$$

then average over four wires:

$$\frac{1}{4}\sum_{i=1}^{4} T^L_D + T^R_D - 2\frac{\frac{G_R}{G_L}\beta D_T}{1+\frac{G_R}{G_L}\beta} = Dtp_L + Dtp_R + \frac{1}{4}\sum_{i=1}^{4} D^i_L + D^i_R = 2\left(Dtp_L + Dtp_R\right) \tag{A.19}$$

To calculate a final t_0 it can be seen that:

$$\frac{1}{2}\left(T^L_D + T^R_D + \alpha\frac{G_R}{G_L}T_D\right) = \frac{1}{2}\left(Dtp_L + Dtp_R + D_L + D_R + D_T\right) \tag{A.20}$$

where

$$\alpha = \frac{1-\beta}{1+\beta} = \frac{Q_L - \frac{G_L}{G_R}Q_R}{Q_L + \frac{G_L}{G_R}Q_R} \tag{A.21}$$

so subtracting off $\frac{1}{2}$ the sum of the mean test pulse delays from equation A.19 gives:

$$\frac{1}{2}\left(D_L + D_R + D_T\right) \tag{A.22}$$

which is t_0 as defined in equation A.14.

The final quantity calculated from the test pulse data is $\frac{L_{eff}}{L}$: the ratio of the effective wire length to the true wire length used in charge division reconstruction to calculate the radial coordinate R:

$$\frac{R}{L} = \frac{Q_L - \frac{G_L}{G_R}Q_R}{Q_L + \frac{G_L}{G_R}Q_R} \times \frac{L_{eff}}{L} \tag{A.23}$$

At the end of the anode wire the quantity $\frac{R}{L} = 1$ by definition. The charges from a chamber hit at either end of the wire divide in the ratio $\frac{1}{\beta}$ as defined in equation A.8. $\frac{L_{eff}}{L}$ is therefore given by:

$$\frac{L_{eff}}{L} = \frac{1+\beta}{1-\beta} = \frac{1}{\alpha} \ . \tag{A.24}$$

A.2 Corrections Applied to Drift Times Using Test Pulse Calibration Constants

If the true (corrected) drift time in the chamber is D_{corr} then the time calculated from equation A.1 will be:

$$T_D = \frac{Q_L\left(T_{corr} + \frac{1}{2}(1-\gamma)D_T + D_L\right) + Q_R\left(T_{corr} + \frac{1}{2}(1+\gamma)D_T + D_R\right)}{Q_L + Q_R} \tag{A.25}$$

where γ is the fractional distance from the center of the chamber to the *L*eft end of the wire ($-1 \leq \gamma \leq 1$).

From equations A.5 and A.14:

$$D_L = t_0 - \frac{D_T - D_D}{2} \quad \text{and} \quad D_R = t_0 - \frac{D_T + D_D}{2} \tag{A.26}$$

Substituting this into equation A.25 and rearranging gives

$$T_{corr} = T_D - \left\{t_0 + \frac{1}{2}\alpha D_D - \frac{1}{2}\alpha\gamma D_T\right\} \ . \tag{A.27}$$

which is used during track reconstruction to correct the 'raw' drift time of each hit during the calculation of drift distances in an RWDC.

Appendix B

Calculation of the RWDC Impulse Response

B.1 The Capacitance, Inductance and Propagation Delays along a RWDC Anode and Hub Connection

No attempt has been made to calculate the inductance and capacitance of a RWDC by solving Maxwells equations for the complicated RWDC geometry. Capacitance and inductance are instead estimated by comparing components of the RWDC with idealized situations such as infinitely long parallel conductors and long wires above infinite plates for which capacitance and inductance can be calculated with relative ease.

B.1.1 Capacitance

Most undergraduate text books on electromagnetism [41] give simple formulae for the capacitance per unit length of a pair of infinitely long parallel wires, each of radius a, with a distance between their centers b, as

$$C \approx \frac{\pi \varepsilon_0 \varepsilon_r}{\log_e\left(\frac{b}{a}\right)} \quad . \tag{B.1}$$

For two wires of different radii a_1 and a_2 this may easily be extended. If the charge per unit length on a wire is λ the electric field $E(r)$ at a distance r is

$$E(r) = \frac{\lambda}{2\pi\varepsilon_0\varepsilon_r r} \tag{B.2}$$

so the total potential V between the two conductors is

$$V = \frac{\lambda}{2\pi\varepsilon_0\varepsilon_r}\left[\int_{a_1}^{b-a_2}\frac{dr}{r} + \int_{a_2}^{b-a_1}\frac{dr}{r}\right] = \frac{\lambda}{2\pi\varepsilon_0\varepsilon_r}\log_e\left\{\frac{(b-a_1)(b-a_2)}{a_1 a_2}\right\} \quad . \tag{B.3}$$

Using the approximation that $a \ll b$ the capacitance C per unit length is then

$$C = \frac{\lambda}{V} \approx \frac{2\pi\varepsilon_0\varepsilon_r}{\log_e\left\{\frac{b^2}{a_1 a_2}\right\}} \quad . \tag{B.4}$$

The capacitance per unit length of a long wire of radius a a distance b above an infinite plate is

$$C = \frac{2\pi\varepsilon_0\varepsilon_r}{\log_e\left\{\frac{2b}{a}\right\}} \quad . \tag{B.5}$$

B.1.1.1 Anode Capacitance

The anodes in a drift chamber are capacitively coupled to all other parts of the chamber. The principal components contributing to the capacitance of an anode will be the adjacent field wires and the cathode planes. The radii of the anode and field wires are 25 μm and 62.5 μm respectively. Each anode is 67 cm long and the gas will have a relative permittivity $\varepsilon_r \simeq 1$. The anode and field wires are 5 mm apart so the capacitance per unit length between an anode and a field wire is $\sim$ 5.8 pF/m.

The distance between the anode and the cathode varies between 1 cm close to the hub and 5 cm at the wide end of the wedge. The cathode plates are 12 cm wide which is reasonably large compared to the 1 cm separation at the hub so in this region equation B.5 is probably a reasonable approximation and the capacitance per unit length is $\sim$ 8.3 pF/m. At the wide end of the wedge the width of the cathode is not significantly larger than the distance to the wire plane, so equation B.5 will be a poor approximation of the capacitance. Still, using equation B.5, the capacitance per unit length at the wide end of the wedge is $\sim$ 6.7 pF/m.

An estimate of the capacitance of a RWDC wedge must therefore be somewhere between $(2 \times 5.8 + 2 \times 8.3) = 28.2$ pF/m close to the hub and $\sim (2 \times 5.8 + 2 \times 6.7) =$

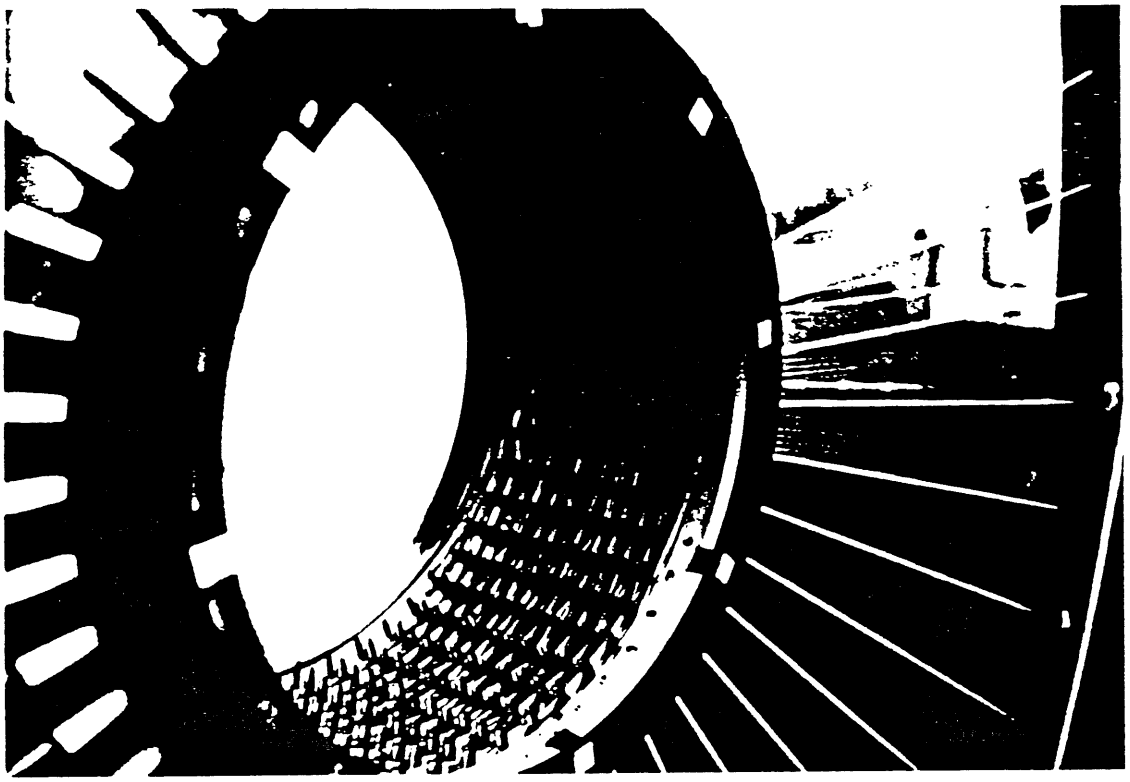

Figure B.1: Photograph of the connections linking pairs of wedges at the RWDC hub.

25 pF/m at the wide end of the wedge. For the simulation in chapter 5, I use a value of 17 pF for a 67 cm long anode.

B.1.1.2 Hub Capacitance

The connections linking pairs of wedges at the hub are un-shielded with an inner conductor of $\sim$ 0.21 mm radius. The connectors are packed into a single layer which fills the inner surface of the hub (figure B.1) so each connector is in contact with one other on either side over its full length of 25 cm. The diameter of the connectors is 1.6 mm and the insulating material is polythene which has a relative permittivity ε_r of 2.4. The capacitance between a pair of hub connectors is therefore $\sim$ 33 pF/m so the total capacitance between each connector and its two neighbors is $\sim$ 16.5 pF.

B.1.2 Inductance

The magnetic flux ϕ surrounding a wire carrying a current I at a distance r is

$$\phi(r) = \frac{\mu_0 I}{2\pi r} \tag{B.6}$$

so for two parallel conductors, of radii a_1 and a_2 and separation b, each one carrying a current I, the flux between them is

$$\Phi = \frac{\mu_0 I}{2\pi}\left[\int_{a_1}^{b-a_2}\frac{dr}{r} + \int_{a_2}^{b-a_1}\frac{dr}{r}\right] = \frac{\mu_0 I}{2\pi}\log_e\left\{\frac{(b-a_1)(b-a_2)}{a_1 a_2}\right\} \tag{B.7}$$

So using the approximation $a_{1,2} \ll b$ the mutual inductance L is

$$L = \frac{\mu_0}{2\pi}\log_e\left\{\frac{b^2}{a_1 a_2}\right\} \tag{B.8}$$

In the case of the two conductors having the same radii a this becomes

$$L = \frac{\mu_0}{\pi}\log_e\left\{\frac{b}{a}\right\} \quad . \tag{B.9}$$

The calculation of the mutual inductance of a wire above a plate requires a knowledge of the spatial distribution of the current in the plate which will vary as a function of the frequency of the signal. Equation B.8 may however be re-written in the form

$$L = \frac{\mu_0}{2\pi}\left[\log_e\left(\frac{b}{a_1}\right) + \log_e\left(\frac{b}{a_2}\right)\right] \tag{B.10}$$

and a rough estimate of the inductance made. At the narrow end of the wedge, the closest the wire comes to each cathode is $\sim$ 1 cm. The first term in equation B.10 would therefore contribute 1.2 μH. The furthest the current in the cathode can be from the anode is $\sim$ 6 cm and the first term from equation B.10 would contribute 1.6 μH. Similarly at the wide end of the wedge the first term in the equation will contribute between 1.5 μH and 1.6 μH. What to do with the second term in equation B.10 is less clear since there is no obvious value for a_2. If the cathode plate is, however, visualised as a large diameter wire, then it is clear that the flux density surrounding the cathode is much lower than that surrounding a thin wire so the contribution of the second term will be smaller than that from the first term in equation B.10. The mean mutual inductance between an anode wire and a cathode is therefore likely to be $\sim$ 1.5 μH.

B.1.2.1 Anode Inductance

If the inductance of the anodes were due entirely to a single field wire then from equation B.8 it would be 1.9 μH/m. From equation B.7 it is seen that current must flow back along the second conductor (ie. the field wire or cathode concerned) for it to contribute to the inductance. The *total* current flowing in both of the field wires and both of the cathodes is equal to the current flowing in the anode. The *total* inductance is therefore some weighted average of the inductance of a single field wire-anode combination and that of a single cathode-anode combination. Fortunately, the values of inductance for these are roughly the same so it is not necessary to have a good knowledge of exactly how much current flows in the cathodes and how much in the adjacent field wires. A reasonable approximation for the inductance of an anode wire 67 cm long would therefore be $\sim 1.2\,\mu$H.

B.1.2.2 Hub Inductance

A similar argument is used for the inductance of the hub connections as was used for the anodes. The inductance of a pair of adjacent connectors is $\sim 0.8\,\mu$H/m. The sharing of this between a connector on either side makes no difference so the final inductance of the hub connector is $\sim 0.2\,\mu$H.

B.1.3 Propagation Delays

The propagation time delay of a signal travelling along a transmission line is $(LC)^{\frac{1}{2}}$ [41] where L and C are the capacitance and inductance respectively. Using the values of L and C for the hub and the anodes calculated above, the delay in the hub is 1.8 ns and in the anodes the delay is 3.6 ns, both of which correspond to a velocity of 1.4×10^8 m/s or 0.5 c, where c is the speed of light in a vacuum.

The total length of wire between a pair of preamplifiers is 1.9 m. That is, 2×67 cm for the anodes, 25 cm for the hub connection and $\sim$ 30 cm for the wires connecting the ends of the anodes to the preamplifiers. The mean time difference for test pulses to travel between two preamplifiers (see section 3.5 was 13.9 ns (table 3.1) corresponding to a velocity of 1.4×10^8 m/s, which is the same as the predicted value above.

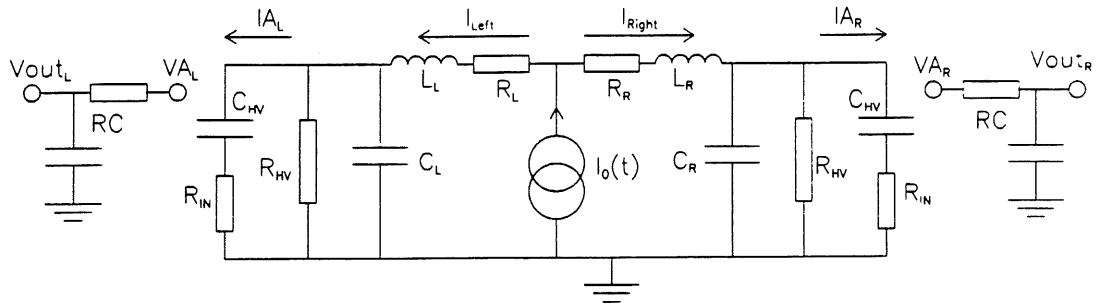

Figure B.2: Equivalent circuit used to calculate the RWDC impulse response.

B.2 Transfer Function for the RWDC Equivalent circuit

Before applying Thevenins theorem [42] to the RWDC equivalent circuit in figure 5.4, the circuit diagram may be modified slightly to make certain qualities of the circuit clearer.

- The central section of the circuit, ie. the part which represents the chamber, is completely isolated from ground by the decoupling capacitors at the preamplifier input. In practice the anodes are at some high voltage, the value of which is irrelevant to the calculation of the impulse response. Since the current through the decoupling capacitor is independent of the *static* high voltage on the chamber, the chamber can be assumed to be at ground potential and both the high voltage input and the base of the current source are therefore connected to ground.

- The input impedance of an operational amplifier connected in the way shown in figure 5.4 is simply that of the input resistor R_{IN}. For the calculation, therefore, the operational amplifier is removed and the input resistor connected to ground.

- The preamplifier acts as a buffer between the input resistor and the output RC circuit. The *voltage* at the output of the preamplifier is equal to the amplifier gain G times the *current* in the input resistor.

The circuit in figure 5.4 has been re-drawn, to illustrate these features more clearly, as is shown in figure B.2.

The first step in the calculation is to see how the current $I_0(t)$ divides between the two halves of the circuit to make I_L and I_R. The complex impedance Z_L of an

inductance L is given by $Z_L = sL$ where $(s = j\omega)$ and the complex impedance Z_C of a capacitance $C = \frac{1}{sC}$. The impedance of a resistor R is simply R, so the impedance $Z_{||}$ of the components on the left of the current source is $R_L + sL_L +$ the impedance of the parallel combination of the four components $\frac{1}{sC_L}$, R_{HV} and $\frac{1}{sC_{HV}} + R_{IN}$ which is given by

$$Z_{||} = \frac{1}{sC_L + \frac{1}{R_{HV}} + \frac{sC_{HV}}{sC_{HV}R_{IN}+1}}$$

$$= \frac{R_{HV}(1 + sC_{HV}R_{IN})}{s^2C_LC_{HV}R_{IN}R_{HV} + s(C_LR_{HV} + C_{HV}R_{IN} + C_{HV}R_{HV})} \tag{B.11}$$

So the total impedance of the components to the left of the current source is

$$Z_{Left} = R_L + sL_L + Z_{||} \tag{B.12}$$

which is of the form

$$Z_{Left} = \frac{s^3T_L^3 + s^2T_L^2 + sT_L^1 + T_L^0}{s^2B_L^2 + sB_L^1 + B_L^0} \tag{B.13}$$

where

$T_L^3 = L_LC_LC_{HV}R_{HV}R_{IN}$

$T_L^2 = L_L(C_{HV}R_{IN} + C_{HV}R_{HV} + C_LR_{HV}) + C_LC_{HV}R_LR_{HV}R_{IN}$

$T_L^1 = L_L + C_{HV}R_{IN}R_L + C_{HV}R_{HV}R_L + C_LR_{HV}R_L + C_{HV}R_{HV}R_L$

$T_L^0 = R_L + R_{HV}$

and

$B_L^2 = C_LC_{HV}R_{IN}R_{HV}$

$B_L^1 = C_LR_{HV} + C_{HV}R_{IN} + C_{HV}R_{HV}$

$B_L^0 = 1$

Similarly for the right hand side:

$$Z_{Right} = \frac{s^3T_R^3 + s^2T_R^2 + sT_R^1 + T_R^0}{s^2B_R^2 + sB_R^1 + B_R^0} \tag{B.14}$$

where

$T_R^3 = L_RC_RC_{HV}R_{HV}R_{IN}$

$T_R^2 = L_R(C_{HV}R_{IN} + C_{HV}R_{HV} + C_RR_{HV}) + C_RC_{HV}R_RR_{HV}R_{IN}$

$T_R^1 = L_R + C_{HV}R_{IN}R_R + C_{HV}R_{HV}R_R + C_RR_{HV}R_R + C_{HV}R_{HV}R_R$

$T_R^0 = R_R + R_{HV}$

and

$B_R^2 = C_R C_{HV} R_{IN} R_{HV}$

$B_R^1 = C_R R_{HV} + C_{HV} R_{IN} + C_{HV} R_{HV}$

$B_R^0 = 1$

The currents flowing into the left and right hand sides of the circuit are given by

$$I_{Left} = \frac{Z_{Right}}{Z_{Left} + Z_{Right}} I_0 \tag{B.15}$$

and

$$I_{Right} = \frac{Z_{Left}}{Z_{Left} + Z_{Right}} I_0 \tag{B.16}$$

The currents I_{Left} and I_{Right} then divide 3 ways between the chamber capacitance $C_{L,R}$, the high voltage feed resistor R_{HV}, and the combined impedance of the high voltage decoupling capacitor and the preamplifier input resistance C_{HV} and R_{IN}.

At the left end the current IA_L which flows in the preamplifier input resistor is

$$IA_L = \frac{sC_{HV}R_{HV}}{s^2 C_{HV} C_L R_{HV} R_L + s(C_L R_{HV} + C_{HV} R_{HV} + C_{HV} R_{IN}) + 1} I_{Left}$$

$$= \frac{sT_L^4}{s^2 B_L^5 + sB_L^4 + B_L^3} I_{Left} \tag{B.17}$$

where

$T_L^4 = C_{HV} R_{HV}$

$B_L^3 = 1$

$B_L^4 = C_L R_{HV} + C_{HV} R_{HV} + C_{HV} R_{IN}$

and

$B_L^4 = C_{HV} C_L R_{HV} R_L$

and at the right hand end

$$IA_R = \frac{sC_{HV}R_{HV}}{s^2 C_{HV} C_R R_{HV} R_R + s(C_R R_{HV} + C_{HV} R_{HV} + C_{HV} R_{IN}) + 1} I_{Right}$$

$$= \frac{sT_R^4}{s^2 B_R^5 + sB_R^4 + B_R^3} I_{Right} \tag{B.18}$$

where

$T_R^4 = C_{HV} R_{HV}$

$B_R^3 = 1$

$B_R^4 = C_R R_{HV} + C_{HV} R_{HV} + C_{HV} R_{IN}$

and

$B_R^4 = C_{HV} C_R R_{HV} R_R$

The preamplifiers used with the RWDC are charge sensitive (section 2.3.3) so the voltage at the output of the preamplifier ($VA_{L,R}$ in figure B.2) is given by

$$VA_{L,R} = G \times IA_{L,R} \tag{B.19}$$

where G is the sensitivity of the amplifier (in Volts/Amp).

Finally, the transfer function of the RC circuit on the output of each preamplifier (which represents the rise time of the preamplifier and signal cable) relates the output voltage at each end $Vout_{L,R}$ to $VA_{L,R}$ by

$$\text{Vout}_L = \frac{1}{sRC+1} VA_L \tag{B.20}$$

and

$$\text{Vout}_R = \frac{1}{sRC+1} VA_R \tag{B.21}$$

It is then possible to combine the coefficients in equations B.13, B.15, B.17 and B.20 for the left end and equations B.14, B.16, B.18 and B.21 for the right end to get the two transfer functions which take the form

$$\frac{\text{Vout}\,(s)}{I_0\,(s)} = \frac{\sum_{i=0}^{7} A_i s^i}{\sum_{j=1}^{8} C_j s^j} \tag{B.22}$$

That is, equations which have a numerator which is an 7^{th} order polynomial of s and a denominator which is an 8^{th} order polynomial of s.

In order to take the inverse Laplace transform of equation B.22 it is first necessary to factorize the denominator which changes the form of the equation to

$$\frac{\text{Vout}\,(s)}{I_0\,(s)} = \frac{\sum_{i=0}^{7} A_i s^i}{C_8 \prod_{j=1}^{8} (s+\alpha_j)} \quad . \tag{B.23}$$

In practice this is done by solving the 8^{th} order polynomial in equation B.22 for $s = 0$ [43]. In general the coefficients α_i may be complex and care must be taken to preserve a constant term (equal to C_8 from equation B.22) which is otherwise lost.

B.3 The Laplace Transform of 8 Exponential Decays

The Laplace transform of a single decaying exponential $Fe^{-\alpha t}$ is given by

$$\mathcal{L}\left\{Fe^{-\alpha t}\right\} = \int_0^\infty Fe^{-\alpha t}e^{-st}\,dt = F\frac{1}{s+\alpha} \tag{B.24}$$

The Laplace transform of 8 exponential decays is therefore

$$\mathcal{L}\left\{\sum_{i=1}^{8} F_i e^{-\alpha_i t}\right\} = \sum_{i=1}^{8} F_i \frac{1}{s+\alpha_i} \tag{B.25}$$

The 8 terms in equation B.25 may be combined so that there is a single, common, denominator:

$$\mathcal{L}\left\{\sum_{i=1}^{8} F_i e^{-\alpha_i t}\right\} = \frac{\sum_{i=1}^{8} F_i \left\{\prod_{j\neq i} (s+\alpha_j)\right\}}{\prod_{i=1}^{8} (s+\alpha_i)} \tag{B.26}$$

which is of the same form as equation B.23 since it consists of a numerator which is 7^{th} order in s over a denominator which is 8^{th} order in s.

The impulse response of the RWDC equivalent circuit is therefore the sum of 8 exponential decays:

$$Vout\,(t) = \sum_{i=1}^{8} F_i e^{-\alpha_i t} \tag{B.27}$$

where the coefficients α_i are the α_i from equation B.23. To obtain the values of F_i it is necessary to expand the numerator of equation B.26 and compare the different powers of s, ie.

$$\frac{A_0}{C_8} = F_1\alpha_2\alpha_3\alpha_4\alpha_5\alpha_6\alpha_7\alpha_8 + F_2\alpha_3\alpha_4\alpha_5\alpha_6\alpha_7\alpha_8\alpha_1 + F_3\alpha_4\alpha_5\alpha_6\alpha_7\alpha_8\alpha_1\alpha_2 + \cdots$$

$$\frac{A_1}{C_8} = F_1\left(\alpha_3\alpha_4\alpha_5\alpha_6\alpha_7\alpha_8 + \cdots + \alpha_2\alpha_3\alpha_4\alpha_5\alpha_6\alpha_7\right) + F_2\left(\alpha_1\alpha_4\alpha_5\alpha_6\alpha_7\alpha_8 + \cdots\right.$$

$$\vdots$$

$$\frac{A_5}{C_8} = F_1\left(\alpha_2\alpha_3 + \alpha_2\alpha_4 + \alpha_2\alpha_5 + \alpha_2\alpha_6 + \alpha_2\alpha_7 + \alpha_2\alpha_8 + \alpha_3\alpha_4 + \cdots + \alpha_7\alpha_8\right) + \cdots$$

$$\frac{A_6}{C_8} = F_1\left(\alpha_2 + \alpha_3 + \alpha_4 + \alpha_5 + \alpha_6 + \alpha_7 + \alpha_8\right) + F_2\left(\alpha_3 + \alpha_4 + \alpha_5 + \alpha_6 + \cdots + \alpha_1\right) + \cdots$$

$$\frac{A_7}{C_8} = F_1 + F_2 + F_3 + F_4 + F_5 + F_6 + F_7$$

Since the values of α_i are already known, these 8 simultaneous equations may be solved to obtain the values of F_i. Since the values of α_i may be complex, the values of F_i may also be complex, which leads to an impulse response containing both oscillating and exponentially decaying components.

References

[1] R.D. Peccei *ed. Proceedings of the HERA Workshop*, DESY, 1988.

[2] W. Buchmüller and G. Ingelman (eds.) *Physics at HERA*, DESY 1992

[3] C.P. Bee, PhD Thesis. University of Lancaster, 1983.

[4] P.N. Harriman *et.al.*, *Parton Distributions Extrapolated from Data on Deep-Inelastic Lepton Scattering, Prompt Photon Production and the Drell-Yan Process*, Rutherford Appleton Laboratory **RAL-09-007** 1990.

[5] Particle Data Group, *Review of Particle Properties*, Physics Letters **B204**, 1990.

[6] *Technical Proposal for the H1 Detector*, DESY, 1986.

[7] Halmatic Ltd. Hampshire, UK.

[8] J. VaVra, Nucl.Inst.Meth. **A252** 547 (1991).

[9] Noryl: Polyetherpolyphenylene plus 6 % filler (titanium oxide), Dupont, USA.

[10] H. Grässler *et al*, Nucl.Inst.Meth. **A310** 535 (1991).

[11] Permali Ltd, Gloucester, UK.

[12] California Fine Wire Company, Grover City, Ca. USA.

[13] M. Coupland, Nucl.Inst.Meth. **A252** 211 (1983).

[14] Yeovil Circuits, Yeovil, Somerset, UK.

[15] G. Beck, University of Liverpool, Private Communication.

[16] SY227 Current Monitor, CAEN, Viareggio, Italy.

[17] SY127 High Voltage Supply, CAEN, Viareggio, Italy.

[18] M. Hohlmann, *Test der Vorwärts-Spurkammern des H1-Detektors mit kosmischen Teilchen* Diploma Thesis, III Phys. Inst., RWTH Aachen **PITHA 92/27** (July 1992).

[19] W. Zimmermann, DESY, Private Communication.

[20] F1000 FADC System, DESY / Struck.

[21] S. Kolya. University of Manchester, Private Communication.

[22] DL300 FADC System, Struck.

[23] H. Grässler et al, Nucl.Inst.Meth. **A283** 622 (1989).

[24] L. Gatignon, CERN. Private communication.

[25] D.P.C. Sankey. PhD Thesis, University of Liverpool 1990, **RALT-115**.

[26] H. Klar, DESY, Private Communication.

[27] A. Manarin, G. Vismara. **LEP/BI-TA/Note 85-3**. CERN (1985).

[28] LeCroy LRS 620L.

[29] D. Johannes Heidenhain, D-8225 Traunreut, Germany.

[30] H. Breuker *et al.* Nucl.Inst.Meth **A260** 329 (1987).

[31] S. J. Maxfield and D.P.C. Sankey. H1-Tracking Note **24** (1990).

[32] T. Pomentale. Subroutine LINSQ, CERN Program Library, (1989).

[33] B. Jean Marie *et. al.* Nucl.Inst.Meth **159** 213 (1979)

[34] Plot courtesy of R. Martin. University of Liverpool.

[35] F. Sauli, *Principles of Operation of Multiwire Proportional and Drift Chambers.* **CERN 77-09** (1977).

[36] G. L. Salmon, *Centaur Gas Gain*, ZEUS-Oxford-89-7 (1989).

[37] P.A. Lyn, *An Introduction to the Analysis and Processing of Signals*, second edition, Macmillan, London (1982).

[38] V. Radeka and P. Rehak, IEEE Trans. Nuc.Sci.NS-26, No. 1, 225 (1979).

[39] V.L. Ginzberg and I.M. Frank. Zh.Eksp.Teor.Fiz. (Sov.Phys-JETP) 16 (1946). 15.

[40] Plot courtesy of S. J. Maxfield, University of Liverpool.

[41] See for example W. J. Duffin. *Electricity and magnetism*, 3rd edition. McGraw-Hill. (1980).

[42] P. Horowitz and W. Hill, *The Art of Electronics*, Cambridge University Press. (1980).

[43] H. Umstaetter. Subroutine MULLER, CERN Program Library, (1989).

[44] J.M. Bailey *et. al.* Nucl.Inst.Meth. **A323** (1992) 184-190

Associated Publications

- H. Gräßler *et. al.*

  Precision Reconstruction of Charged Tracks with Simultaneous Electron Identification in a Gaseous Detector using Transition Radiation.

  Nucl. inst. Meth. A310 (1991) 535

- J.M. Bailey *et. al.*

  Spatial Precision of an H1 Radial Wire Drift Chamber using Gas Mixtures Suitable for Transition Radiation Detection.

  Nucl. Inst. Meth. A323 (1992) 184-190

- H. Gräßler *et. al.*

  Electron Identification in the H1 Radial Drift Chambers.

  Nucl. Inst. Meth. A323 (1992) 401-406

- The H1 Collaboration (T. Ahmed, *et al.*),

  Hard scattering in γp interactions.

  Phys.Lett.B 297 (1992) pp 205-213

- The H1 Collaboration (T. Ahmed, *et al.*),

  Total photoproduction cross-section measurement at HERA energies.

  Submitted to Phys.Lett.B

- The H1 Collaboration (T. Ahmed, *et al.*),

  Measurement of the hadronic final state in deep inelastic scattering at HERA.

  Phys.Lett.B 298 (1993) pp 469-478

- The H1 Collaboration (T. Ahmed, *et al.*),

  Observation of deep inelastic scattering at low x.

  Submitted to Phys.Lett.B